Joining Carbon Fiber and Aluminum with Ultrasonic Additive Manufacturing

A Thesis

Presented in Partial Fulfillment of the Requirements for the Degree
Master of Science in the Graduate School of The Ohio State
University

By

M. Bryant Gingerich,

Graduate Program in Mechanical Engineering

The Ohio State University

2016

Master's Examination Committee:

Dr. Marcelo J. Dapino, Advisor

Dr. Anthony Luscher

© Copyright by

M. Bryant Gingerich

2016

Abstract

Due to increasing emphasis on lightweighting to increase fuel efficiency, integration of carbon fiber reinforced polymers (CFRP) with metal structures is necessary. Current adhesive and mechanical fastening methods used for joining CFRP to metals are not ideal due to poor mechanical properties and incompatibility with current manufacturing infrastructure. Consequently, new joining techniques are needed for increasing the use of CFRP. In this research project, a method of creating joints between CFRP and 6061-H18 aluminum was developed by using ultrasonic additive manufacturing (UAM). The UAM process was used to embed dry carbon fiber tows within an aluminum matrix, creating a mechanical joint between the two materials. The joints were then integrated with additional CF fabrics and epoxy, forming a fully integrated CF-Al structure. This technique was used to create CF-Al joints for tensile, cross tensile, and three-point-bend testing. Mechanical test results showed that the UAM constructed joints had superior strength when compared to adhesive single lap joints. Throughout the UAM joint manufacturing process, experimental observations paired with FEA were used to help solve issues with foil tearing, which is a common problem experienced when materials are embedded with UAM.

Acknowledgments

I would like to thank a number of individuals who have helped me immensely with this research project. First of all, I would like to thank my adviser, Professor Dapino for allowing me to be a part of his exciting and groundbreaking research. I am grateful for his insightful guidance throughout the project as well as his financial support. Thanks to Xiang Chen, Leon Headings, Paul Wolcott, and Adam Hehr for their continued support and advice. Also thanks to Matt Scheidt who has spent countless hours improving SMSL testing equipment and has been a great friend though my time in the laboratory. Thanks to Ryan Hahnlen for his advice and for helping with supplies and testing equipment. Special thanks to Prof. Luscher for his willingness to serve on my examination committee. This acknowledgment would not be complete without recognizing Mark Norfolk and his team from Fabrisonic who have faithfully kept the UAM machine running - often coming to the rescue on very short notice.

Outside of lab, I have an amazing network of family and friends who have supported me in the decision pursue a master's degree. To my friends, thanks for providing an outlet for activities outside of lab. To my mentors: Noah and Willard, thank you for your prayers and words of wisdom. To my grandparents: Marvin and Betty, Lloyd, thank you for your love, prayers, and financial support. Your impact on my life is more than you can know. To my family, thanks for love, laughter, and encouragement. Mom and dad, thanks for your constant guidance through this season of

my life. Finally I'd like to thank my fiance, Amy, for the joy that she has brought into my life through this period of transition. I thank God for you daily.

- Soli Dei Gloria -

Vita

December 2014	B.S. Mechanical Engineering, Magna Cum Laude, The Ohio State University
January 2014 - May 2016	Graduate Research Assistant: The Ohio State University

Fields of Study

Major Field: Mechanical Engineering

Studies in:

Ultrasonic Additive Manufacturing	Dr. Marcelo Dapino
Metal/FRP Joining	Dr. Marcelo Dapino

Table of Contents

Page

Abstract ii

Acknowledgments iii

Vita v

List of Tables ix

List of Figures xi

1. Introduction 1

    1.1 Literature Survey 1
        1.1.1 Background 1
        1.1.2 Current Joining Methods 3
        1.1.3 Joining of Aluminum to CFRP by Ultrasonic Welding . . . 5
        1.1.4 Carbon Fiber to Metal Galvanic Corrosion 8
        1.1.5 Ultrasonic Additive Manufacturing 15
    1.2 Objectives 22

2. Embedding Carbon Fiber within Metals Using UAM 24

    2.1 Embedding CF into 6061-H18 Aluminum 24
        2.1.1 Consolidation Preparation and Process 24
        2.1.2 Cross Section Micro-imaging Results 26
        2.1.3 Mechanical Pullout Testing on Embedded CF Tows 27
    2.2 Embedding Nickel Coated CF into 6061-H18 Aluminum 32
        2.2.1 Consolidation Preparation and Process 32
        2.2.2 Cross Section Micro-imaging Results 33
        2.2.3 Mechanical Pullout Testing on Embedded Nickel Coated CF Tows 34

2.3 Embedding CF into 4130 Steel using 201 Nickel as Interlayers . . . 36
    2.3.1 Welding 4130 Steel using 201 Nickel Interlayers 36
    2.3.2 CF Consolidation Preparation and Process 38
    2.3.3 Results and Discussion 40
2.4 Embedding Glass Fibers into 6061-H18 Aluminum 40
    2.4.1 Consolidation Preparation and Process 41
    2.4.2 Mechanical Pullout Testing on Embedded Glass Fiber Tows 41
2.5 Summary and Discussion 42

3. Design, Construction, and Testing of CF-Al UAM Joints 44

3.1 Three Layer, Straight Channel Joints 45
    3.1.1 Joint Design and Manufacturing 45
    3.1.2 Corrosion Testing 49
    3.1.3 Tensile Testing 54
    3.1.4 Three-Point-Bend Testing with Adhesive Joint Comparison 59
    3.1.5 Discussion 65
3.2 Five Layer, Straight Channel Joints 66
    3.2.1 Joint Design and Manufacturing 66
    3.2.2 Tensile Testing Results 68
    3.2.3 Three-Point-Bend Testing and Results 71
    3.2.4 Discussion 75
3.3 Curved Channel CF-Al Joints 75
    3.3.1 Joint Design and Manufacturing 76
    3.3.2 Tensile Testing 78
    3.3.3 Discussion 82
3.4 Curved Channel Joints with Increased Adhesive Joining Area . . . 83
    3.4.1 Joint Design and Manufacturing 83
    3.4.2 Tensile Testing 86
    3.4.3 Discussion 93
3.5 Cross Tensile Joints 93
    3.5.1 Joint Design and Manufacturing 94
    3.5.2 Cross Tensile Testing 98
    3.5.3 Discussion 104
3.6 CF-Al UAM Joint Summary and Discussion 105

4. Adhesive Lap Joint Benchmarking 107

4.1 Adhesive Joint Construction 107
4.2 Adhesive Joint Testing 109
    4.2.1 Tensile Specimens 109
    4.2.2 Cross Tensile Specimens 111

4.3 Comparison: Adhesive Joints vs. UAM Joints 112

5. UAM Foil Tearing 115

5.1 Introduction 115
5.2 Experimental Observations 116
5.2.1 Factors Not Substantially Affecting Foil Tearing 116
5.2.2 Factors Affecting Foil Tearing 122
5.2.3 Predicted Root Cause 124
5.3 Finite Element Analysis Model 125
5.3.1 Assumptions 126
5.3.2 Inputs 128
5.4 FEA Model Results 132
5.4.1 Results at the Center and End of Channel Locations using Standard Assumptions 134
5.4.2 FEA Results for Three Special Cases 139
5.5 Discussion and Future Work 144
5.5.1 Summary and Conclusions 144
5.5.2 Future Work Items 145

6. Concluding Remarks 147

6.1 Summary 147
6.2 Future Work 149

Bibliography 152

List of Tables

Table **Page**

2.1 UAM parameters used for single CF tow consolidation. 26

2.2 UAM parameters used for single nickel electroplated CF tow consolidation. 32

2.3 Properties of the steel and nickel foils. 37

2.4 UAM parameters used when welding 4130 steel using 201 nickel interlayers. 37

2.5 UAM parameters used while consolidating CF within a steel/nickel structure. 39

3.1 UAM parameters used during three layer, straight channel joint construction. 47

3.2 Three layer, straight channel HTS stacking sequence. 48

3.3 UAM parameters used for five layer CF-Al joints. 68

3.4 Five layer CF-Al joint stacking sequence. 68

3.5 UAM parameters used for curved channel CF-Al joints. 78

3.6 Tensile testing summary for CF-Al joints with CF sandwich features. 90

3.7 UAM parameters used for cross tensile CF-Al joints. 97

3.8 Cross tensile testing summary for CF-Al joints with CF sandwich features. 103

5.1 Material properties used in the FEA model. 129

5.2 Summary of FEA results for cases with standard assumptions. 138

5.3 Summary of FEA results for special cases. 143

List of Figures

Figure **Page**

1.1 Lap shear response comparison between adhesive joint and adhesive/welded joint [15]. 5

1.2 Orientation of ultrasonic metal and plastic welding [10]. 7

1.3 Contrasting the single lap strength of UPW with that of UMW [8]. . . 8

1.4 The basic concept of galvanic corrosion [14]. 9

1.5 Simplified galvanic series 10

1.6 CFRP/aluminum joint with fiberglass corrosion barrier [30]. 13

1.7 Effect of epoxy coating over carbon fiber/steel couples. [32] 14

1.8 UAM system tools for ultrasonic welding and milling operations. (Courtesy of Fabrisonic) 16

1.9 Basic principles of UAM (courtesy of Fabrisonic). 18

1.10 VHP UAM system used by the Smart Materials and Structures Laboratory at The Ohio State University. 20

1.11 Push pin test for testing UAM welded layer bonding [34]. 21

1.12 Shear and tensile mechanical testing of UAM welded builds [20]. . . . 22

2.1 CF consolidation sequence. (a) Channels are cut into base 6061-H18 Al layers, (b) CF tows are placed into the channels, (c) layers of 6061-H18 Al foil are welded over the CF tows. 25

2.2 Images of an early attempt at consolidating CF tows without the use of channels to house the fibers. 26

2.3 SEM micro-images of a CF tow which was housed in a channel during consolidation. 27

2.4 Schematic showing pullout test specimen construction. 28

2.5 In house load frame with pullout fixture for embedded fiber pullout strength test. 29

2.6 Pullout strength of epoxy impregnated joints compared with the strength of dry joints. 30

2.7 Three different failure modes seen in CF - Al pullout specimens wetted with epoxy. (a) Specimen E3, complete pullout from joint; (b) Specimen E4, failure in the fiber gauge length - no joint failure; (c) Specimen E5, brittle failure near the front edge of joint. 31

2.8 Consoliation nickel coated CF tows. (a) CF placed in the channels, (b) CF embedded and pullout specimens cut out. 33

2.9 SEM micro-images of consolidated nickel coated CF. 34

2.10 Pullout test results for nickel coated CF tows with different wetting conditions. 35

2.11 Optical micro-images of 4130 steel welded with 201 nickel interlayers. 37

2.12 Consolidation CF into a 4130 steel/201 nickel structure. (a) Channels are cut, (b) CF placed into channels, (c) nickel interlayer placed over CF, (d) steel foil welded over nickel and CF. 39

2.13 Load vs. displacement during the glass tow pullout testing. 42

3.1 Schematic of the three embedded CF layer hybrid transition structure design with straight channels. 45

3.2 Carbon fiber embedding sequence in the three layer, straight channel CF-Al joint design. 46

3.3 (a) Three layer, straight channel CF-Al joint after baseplate removal, (b) Tensile specimen formed after layup with additional CF bidirectional fabric layers and epoxy. 49

3.4 Glass fabric being consolidated into 6061-H18 aluminum. 50

3.5 Schematic portraying CF-GF-Al hybrid joint design. 51

3.6 Specimen visual appearance before and after the corrosion cycling for CF-Al and CF-GF-Al joints. 53

3.7 Epoxy cracking observed in corroded CF-Al joint. 54

3.8 Tensile testing equipment: (a) Interlocken frame, MTS grips, and DIC camera setup. (b) Control and data aquisition center. 55

3.9 DIC strain maps of failure initiation overlaid onto tensile specimens. (a) Corroded CF-Al tensile specimen. (b) Non-corroded CF-Al tensile specimen. (c) Corroded CF-GF-Al tensile specimen. (d) Non-corroded CF-GF-Al tensile specimen. 56

3.10 Load vs. displacement for each of the four three embedded layer tensile specimens. 57

3.11 Failed specimens from tensile testing: (a) Adhesive failure in the non-corroded CF-GF-Al specimen (surface is covered with DIC speckling). (b) Adhesive failure in the corroded CF-GF-Al specimen. (c) Aluminum failure in the non-corroded CF-Al specimen. 58

3.12 Schematic showing the three-point-bend specimen design featuring three-layer CF-Al UAM joints. 60

3.13 (a) CF-Al joint before layup into the three-point-bend structure. (b) Completed UAM CF-Al three-point-bend specimen. 61

3.14 (a) Adhesive three-point-bend components, complete with treated joining surfaces. (b) Clamping the three-point-bend adhesive components together. 62

3.15 (a) Interlocken load frame set up with the three-point-bend fixture. (b) Three-point-bend fixture detail. 63

3.16 Load vs. displacement for UAM CF-Al and Adhesive CF-Al joints. . 64

3.17 Components of the failed adhesive single lap three-point-bend speicmen. 64

3.18 (a) Damaged UAM CF-Al joint. (b) Detail of UAM CF-Al joint damage. 65

3.19 Embedding sequence for the five layer CF-Al joint manufacturing process. 67

3.20 Tensile results from the five layer CF-Al tensile test compared with three embedded layer CF-Al joint performance. 69

3.21 Strain mapping overlaid on the five embedded CF-Al specimen. (a) Immediately before initial cracking at the base of the aluminum tab. (b) Immediately after initial cracking at the base of the aluminum tab. 70

3.22 (a) The five embedded layer CF-Al joint after tensile testing. (b) Failed joint detail. 71

3.23 Schematic of the five embedded layer three-point-bend specimen. . . . 72

3.24 Three-point-bend DIC setup. (a) Camera positioning. (b) DIC strain mapping results. 73

3.25 The five layer three-point-bend load vs. displacement curve compared with the three layer and adhesive joints. 74

3.26 (a) Failed five layer three-point-bend specimen. (b) Detail of aluminum tab failure. 74

3.27 Curved channel CF-Al joint manufacturing progression. (a) CF is prepared for embedding by cutting and removing unwanted tows. (b) Channels are cut into base foil layers. (c) CF tows are placed into channels. (d) Aluminum foil is welded to consolidate the CF. (e) The joint is removed from the aluminum baseplate when the welding process is completed. 77

3.28 Load vs. displacement for two thicknesses of curved channel CF-Al joints compared with the straight channel design. 79

3.29 Thin curved channel CF-Al joint failure sequence: (a) Cracking initiates in the left inside corner between the aluminum tab and CFRP plate. (b) Cracking propagates. (c) Cracking continues to propagate. (d) Entire aluminum tab interface has separated from the bulk CFRP. (e) Crack initiates in aluminum tab at upper left channel. (f) Aluminum tab failure. 81

3.30 (a) Failed thin curved CF-Al tensile specimen. (b) Failed thicker CF-Al tensile specimen. (c) Detail of failed thicker CF-Al tensile specimen. . 82

3.31 CF-Al joint construction featuring the flange concept. (a) CF is placed into channels, (b) Flange material is manually laid over channels, (c) Flange material is welded over the CF, (d) Completed structure with two integrated flanges. 84

3.32 CF-Al curved channel tensile specimen with the flange feature. (a) Front, (b) Back. 85

3.33 CF-Al curved channel tensile specimen with the CF sandwich feature. (a) Front, (b) Back. 86

3.34 DIC strain mapping of the CF-Al joint with curved channels and the aluminum flange feature. (a) Crack initiation, (b) Crack propagation. 87

3.35 Load vs. displacement curves for CF-Al joints with increased adhesive bonding area features compared with the original CF-Al curved channel design. 88

3.36 (a-e) CF-Al joints with curved channels and CF sandwich features. (f) CF-Al sandwich feature joint without embedded CF. 89

3.37 Tensile testing load vs. displacement curves CF-Al joints with CF sandwich features. 90

3.38 Strain maps overlaid on specimens during failure. (a) DIC strain map of a CF-Al joint with the sandwich feature and no embedded CF. (b) DIC strain map of a CF-Al joint with curved channels and the sandwich feature. 92

3.39 (a-e) Failed CF-Al joints with CF embedded in curved channels and sandwich features. (f) Failed CF-Al adhesive sandwich joint. 92

3.40 Cross tensile CF-Al joint schematics: (a) Without sandwich feature. (b) With sandwich feature. 95

3.41 (a) Cross tensile specimens being manufacturing in UAM center. (b) One of the cross tensile joints after baseplate removal. 96

3.42 Finished cross tensile joints. (a) CT joint with embedded CF only. (b) CT joint with embedded CF and CF sandwich feature. 98

3.43 (a) Mounting a cross tensile specimen into the cross tensile loading fixture. (b) Cross tensile testing setup, with Interlocken load frame, MTS grips, and in-house built loading fixture. 99

3.44 Cross tensile CF-Al joint load vs. displacement curves. 100

3.45 Failed cross tension joints. (a) Cross tensile joint with embedded CF only. (b) Cross tensile joint with embedded CF and CF sandwich feature. 100

3.46 (a-d) CF-Al cross tensile joints with embedded CF and CF sandwich features. (e) CF-Al joint with sandwich feature, but no embedded CF. 101

3.47 Load vs. displacement of CF-Al cross tensile testing. 102

3.48 Failed CF-Al cross tensile joints. (a-e) Joints with embedded CF and sandwich features. (e) Joint with no embedded CF, adhesive only. (f) Detail of CF sandwich delamination and shearing from specimen 5. . 103

4.1 Adhesive joint assembly process. (a) Prepared aluminum tensile specimen parts, (b) prepared aluminum cross tensile specimen parts, (c) Glueing a tensile specimen, (d) Glueing a cross tensile specimen, (e) two part adhesive applicator gun with mixing tips, (f) Clamping with weights. 108

4.2 Completed adhesive joints. (a) Adhesive cross tensile joint. (b) Adhesive tensile joint. (c) Side profile of adhesive tensile joint. The specimen thickness is exaggerated for clarity. 109

4.3 Load vs. displacement curves taken during the adhesive tensile testing. 110

4.4 Adhesive tensile joint failure classification. (a) Specimen 1: mix of adhesive and cohesive failure. (b) Specimen 2: Adhesive failure with a small amount of cohesive failure. (c) Specimen 3: adhesive failure. (d) Specimen 4: adhesive failure. 111

4.5 Load vs. displacement curves of the adhesive cross tensile joint testing. 112

4.6 UAM and adhesive CF-Al joints compared for tensile and cross tensile testing cases. 113

5.1 Foil tearing examples. (a) Multiple tear locations while welding over cross-hatch channels filled with CF tows. (b) Case of foil tearing where the channels run parallel to the welding direction. (c) Foil tearing over the first channel with a "bent" channel design. (d) Foil tearing over the first channel with a angled design. 117

5.2 Normal force profile when welding a foil layer directly over cross-hatch channels before and after the controller gain adjustments. 118

5.3 Stress vs. strain curves for 6061-H18 aluminum tape, before and after 18 hour aging at 160 $C°$. 120

5.4 Examples of foil tearing on builds with channel arrangements specifically designed for even substrate compliance over the embedded fiber region. (a) Foil tearing persists with angled channels. (b) Foil tearing at the front channel of a build utilizing the "bent" channel design to minimize substrate compliance over the channel region. 121

5.5 The effect of having CF tows in the channels. (a) Channels are cut at 1.8 mm x 0.28 mm in width and depth respectively. (b) Layer of aluminum foil is welded over the unfilled channels. This resulted in no foil tearing. (c) Layer of foil is welded over channels filled with CF tows. Several foil tears are produced. 123

5.6 Schematic showing the predicted root cause of foil tearing. 125

5.7 Solid model of the part assembly used in the FEA model 128

5.8 Stress vs. strain approximation used in the FEA model overlaid onto experimental stress vs. strain curves. The experimental testing was completed on 6061-H18 aluminum samples post UAM welding. 129

5.9 Boundary conditions applied to the FEA model. 131

5.10 S_{13} stress state which is an indicator of foil tearing failure. 133

5.11 FEA S_{13} stress results at the middle and end of channel positions. Cases for sonotrode to foil friction coefficients of 0.5 and 0.2 are shown. The dark red color indicates yielding. (a) End of channel position with friction coefficient of 0.5. Yielding predicted. (b) End of channel position with a friction coefficient of 0.2. No yielding is predicted. (c) Middle of channel position with a friction coefficient of 0.5. Yielding is predicted. (d) Middle of channel position with a friction coefficient of 0.2. Yielding is predicted. 135

5.12 Schematic showing FEA validation technique. 137

5.13 FEA S_{13} shear stress results at the center of channel position with reduced normal force (a) compared with the original simulation force case (b). Dark red indicates yielding. 138

5.14 Special Case 1 FEA results and comparison. Dark red indicates yielding. (a) FEA results from securing the foil after the channel with a tie constraint. (b) The original FEA result with the foil/base layer interface given frictionless tangential properties. 140

5.15 Special Case 2 FEA results and comparison. Dark red indicates yielding. (a) FEA S_{13} shear stress results for the special case where the CF/foil interface is given a friction coefficient of 0.5. (b) FEA S_{13} shear stress results for the original center of channel position case . . 141

5.16 Special Case 3 FEA results with the foil and base layer edges constrained from 3-direction motion. Dark red indicates yielding. (a) 3-direction constraints on the base layer and foil edges. (b) FEA S_{13} shear stress results from using the 3-direction constraints. (c) FEA S_{13} shear stress results from original center of channel position case. . . . 143

Chapter 1: INTRODUCTION

1.1 Literature Survey

1.1.1 Background

With fuel efficiency becoming an increasing concern, the design and manufacture of lightweight vehicles has been on the rise. This is the case in the automotive industry as well as the aerospace industry. To achieve effective weight reduction, composite materials are starting to be used in many structural applications. In high performance situations the use of carbon fiber reinforced polymers (CFRP) is becoming increasing common. In October of 2011, the Boeing 787 Dreamliner commercial aircraft made its debut. Half of the Dreamliners weight is made from carbon fiber composites reducing the weight of the aircraft by 20% when compared to more conventional aluminum designs [18]. Such weight reduction is beneficial to fuel economy, reducing operating costs as well as leaving a smaller carbon footprint. According to the aerospace consultancy firm, AeroStrategy LLC, in 2008 the aerospace industry accounted for nearly 60% of the carbon fiber produced. This is mainly due to the large quantities of carbon fiber used by aircraft giants Boeing and Airbus [31].

While there is certainly motivation for the automotive industry to adopt the use of carbon fiber, it has been slower to embrace this lightweighting technology. For automotive applications, reducing vehicle weight by 100 kg on the average vehicle corresponds to a 0.3-0.4 liter per 100 km reduction in fuel consumption [21]. Currently carbon fiber use in automobiles is mostly limited to high end sports cars and race cars. One of the main reasons for the slow adoption process of carbon fiber by the automotive industry is cost. Carbon fiber costs approximately 20 USD/kg, this should be compared to the price of steel which is only 1 USD/kg. Despite the cost, automotive manufacturer BMW has already adopted CFRP into their mass produced i3 series [26]. BMW expects to reduce the cost of a carbon fiber frame down to the level of aluminum by year 2020 [26]. They have made a huge step toward vehicle lightweighting and other auto manufacturers will follow. The use of carbon fiber in the automotive industry is increasing due to carbon fiber cost reduction and recent advances in carbon fiber manufacturing techniques.

One of main advances in carbon fiber technology is in resin transfer molding (RTM) techniques. Resin transfer molding involves a reinforcement mat and low viscosity resin which is injected under pressure. First a dry unimpregnated carbon fiber pre-shaped reinforcement is prepared into the preform which is the skeleton of the actual part to be created. The preform is paired with a matching die mold. After the mold is closed the resin is injected under pressure. Heat is then applied to activate the curing process. The part can be removed from the mold as soon as it develops sufficient strength for handling. [21] Japanese textile manufacturer and carbon fiber products supplier, Toray Industries, has developed a carbon fiber processing method that will make mass production of lightweight, carbon fiber vehicles possible. This process marries proprietary resin transfer molding techniques with enhanced resin infiltration and hardening technologies. This improved process has been used to shorten the molding cycle from 160 minutes to 10 minutes. Studies have shown that these CFRP parts are 1.5 times safer in a collision than steel parts. This program to develop CFRP parts for automotive use is backed by the Japanese Government. [31]

Recent innovations in resin transfer molding has made producing large and complex shapes with good laminate surface quality possible. The process also enables integration of ribs, cores and inserts. While the RTM process allows integration with some load attachments and secondary structures, the requirement to join to other load attachment points and secondary structures is unavoidable [21]. These structural components could include metallic space frames or secondary structures including seat mountings and suspension systems. Composite materials are much more complex than metallic ones in the way they support loadings. Metallic materials are nearly homogenous and can dissipate local stress concentrations due to plasticity. Composites on the other hand exhibit material anisotropy, poor interlaminar strength and lack local stress relief [21]. Developing joining techniques for composites is challenging, but is necessary to tackle for enabling robust integration of CFRP structures into automotive and aerospace products.

1.1.2 Current Joining Methods

A common industrial joining technique for metals is resistive spot welding. For metal to metal joints, this method has been used to create high strength joining and can be integrated into efficient, highly automated processes. However, resistive spot welding cannot be used with CFRP to metal joining [17]. As a result, joining techniques including adhesives, mechanical fasteners, or a combination of the two have been used

[21]. The primary method of joining composites to metals is by high-strength adhesive joining. Adhesive joining is typically favored over mechanical fasteners such as bolts and rivets because these methods produce point-source loadings which requires thicker, heavier material [37]. Adhesive joining also offers intrinsic galvanic corrosion protection when joining materials such as carbon fiber to metals [37]. While adhesive joining has a number of important positive points, it is not without flaws.

The primary shortcoming of adhesive joining is inherently weak peal strength [11]. In practice, bonded structures are exposed to a combination of different loadings. These include tensile, compressive, shear, cleavage, and peel stresses. Engineers usually design some form of lap shear joint for use with adhesives. These joints are not ideal structurally because under load both shear and peel stresses are activated [5]. There is little that can be done to reduce the amount of induced peel stress in single lap joints. Additionally, surface finish does not have as great of an effect on peel strength as it does in tensile strength [36]. As a result, optimizing the surface finish is not a viable solution to reducing peel failure.

Hybrid joints have been developed which feature adhesive joining aided by welded steel clamping [15]. The strength and toughness of this hybrid joint is compared with plain adhesive joining in Figure 1.1. Hybrid joints are an improvement over purely adhesive joints because they reduce delamination and peel failure. Consequently, the strength of welded/adhesive joints is slightly greater than adhesive joints and the toughness is greatly improved. Another positive point of hybrid joints is that the joint can be clamped together via the welding while the adhesive is curing [37]. This allows for a more streamlined manufacturing process.

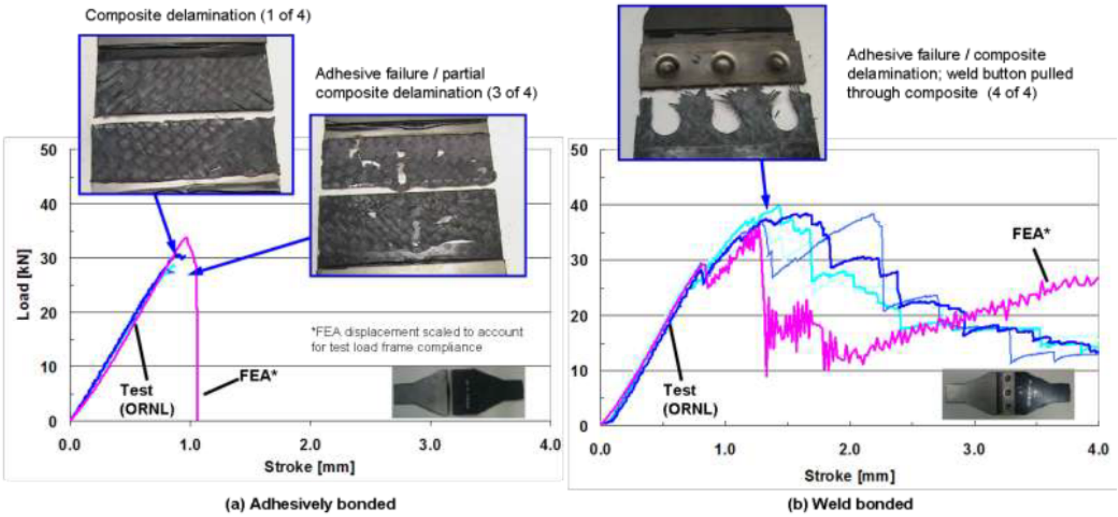

Figure 1.1: Lap shear response comparison between adhesive joint and adhesive/welded joint [15].

Other recently developed joining methods for CFRP to metals include friction spot joining [6], metal to metal foam to composite joining [38], cold metal transfer pin techniques [35], and ultrasonic welding [7]. These joining techniques will not be discussed in detail with the exception of ultrasonic welding, since the process is similar to the ultrasonic additive manufacturing process used in this research project.

1.1.3 Joining of Aluminum to CFRP by Ultrasonic Welding

Ultrasonic welding is a solid state welding technique where the joining occurs as the result of static pressure coupled with ultrasonic oscillations directed from a weld head (often called the sonotrode) into the two joining structures. When compared to fusion welding or brazing, ultrasonic welding is marked by low energy input. This results in a joining process that is characterized by low maximum temperatures. Ultrasonic welding is particularly well suited to welding of thin foils of metal or thin sheets to thicker sheets. Dissimilar metals can also be welded with high power ultrasonic welders. [8]

The primary welding parameters used in ultrasonic welding include oscillation amplitude, welding force exerted on the joint, welding energy, and workpiece temperature. It is possible to create robust welded joints between unique materials combinations by tailoring the welding parameters for the application. In addition to welding parameters, the joining material properties, surface conditions, and part geometry can also play large factors in the quality of ultrasonically welded joints.

There are two primary types of ultrasonic welders. These are defined by their sonotrode oscillation orientations. Ultrasonic metal welders have transducers which induce oscillations in the sonotrode parallel to the joining surfaces. Ultrasonic metal welding (UMW) is well suited for joining of metals. Conversely, ultrasonic plastic welding (UPW) features sonotrode oscillations perpendicular to the joining surfaces. Ultrasonic plastic welding has traditionally been used for the welding of polymers. [8]

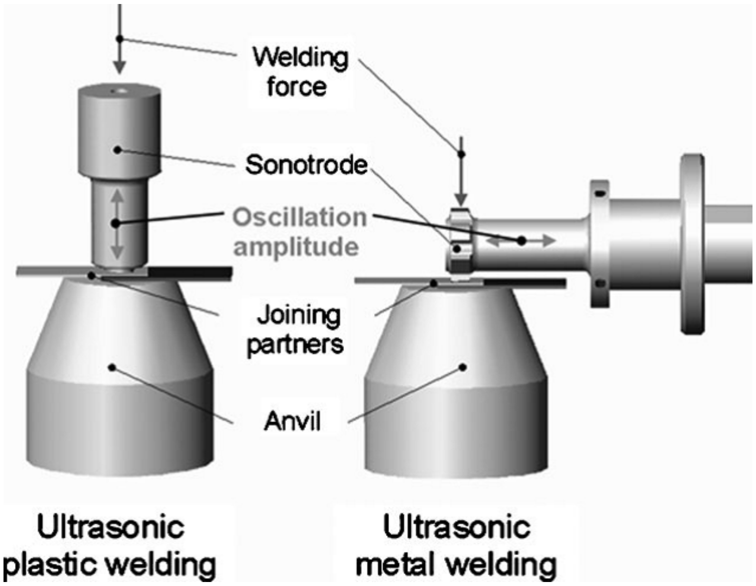
Welding force
Sonotrode
Oscillation amplitude
Joining partners
Anvil
Ultrasonic plastic welding
Ultrasonic metal welding

Figure 1.2: Orientation of ultrasonic metal and plastic welding [10].

Balle et al. [8] showed that ultrasonic metal welding is more effective in joining carbon fiber reinforced polymers to metals than ultrasonic plastic welding. The CFRP chosen for welding in this study had a thermoplastic matrix (PA66). This was used to allow energy from the ultrasonic welder to push the matrix between the carbon fibers and the metal interface aside. This matrix choice is important, because carbon fiber composites with epoxy as the matrix cannot be welded [37]. Using UMW with the PA66 matrix resulted in direct mechanical joining between the metal and carbon fibers. When ultrasonic plastic welding was used, it was much less effective in pushing the matrix aside, resulting in a intermediate layer of thermoplastic matrix between the fibers and metal [8].

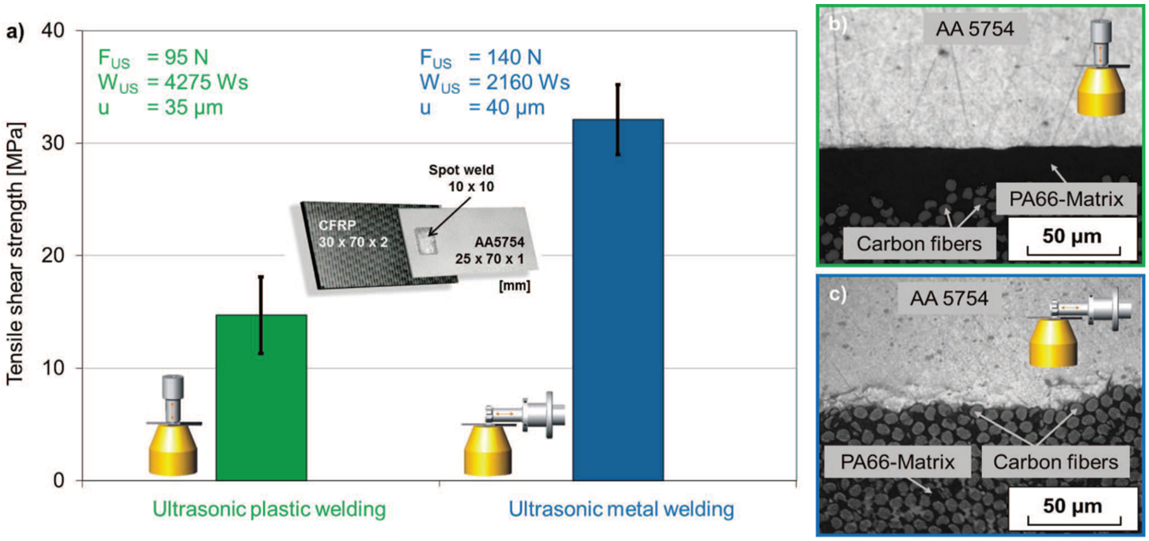

Figure 1.3: Contrasting the single lap strength of UPW with that of UMW [8].

Balle et al. had excellent results with joining aluminum to CFRP with a PA66 matrix. Further improvements of this joining method were achieved by making surface finish modifications including acid etching and corundum-blasting of the aluminum joining member. Using this pre-welding surface treatment, the joint strength was increased from 30MPa to nearly 50MPa [9]. The main shortcoming of ultrasonic welding of CFRP to aluminum is that it requires a thermoplastic matrix which is generally not used in the RTM process. However, a great deal of research is being done to develop a thermoplastic chemistry that is compatible with RTM and can meet the stringent cycle time necessary for mass production [27].

1.1.4 Carbon Fiber to Metal Galvanic Corrosion

The very idea of CFRP to metal joining is controversial because of the phenomenon of galvanic corrosion. Typical cases of galvanic corrosion include two joined metals such as aluminum and steel which are in the presence of an electrolyte fluid. While carbon fiber is not a metal, it is conductive and highly cathodic, making CF/metal joining a recipe for corrosive disaster if careful design steps are not taken. Because of it's relevance CF/metal joining, a literature survey of CF/metal galvanic corrosion principles, modeling, and prevention measures was conducted. Though intensive corrosion testing has not yet been completed with UAM CF/metal joints, the information from this literature survey will be useful in future design phases of this work.

Galvanic corrosion occurs when two metals (or graphite) of different electric potentials are in electrical contact with each other and both are immersed in an electrolyte fluid. This concept is illustrated in Figure 1.4. While it is common to find the ingredients for galvanic corrosion in mechanical design, whether galvanic corrosion will be problematic depends on the corrosion rate and desired part lifetime.

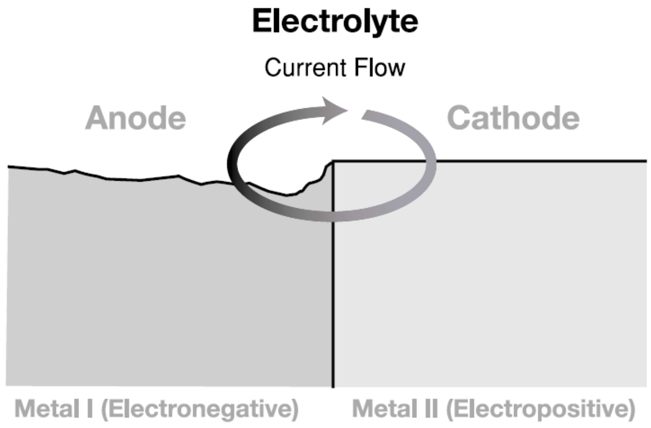

Figure 1.4: The basic concept of galvanic corrosion [14].

There are a number of factors which influence galvanic corrosion rate, shown in Equation 1.1 [29]. The driving force for galvanic corrosion is the electric potential difference between the two electrically connected conductors ($E_c - E_a$). The greater the difference in electric potential, the greater the corrosion rate. In terms of carbon fiber to metal joining, graphite is noble (cathodic) and metals like aluminum and steel are fairly active (anodic). This produces a combination that traditionally would be avoided. Figure 1.5 shows a simplified version of the galvanic series which essentially ranks different materials based on their electric potentials.

$$I_{galv} = \frac{E_c - E_a}{R_a + R_c + R_s + R_m} \tag{1.1}$$

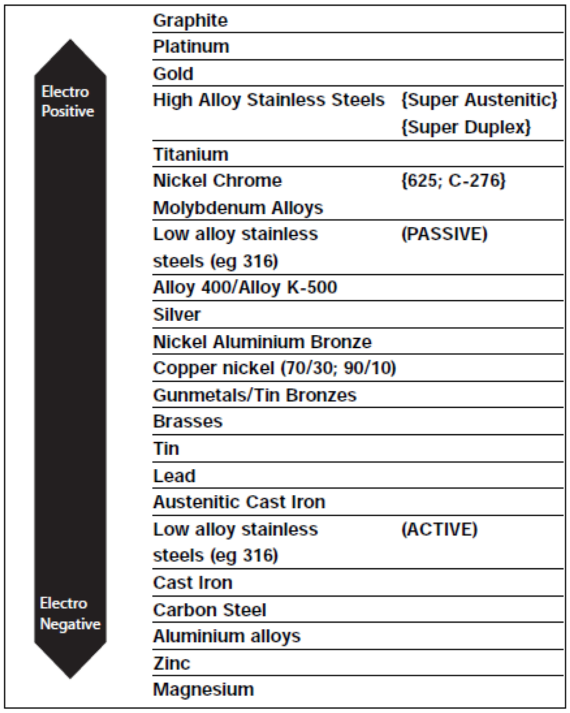
Electro Positive
Electro Negative

Graphite	
Platinum	
Gold	
High Alloy Stainless Steels	{Super Austenitic} {Super Duplex}
Titanium	
Nickel Chrome Molybdenum Alloys	{625; C-276}
Low alloy stainless steels (eg 316)	(PASSIVE)
Alloy 400/Alloy K-500	
Silver	
Nickel Aluminium Bronze	
Copper nickel (70/30; 90/10)	
Gunmetals/Tin Bronzes	
Brasses	
Tin	
Lead	
Austenitic Cast Iron	
Low alloy stainless steels (eg 316)	(ACTIVE)
Cast Iron	
Carbon Steel	
Aluminium alloys	
Zinc	
Magnesium	

Figure 1.5: Simplified galvanic series

Though carbon fiber to metal joining is a scenario that would traditionally be avoided, it is a joining situation that is important for the automotive and aerospace industries because of lightweighting. There are also other factors playing into the galvanic corrosion rate which can be used to minimize corrosion. These factors are represented by the resistive elements in Equation 1.1. R_a and R_c are the anode resistance and cathode resistance respectively. These resistance factors can increase dramatically by coating the respective metal surface with a non-conductive coating. The resistance factor, R_s, is the resistance of the electrolyte solution between the anode and cathode. The final factor, R_m, is the resistance from the anode surface to the cathode surface. Typically this resistance is negligible if the cathode and anode are in direct contact with each other or if they are connected electrically by other means [29]. Equation 1.1 is a theoretical relationship that provides valuable insight into modeling galvanic corrosion, but in practice there are complicated interactions between the different factors [29] that make determining proper values for the resistive elements difficult.

Despite the difficulty associated with obtaining accurate resistive element values, the following parameters can be considered during part design and used to increase the resistive elements, thereby reducing galvanic corrosion:

1. The presence of an insulator between conductors (if any) [30].
2. The composition the electrolyte fluid and/or thickness of the electrolyte film [29].
3. The thickness and composition of protective non-conductive coating covering the anode and cathode [32].
4. The ratio of anode surface area to cathode surface area.

Keeping these factors in mind when designing a multi-material part can result in a minimal corrosion rate, even when the two conductors have vastly differing electric potentials.

A classic design for corrosion mitigation is to insert a thin non-conductive material between the two conductive materials of interest. The insulating material then acts as a galvanic current barrier, preventing dissolution of metal at the anode. In the case of carbon fiber to metal adhesive lap joining this barrier has traditionally been achieved by the adhesive used in bonding. This is an important advantage of adhesive bonding, it offers bonding and corrosion protection in one package. However, with non-adhesive joining techniques, other insulation barriers are often necessary.

Fiberglass is one of the most common non-conductive materials used to separate CFRP and metals. This is typically done by including a fiberglass layer on the outer surface of the composite stack-up. This results in a composite with the stiffness and density of CFRP, as well as a corrosion barrier built into the structure. However, depending on the severity of the part environment and the joint design, galvanic corrosion can still be a problem if the CFRP and metal are in electrical contact with one another by other means. Figure 1.6 shows an example of a part that is susceptible to corrosion even with a fiberglass barrier layer [30]. In this case, the conductive fastener creates a path for galvanic current between the CFRP and the aluminum. Given the fastener, if an electrolyte is in contact with both aluminum and CFRP surfaces, galvanic corrosion will occur. The electrolyte salt bridge shown in Figure 1.6 was formed due to salt spray corrosion testing completed on the part.

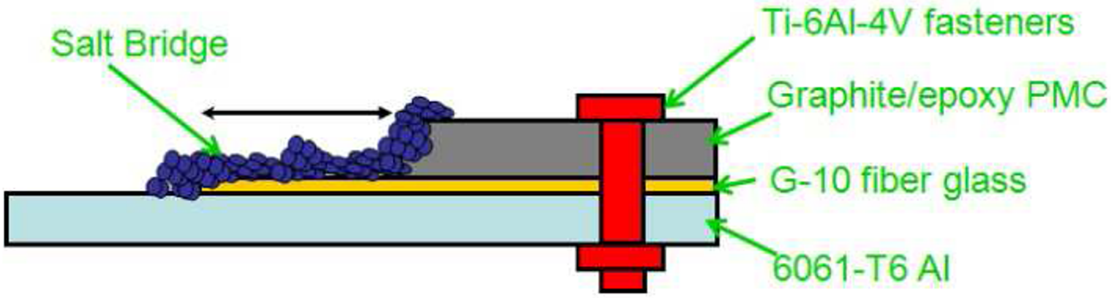

Figure 1.6: CFRP/aluminum joint with fiberglass corrosion barrier [30].

For automotive applications, working conditions can be severe due to high humidity, rain, snow, salt water [29], and chloride in the air [33]. Each of these environments produce thin electrolyte films over exposed parts. One way to prevent galvanic current from traveling through the anode/cathode couple is to use a protective coating on the outer surface of either the anode or cathode, providing a barrier to the electrolyte film. In the case of CFRP, epoxy or other non-conductive matrix materials used to create the carbon fiber composite also coat the exterior of the CFRP. Studies have shown that the thickness of this coat of epoxy is influential in determining the galvanic corrosion rate [32]. Figure 1.7 shows the galvanic current rate for four different test pieces which were tested in both seawater and deicing salt solution. Adding a typical coat of epoxy (0.25 mm) to the outside of a specimen with bare CF resulted in a 95% decrease in galvanic corrosion rate. With regard to epoxy coating thickness, using the typical coating thickness of 0.25 mm resulted in a 79% lower galvanic current than using a thinner coating of 0.1 mm.

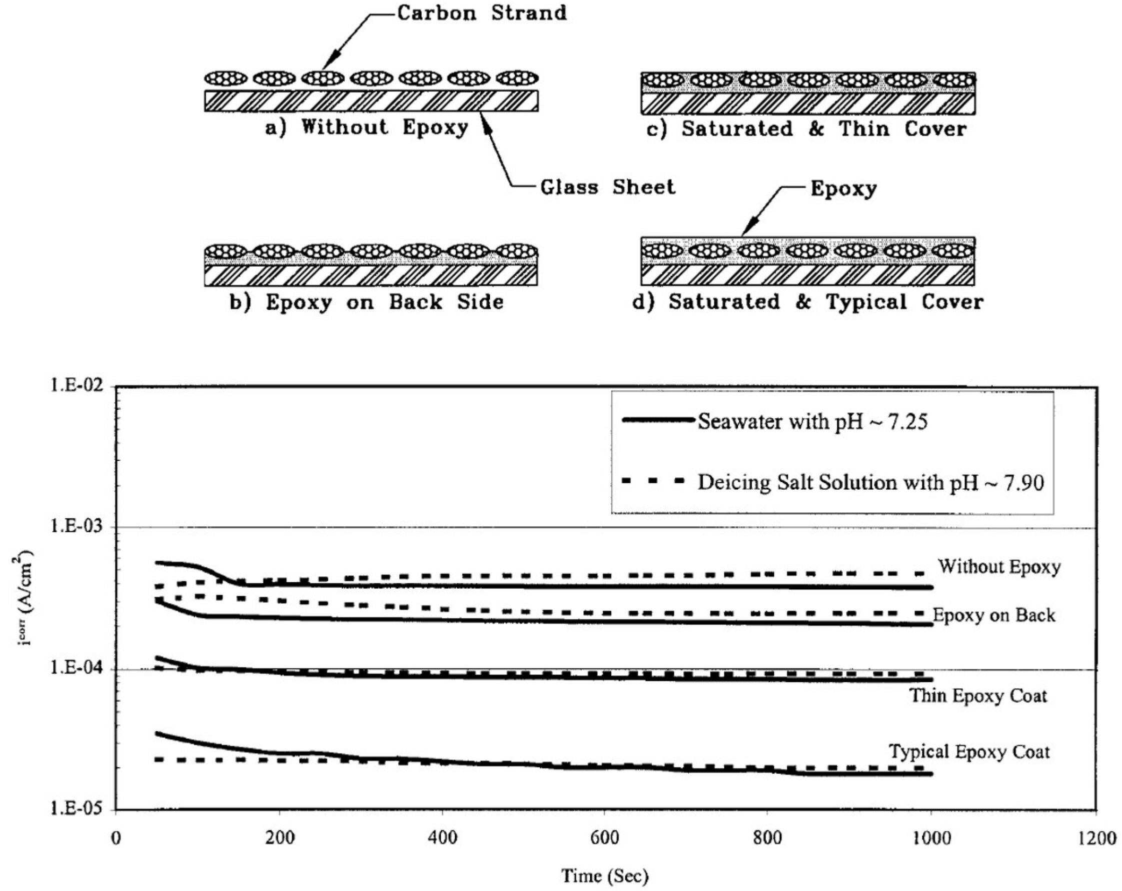

Figure 1.7: Effect of epoxy coating over carbon fiber/steel couples. [32]

A common testing method used to accelerate galvanic corrosion is salt spray testing. For this testing process, the part of interest is placed in a chamber and misted with a saline spray in order to create a continuous electrolyte film on the outside of the part. For salt spray testing, the metric used to determine the severity of the corrosion is often purely qualitative, given by a visual inspection. A common quantitative metric sometimes used with salt spray testing is mass reduction. Mass reduction occurs due to the dissolution of the galvanic couple anode into the electrolyte. Mass reduction can be linked to galvanic current, shown in Equation 1.2 [33].

$$I_{galv} = \frac{Fn\Delta m}{AW\Delta t} \tag{1.2}$$

Here, an estimate of the galvanic current can be made knowing the reduction of mass, Δm, the valency of the anode, n, Faraday's constant, F, the change in time, Δt, and the atomic weight of the anode, AW.

Other common methods used to predict the severity of galvanic corrosion are accomplished by finding potentiodynamic polarization curves of each material in the galvanic couple and estimating the corrosion rate using the superimposed curves, often referred to as an Evans diagram [32]. While methods as described can be helpful to predict how susceptible a particular couple will be to galvanic corrosion, in real world applications there will be other factors playing into the corrosion rate. The electrolyte properties, surrounding environment, and part coatings are not factored into such an experiment, making realistic tests more valuable.

To summarize this section on CFRP to metal galvanic corrosion, graphite and highly anodic metals are not an ideal pairing for corrosion prevention. However, long lifespan joints of these materials can be orchestrated by careful joint design and use of galvanic current barriers, i.e. surface coatings and non-conductive separation between anode and cathode.

1.1.5 Ultrasonic Additive Manufacturing

Ultrasonic Additive Manufacturing (UAM) which is also referred to as Ultrasonic Consolidation (UC) is a manufacturing process that uses additive and subtractive steps to create unique, three-dimensional structures from metal foils. The UAM method has been used to create multi-functional structures with unique internal geometries and internal integration of wiring, electronics, and fiber optics [28]. UAM is often performed from a machine tool which is used in a Computer Numeric Control (CNC) manufacturing center. UAM was first commercially introduced by Solidica Inc. [28]. The Solidica Formation machine incorporated a metal welding head (sonotrode) equipped with an automated tape feed, a standard 3-axis milling head, and software to automatically control tool paths for both the weld head and milling head [28]. Pictured in Figure 1.8, the weld head is treated by the CNC machine as a tool and is used to additively join metal foils to create desired builds.

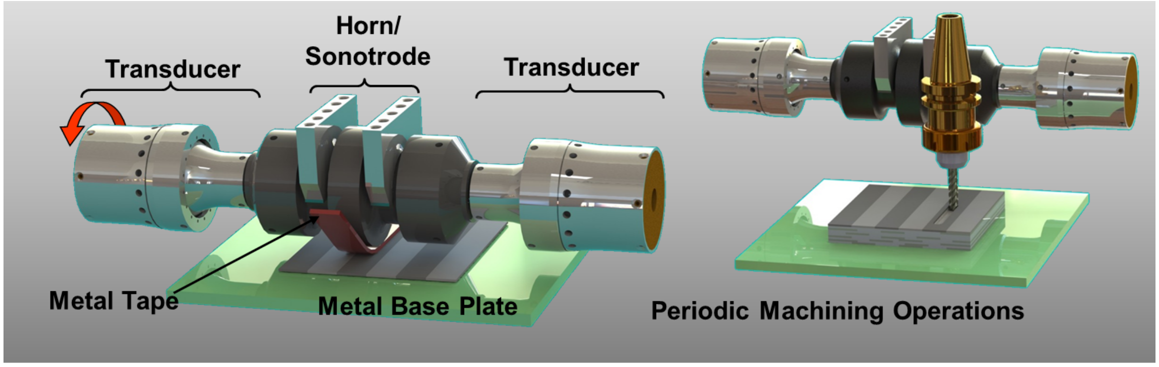

Figure 1.8: UAM system tools for ultrasonic welding and milling operations. (Courtesy of Fabrisonic)

An important characteristic of UAM is that the temperature at the weld interface during the joining process typically does not exceed 30%-50% of the melting temperature of the metal [23]. This unique low temperature joining creates possibilities for embedding temperature sensitive fibers and materials with little to no damage.

Another unique aspect of UAM is that highly localized plastic flow is possible around embedded structures [25]. This capability coupled with the low temperatures of welding make UAM an excellent method for embedding many types of materials within a metal matrix.

The UAM process has been used successfully with a variety of metals including Al, Ni, Ti, Ag, Cu, Ta and others as well as joining of many combinations of dissimilar metals [24]. Regardless of material, the same principles in UAM are at work to create joining between the metal layers. Figure 1.9 illustrates the basic principles of UAM. In the process, a rotating sonotrode travels over the length of the weld. A thin metal foil is placed under the sonotrode as it travels over the work piece. The base substrate is secured by the mill table which is often equipped with a vacuum chuck. Transducers create a 20 kHz signal which drives the sonotrode at the amplitude specified by the operator transverse to the foil layup direction. As the sonotrode moves over the work piece, it is pushed into the two joining materials by the weld tool at a specified loading. The surface of the sonotrode is textured in a manner such that it grips the metal tape forcing the two adjacent surfaces to move relative to each other at 20 kHz and at a specified amplitude. The combination of normal and shear forces result in a scrubbing action causing dynamic interfacial stresses at the foil/base interface. These stresses produce high plastic deformation of surface asperities which effectively break up the oxide layer leading to metallurgical bonding between the metal layers [28]. Further layers can be welded over the first layer of foil until the desired build thickness is achieved. During the construction process, the UAM center's milling tool can be used to remove material from the structure. This machining capability makes complex internal geometries and embedding dissimilar materials possible. After all necessary foils have been welded, further machining can be done to complete the part.

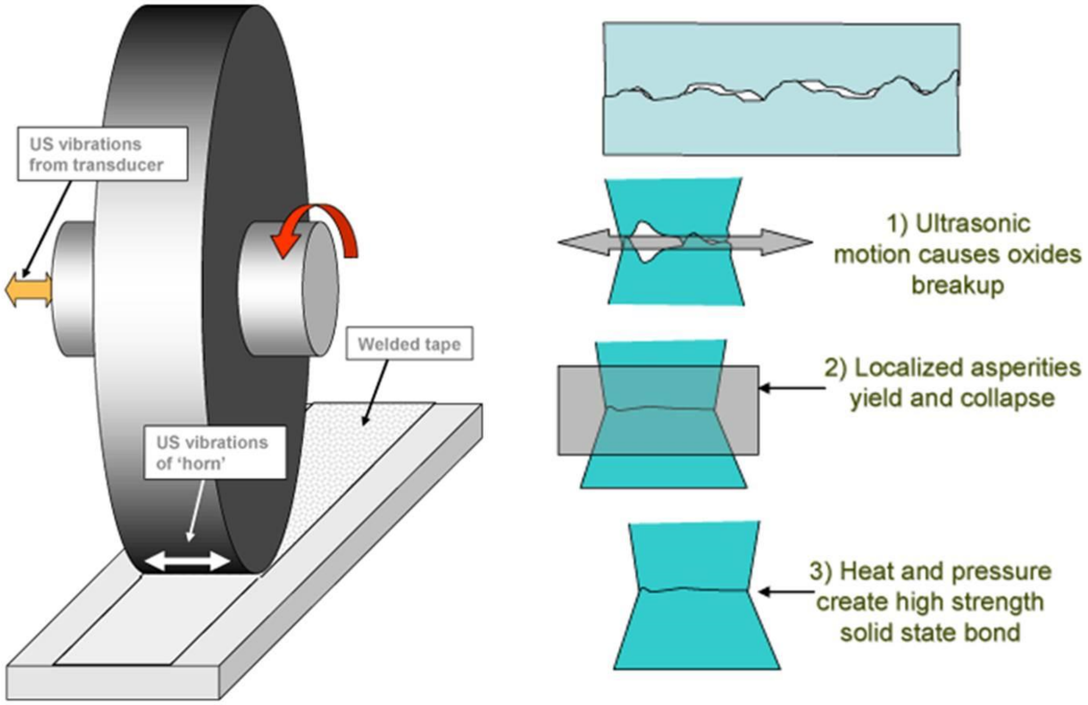
US vibrations from transducer
Welded tape
US vibrations of 'horn'
1) Ultrasonic motion causes oxides breakup
2) Localized asperities yield and collapse
3) Heat and pressure create high strength solid state bond

Figure 1.9: Basic principles of UAM (courtesy of Fabrisonic).

Much like ultrasonic metal welding, the UAM process has a number of parameters which affect the quality of the additive foil process. The parameters can be altered per specific application to render robust joining between the foils and/or embedded structures. The typical parameters include: normal force, sonotrode amplitude, weld speed, baseplate temperature, and sonotrode roughness. The normal force is applied by the welding tool and is monitored by a load cell within the welding assembly. Sonotrode amplitude is the peak to peak movement of the horn driven by the transducers. The amplitude can easily be altered by the operator. The frequency of the oscillation, however, cannot be altered because it is dictated by the sonotrode's operating resonant frequency. This frequency is usually near 20 kHz for UAM applications. Rolling speed is the rate at which the sonotrode roles over the metal foils during the welding process. Many UAM systems are equipped with the option of a heated baseplate. The temperature is controlled by a heating element in the anvil of the UAM system. Lastly, the sonotrode will have a specified surface roughness which is created by wire EDM. This surface roughness can be changed by re-texturing the sonotrode. This process is often necessary after a sonotrode's surface becomes worn from repeated use. The roughness of the horn is necessary because it provides friction necessary to grip the foil to be joined. There are different levels of roughness that can be used depending on the application with a common roughness being 14 $\mu m Ra$.

UAM systems used today include first generation models capable of power up to 1 kW to more recent very high power (VHP) UAM systems that can provide 9 kW of power. The VHP-UAM systems were developed at Edison Welding Institute (EWI) located in Columbus, OH. VHP-UAM systems have increased capabilities for greater normal force and oscillation amplitude. This improvement over the original lower powered systems allows for superior joining with aluminum and steel and makes bonding high strength metals such as titanium and stainless steel possible. Figure 1.10 shows a VHP-UAM system used by the Smart Materials and Structures Laboratory at The Ohio State University.

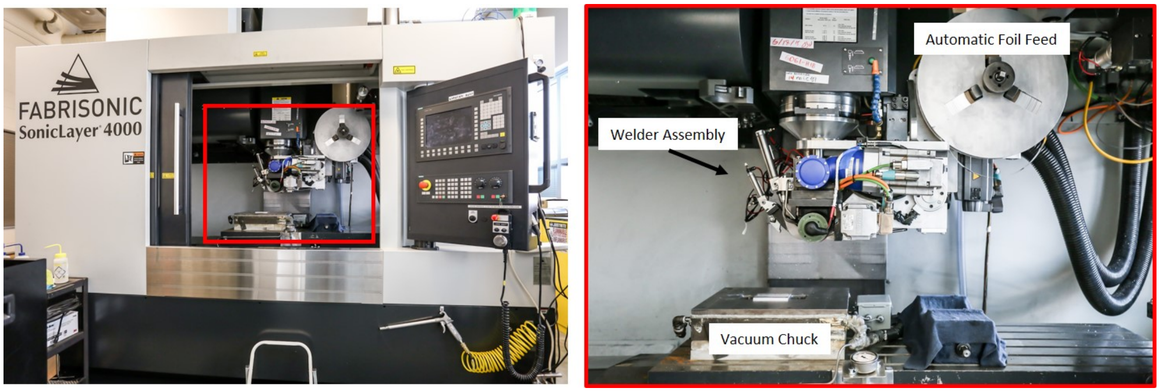

Figure 1.10: VHP UAM system used by the Smart Materials and Structures Laboratory at The Ohio State University.

Since UAM is an emerging process, there is ongoing work being done in examining the fundamentals of the process. Current research includes optimizing techniques and parameters to achieve strong bonding between foil layers. This research includes characterizing methods and parameters for a variety of materials.

Since UAM is an emerging process, there is ongoing work being done in examining the fundamentals of the process. Current research includes optimizing techniques and parameters to achieve strong bonding between foil layers. This research includes characterizing methods and parameters for a variety of materials. One common technique used for interlaminate strength evaluation is push-pin testing. Push-pin tests are conducted by pushing a pin into the surface of a prepared test specimen as show in Figure 1.11. During testing to failure, load and displacement and recorded for analysis. The push pin method can also be combined with finite element analysis to establish correlations between the push pin results and the ultimate strength of the bonded layers [40].

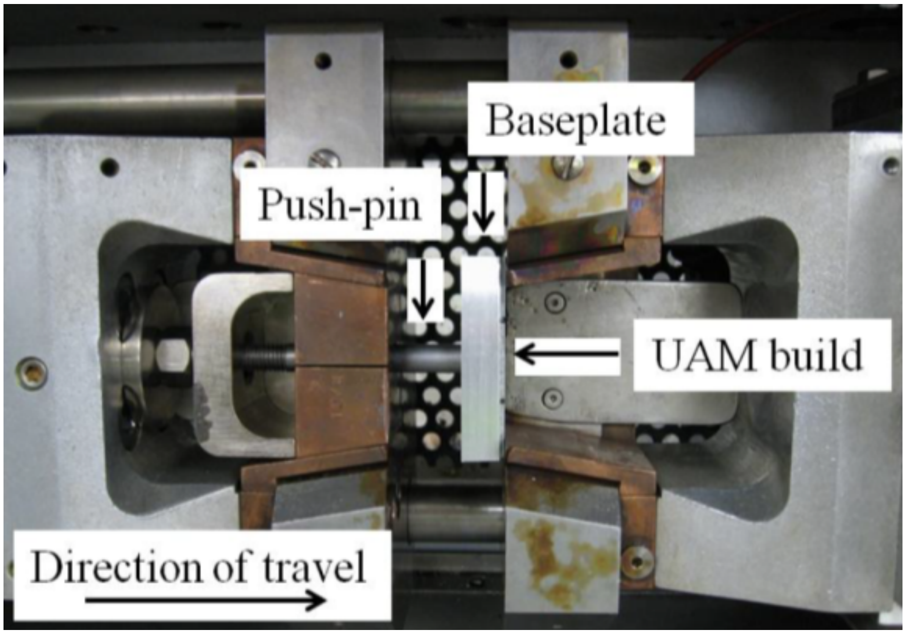

Figure 1.11: Push pin test for testing UAM welded layer bonding [34].

Another common mechanical testing method for determining layer bond strength is traditional shear and tensile testing. Force and displacement data is recorded to determine the bond strength. For tensile testing, one requirement of this method is the strength of the adhesive media used to join the gripping structure to the test specimen must exceed the strength of the bonded layers. This requirement can be avoided by creating an entire dog-bone test specimen of bonded layers as seen in Figure 1.12 [20].

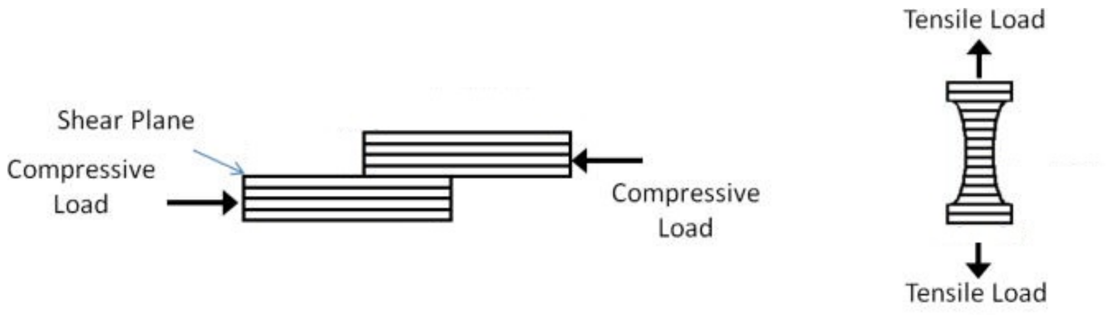

Figure 1.12: Shear and tensile mechanical testing of UAM welded builds [20].

1.2 Objectives

As discussed in Section 1.1.5, the UAM process can be used to embed dissimilar materials within a metal matrix. Given the unsatisfactory performance of joining methods currently used in industry for integrating CFRP structures with metal structures, there is a need for alternative joining techniques. The purpose of this research work is to develop a method using ultrasonic additive manufacturing to join CFRP with aluminum. The end goal of this research is to develop CF-Al joints whose performance is superior to the current state-of-the-art joining methods (i.e. adhesive joining) in strength and durability. These joints also need to be manufactured affordably and with minimal changes to existing industry infrastructure.

Though the UAM process can be used with a number of different metals, the current competency of welding aluminum is far greater than welding other metals. For this reason, 6061-H18 aluminum is the primary metal used for developing CFRP to metal joints. In later phases of this work, joining CFRP to other metals such as steel may be explored. However, before work on integrating CFRP with higher strength metals, greater expertise in using UAM with these metals is necessary.

The metrics used to compare joint performance of different UAM CF-Al joints include several types of mechanical testing. These tests include tensile, cross tensile, and three-point-bend testing. These mechanical testing methods are also used to compare the performance of UAM CF-Al joints with adhesive single lap CF-Al joints. Other metrics which have also been used to evaluate joint characteristics include cross section imaging and corrosion testing paired with visual inspection and mechanical testing.

Another objective of this work is to improve upon UAM processes necessary for creating CF-Al joints. The importance of placing a strong focus on developing the manufacturing process can not be overstated. While developing CF-Al joints is the primary focus of this research, without proper manufacturing processes in place, the joint development is not possible. Part of the manufacturing process includes embedding carbon fiber tows between layers of aluminum. A common problem that is encountered when embedding CF is a phenomenon called foil tearing which must be avoided at all costs. Experimental data and observations were used to predict the root cause of foil tearing. FEA modeling was then used to provide further insight into the issue and formulate foil tearing mitigation solutions.

Chapter 2: EMBEDDING CARBON FIBER WITHIN METALS USING UAM

2.1 Embedding CF into 6061-H18 Aluminum

Critical to UAM CF-Al joint design is the concept of embedding carbon fiber tows within metal. Depending on the joint design, embedding the fibers can create mechanical interlocking between the CF and surrounding metal. Regardless of the joint design, embedding CF tows increases the adhesive surface area when the CF is laid up with epoxy, leading to improved joint performance. The initial efforts with CF-Al joining focused on determining techniques to effectively embed the CF without damage to the CF or aluminum components.

The carbon fiber used for throughout the entirety of this work is HexTow AS4C 4000 3K tows produced by Hexcel. The aluminum foil used with the UAM process throughout this work is 6061-H18 in a rolled foil form of thickness 0.1524 mm (0.006") and width 24.5 mm (1").

2.1.1 Consolidation Preparation and Process

Up to this point, there has been no literature on embedding CF tows within metal using UAM, but the UAM process has been used to embed other fiber-like materials such as nickel titanium wires [19]. Similar tactics were used for embedding the CF tows.

After some initial trial and error experimentation, it was found that the CF could be consolidated with minimal damage into 6061-H18 Al by using 3.2 mm (0.125") wide channels to house the CF tows. The channel depth used was 0.127 mm (0.005"). A sequence of CF tows being embedded is shown in Figure 2.1. First, several layers of aluminum foil were welded onto a small baseplate. Next, channels were cut into the UAM base layers. CF tows were then placed into the channels. Isopropanol was used to densify the CF tows and help work them into the channels neatly. Finally, the UAM process was used to weld additional layers of 6061-H18 foil over the CF tows. The UAM process parameters used during these early CF-Al builds are shown in Table 2.1. More details of early CF tow consolidation can be found in Bryant Gingerich's undergraduate thesis [16].

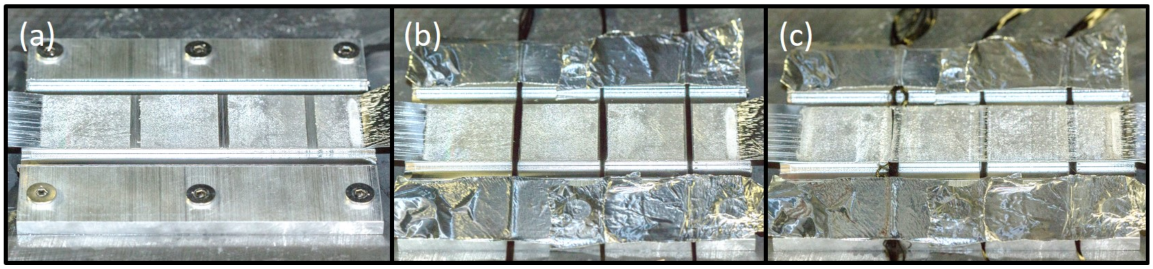

Figure 2.1: CF consolidation sequence. (a) Channels are cut into base 6061-H18 Al layers, (b) CF tows are placed into the channels, (c) layers of 6061-H18 Al foil are welded over the CF tows.

Table 2.1: UAM parameters used for single CF tow consolidation.

Welding Force	5000 N
Welding Speed	508 cm/min
Amplitude	32 μm
Heat-plate Temperature	Room Temperature (22 C°)
Spot Dwell	250 ms

2.1.2 Cross Section Micro-imaging Results

Some early attempts at embedding CF tows did not use channels to house the fibers which resulted in the fibers being severed at the edge of the aluminum foil. Despite this fact, micro-images suggest that other than a few cracked fibers, there was little damage to the embedded CF within the aluminum structure (Figure 2.2).

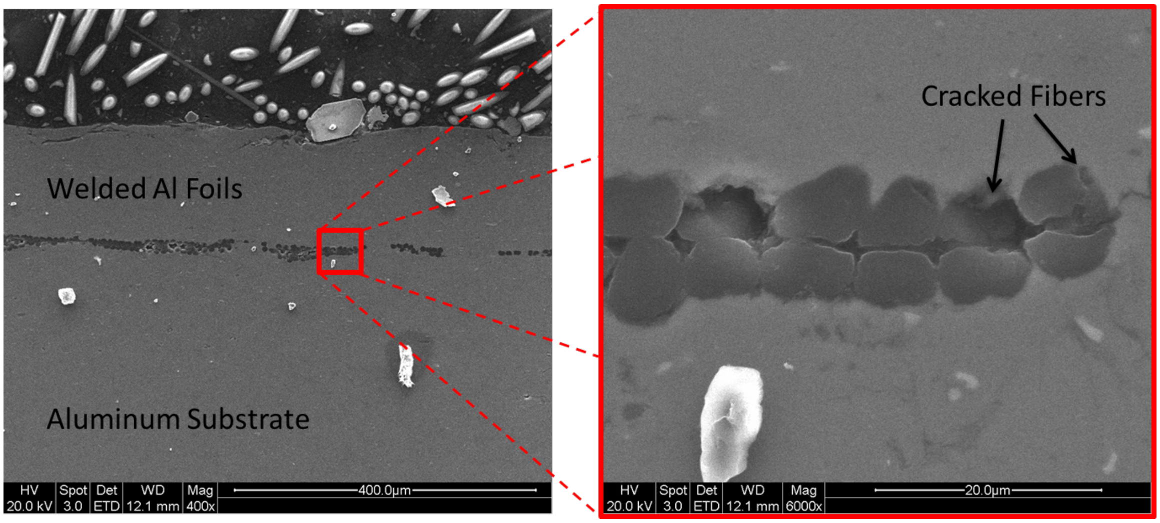
Welded Al Foils
Aluminum Substrate
HV 20.0 kV Spot 3.0 Det ETD WD 12.1 mm Mag 400x
400.0µm
Cracked Fibers
HV 20.0 kV Spot 3.0 Det ETD WD 12.1 mm Mag 6000x
20.0µm

Figure 2.2: Images of an early attempt at consolidating CF tows without the use of channels to house the fibers.

The first successful CF consolidation without severely damaging the CF at the aluminum foil edge used channels to house the fibers as was shown in Figure 2.1. SEM micro-images of the consolidated CF suggests that the embedded CF was not damaged (Figure 2.3). However, the micro-images clearly show void spaces between some of the CF filaments. The micro-images also show that the aluminum underwent plastic deformation around the periphery carbon fibers, causing mechanical interlocking at the CF-Al interface.

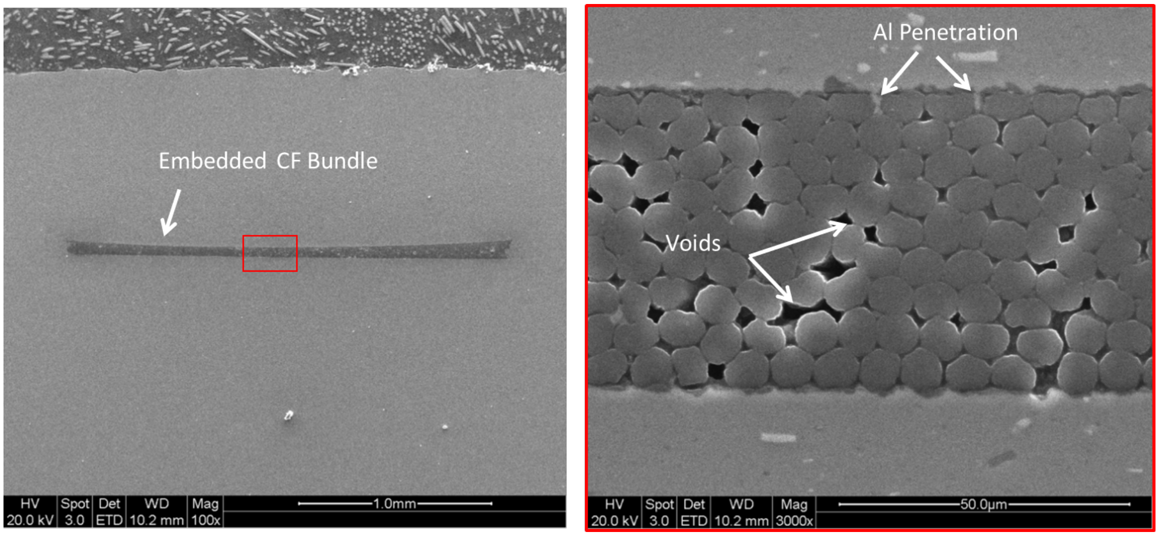
Embedded CF Bundle
HV 20.0 kV Spot 3.0 Det ETD WD 10.2 mm Mag 100x
1.0mm
Al Penetration
Voids
HV 20.0 kV Spot 3.0 Det ETD WD 10.2 mm Mag 3000x
50.0μm

Figure 2.3: SEM micro-images of a CF tow which was housed in a channel during consolidation.

2.1.3 Mechanical Pullout Testing on Embedded CF Tows

For initial joint strength evaluation, pullout testing was chosen to determine the interfacial joint strength of the single embedded carbon fiber bundles which were discussed in Section 2.1.1. To create the test specimens, single CF bundles were consolidated as described in Section 2.1.1 and then machined out of the welded build, shown in Figure 2.4. During testing, the largest stresses occur within two bundle diameters from the front edge of the joint [22]. To be safe, the length of the CF to aluminum joint interface was set to five times of the effective CF bundle diameter (2.54 mm). Wood veneers were added to the free end of the carbon fiber tows to avoid crushing from the tensile loading grips.

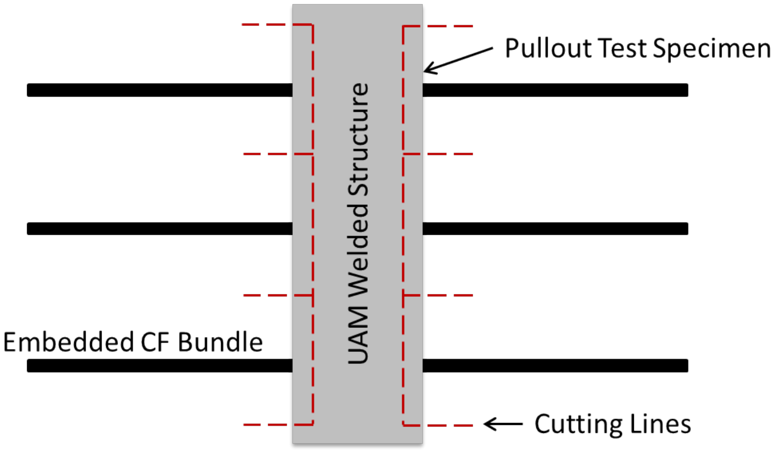

Figure 2.4: Schematic showing pullout test specimen construction.

A small load frame equipped with wedge type mechanical grips and load accuracy of 1.3 N was used to perform the pullout test. To hold the welded joint end of the specimen, a custom test fixture was used. This fixture had been used previously for interfacial strength testing of embedded NiTi fibers [19].

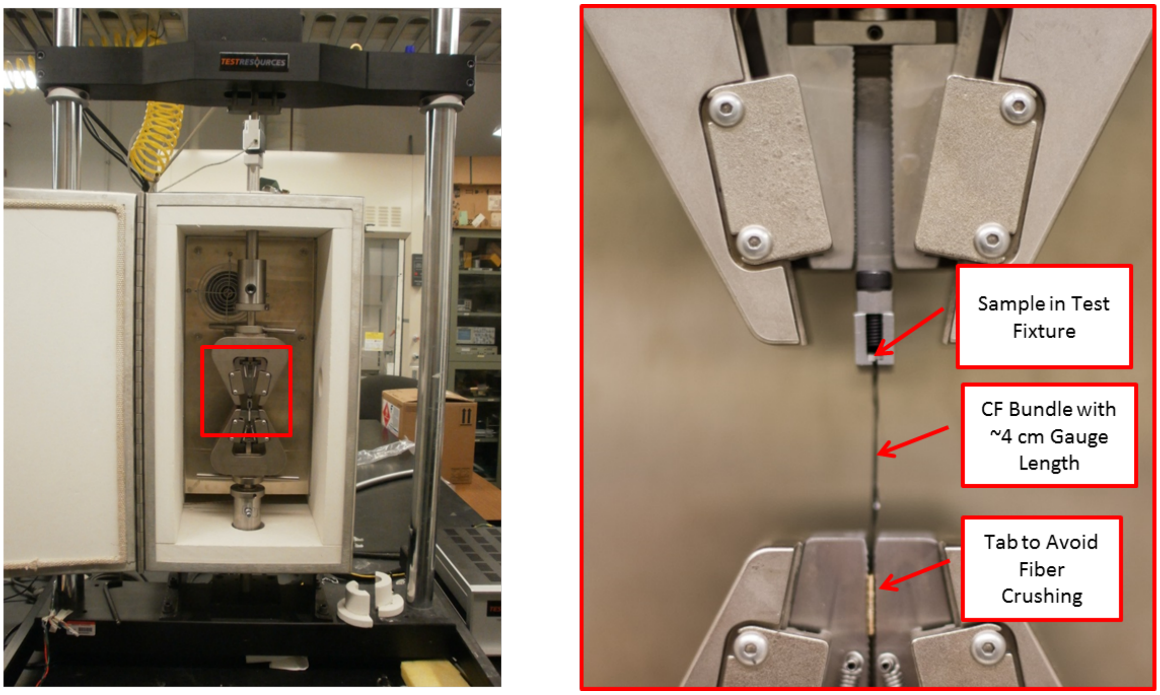
Sample in Test Fixture
CF Bundle with ~4 cm Gauge Length
Tab to Avoid Fiber Crushing

Figure 2.5: In house load frame with pullout fixture for embedded fiber pullout strength test.

The first pullout testing was done on embedded dry CF. These pullout strength results were poor with a load of only 20 N before pullout occurred. The fiber tows did not pull out cleanly, with the fibers around the edges of the tows breaking off and the interior fibers pulling completely out of the joint. This implies that periphery fibers were carrying the bulk of the load since when dry, the outer carbon fibers are not coupled well with the inner carbon fibers.

A second pullout test was completed as before, but each embedded CF tow was wet with epoxy. Micro-images show that the consolidated CF tows feature small voids between fibers which allow epoxy to wick deep within the embedded CF due to surface tension effects (Figure 2.3). This allows for more equal load distribution between the carbon fibers since they are held together with the epoxy. The second pullout test results showed that the joint strength increased by an order of magnitude when compared to the dry CF pullout strength (Figure 2.6). The average pullout strength for the joints wetted with epoxy was 10.9 MPa.

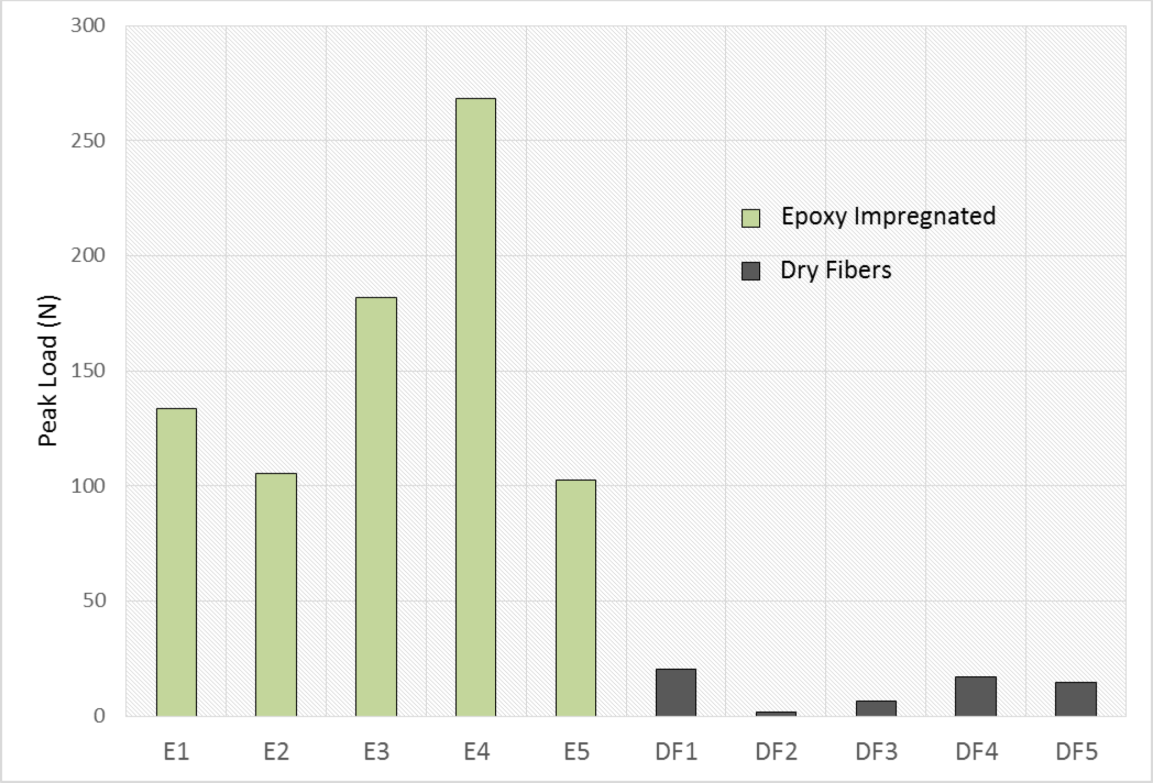

Figure 2.6: Pullout strength of epoxy impregnated joints compared with the strength of dry joints.

While impregating the CF tows with epoxy caused a large increase in pullout strength, the test specimens with epoxy did not all fail in the same manner, shown in Figure 2.7. The cause of the different failure modes is likely due to variance in the channel depth used to house the CF during the consolidation process. This is discussed in greater detail in Bryant Gingerich's undergraduate thesis [16]. The failure modes observed among the epoxy wetted pullout specimens include the following:

1. Clean pullout of bundle - Figure 2.7(a)
2. No joint failure, failure within the CF bundle - Figure 2.7(b)
3. Brittle fracture near the front edge of the joint - Figure 2.7(c)

Pullout specimen, E4, did not fail within the CF-Al joint region, but in the center of the CF gauge length. This test specimen demonstrated that under the correct parameters an embedded carbon fiber joint can be stronger than the carbon fiber itself.

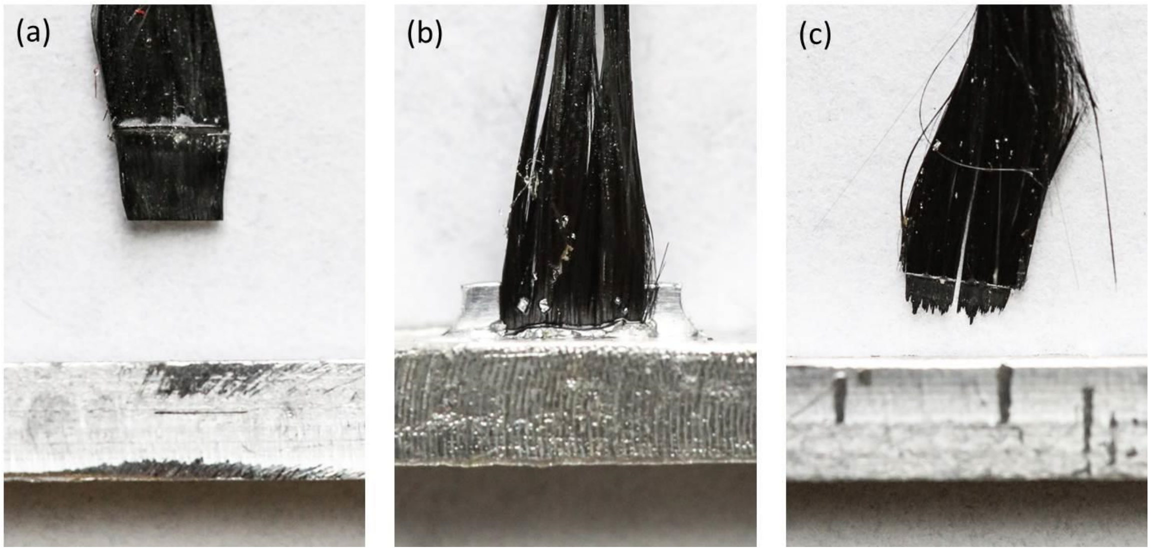

Figure 2.7: Three different failure modes seen in CF - Al pullout specimens wetted with epoxy. (a) Specimen E3, complete pullout from joint; (b) Specimen E4, failure in the fiber gauge length - no joint failure; (c) Specimen E5, brittle failure near the front edge of joint.

2.2 Embedding Nickel Coated CF into 6061-H18 Aluminum

Further CF consolidation experimentation was completed with nickel coated CF tows. The original thought was that since each carbon fiber strand is surrounded by a thin electro-plated coat of nickel, metallurgical bonding between the nickel and surrounding aluminum would be plausible.

2.2.1 Consolidation Preparation and Process

The consolidation process used to embed nickel electroplated CF was similar to that described in Section 2.1. However, there were some differences in channel width and depth. The channel width was reduced because of issues with foil tearing, a phonomenon that will be discussed in Chapter 5. The electro-plated CF tows also had a greater cross sectional area than the 3k Hexcel tows used throughout the bulk of this research work. This fact paired with reducing the channel widths to 1.8 mm (0.070") lead to a greater channel depth of 0.25 mm (0.10"). The weld parameters used to consolidate the nickel coated CF are shown in Table 2.2. Figure 2.8 below shows nickel coated CF pullout specimens before and after fiber consolidation.

Table 2.2: UAM parameters used for single nickel electroplated CF tow consolidation.

Welding Force	5000 N
Welding Speed	508 cm/min
Amplitude	32.5μm
Heat-plate Temperature	Room Temperature (22 C°)
Spot Dwell	250 ms

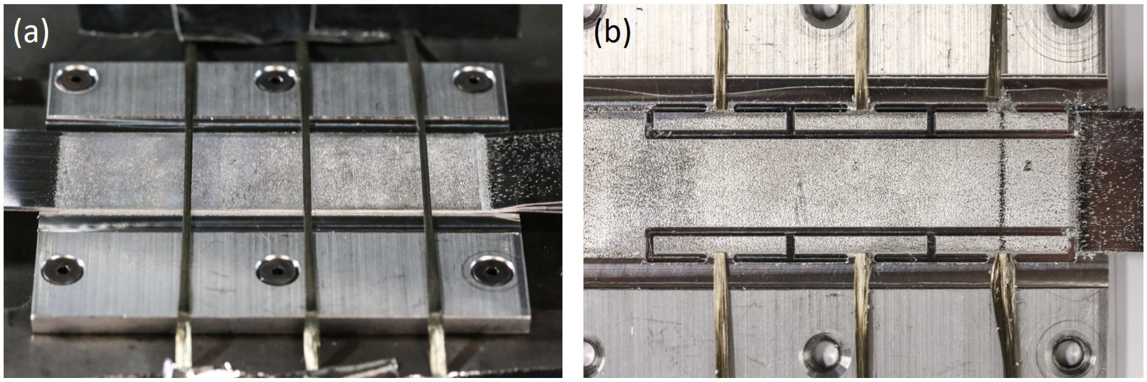

Figure 2.8: Consoliation nickel coated CF tows. (a) CF placed in the channels, (b) CF embedded and pullout specimens cut out.

2.2.2 Cross Section Micro-imaging Results

Cross sectional images of embedded nickel plated CF show that the consolidation process did not harm individual fibers or their nickel coatings (Figure 2.9). Similar to micro-images taken of embedded uncoated CF, void space between individual fibers is present throughout. The primary intention of embedding nickel plated CF was in pursuit of metallurgical bonding between the nickel coatings as well as between the nickel and surrounding aluminum bulk material. The micro-images neither confirmed or denied this possibility, though pullout testing later showed that metallurgical bonding was not present. It is likely that metallurgical bonding could occur given the right circumstances, e.g. consolidation without channels and higher welding amplitudes, but these circumstances would be impractical for CFRP to aluminum joining.

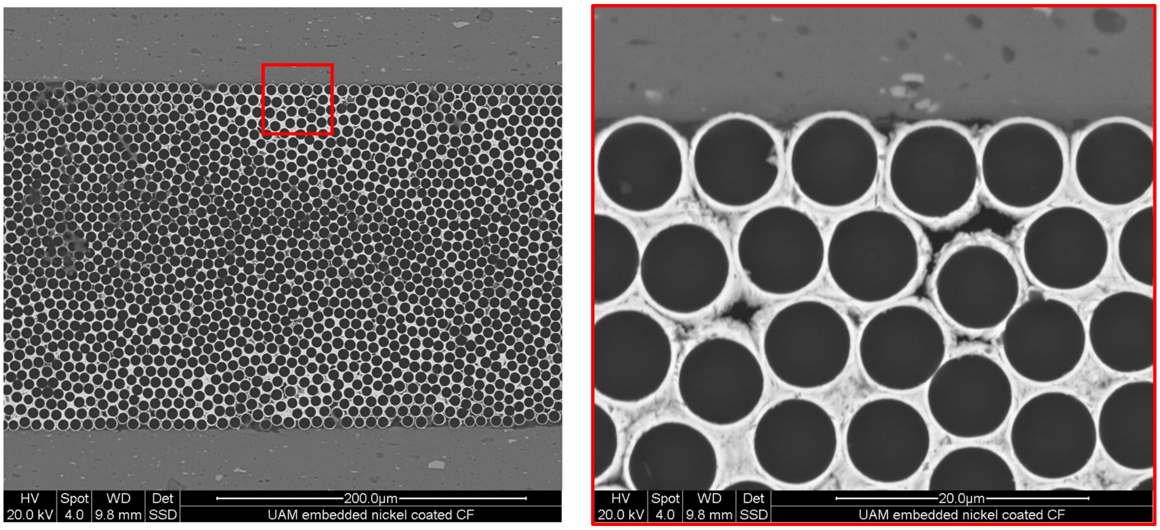
HV
20.0 kV
Spot
4.0
WD
9.8 mm
Det
SSD
200.0μm
UAM embedded nickel coated CF
HV
20.0 kV
Spot
4.0
WD
9.8 mm
Det
SSD
20.0μm
UAM embedded nickel coated CF

Figure 2.9: SEM micro-images of consolidated nickel coated CF.

2.2.3 Mechanical Pullout Testing on Embedded Nickel Coated CF Tows

In addition to micro-imaging, pullout specimens were constructed featuring the consolidated nickel electro-plated CF. The pullout specimens were designed similarly to those described in Section 2.1.3. Figure 2.5 shows the pullout specimen design. For the nickel coated CF pullout tests, three different cases were considered: pullout of dry nickel coated CF, pullout with the joint wetted with epoxy, and pullout with the joint wetted with ultra-thin superglue. Figure 2.10 shows load vs. displacement curves for each case. The specimens with super glue had the highest pullout force, though they began to pull out at a lower displacement than the epoxy case. Unlike earlier pullout tests with uncoated CF, the dry case produced a fairly large pullout force, slightly greater than the epoxy case in-fact. This stark difference from earlier pullout tests with uncoated CF is probably due increased friction between the individual fibers because of the nickel coating. Earlier tests with uncoated CF had very little friction between individual fibers since CF structure is essentially graphite, which can work as a lubricant.

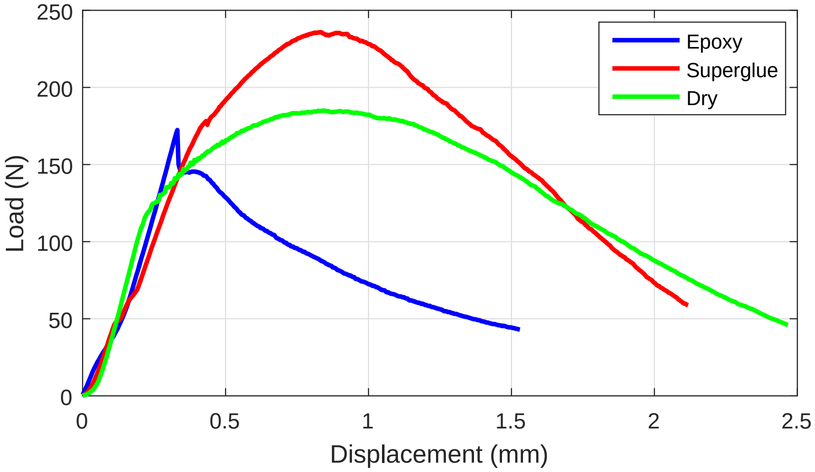

Figure 2.10: Pullout test results for nickel coated CF tows with different wetting conditions.

Additional pullout testing was completed on five other nickel coated CF specimens with epoxy as the wetting agent. The average peak interfacial joint stress was 13.2 MPa. This was slightly greater than the average peak interfacial joint stress for non-coated CF pullout specimens which was 10.9 MPa. However, the two pullout testing results are not completely comparable, since the channel widths and depths were not identical across the two designs.

In conclusion, consolidated nickel coated CF showed slightly greater resistance to pullout (especially in the dry state). Micro-images showed that the individual fibers and their coatings were not damaged from the embedding process, though metallurgical bonding was not confirmed. Though consolidation of these fibers shows promise, efforts throughout the bulk of this research has remained focused on uncoated CF since nickel coated CF is far more expensive and would not be a cost effective choice if adopted by industry.

2.3 Embedding CF into 4130 Steel using 201 Nickel as Interlayers

2.3.1 Welding 4130 Steel using 201 Nickel Interlayers

The current UAM manufacturing process is most effective and understood when welding aluminum. However, there is a vested interest in joining CFRP to high strength steel from industry, making joining CF-steel a future goal for UAM development. Welding steels via UAM is difficult because the sonotrode material is made out of tool steel. Since the steel sonotrode has an affinity toward the steel foil layers, nuggeting or welding to the sonotrode is a common problem. One way to help avoid welding to the sonotrode when welding with steel is to utilize nickel interlayers between the steel foil layers.

In this case, 201 nickel interlayers were used. 201 nickel is a nearly pure nickel alloy and has a much lower yield strength than the 4130 steel foils. Properties of the nickel and steel foils used are shown in Table 2.3. Due to the lower yield stress, the nickel interlayers undergo much more deformation than the steel foils as shown in the micro-image in Figure 2.11. The steel/nickel layers were welded in one weld pass by manually laying the nickel over the base layers and using the UAM machine's automatic tape feed to feed the steel foil during welding. Many trial welds were performed before satisfactory results were achieved. The weld parameters which showed the best results are shown in Table 2.4.

Table 2.3: Properties of the steel and nickel foils.

	4130 Steel Foil	**201 Nickel Foil**
Ultimate Strength	1030 MPa	450 MPa
Foil Thickness	0.13 mm (0.005 in)	0.025 mm (0.001 in)

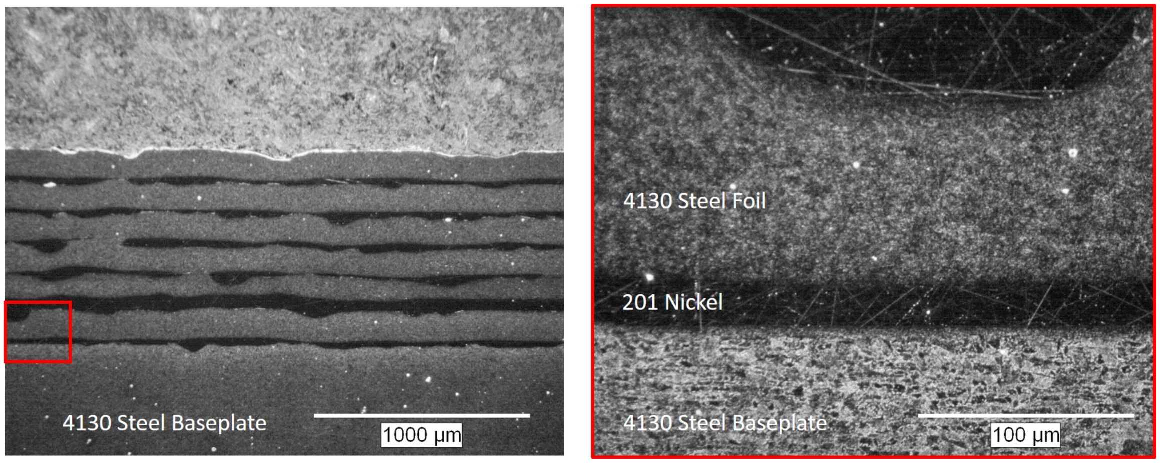
4130 Steel Baseplate
1000 µm
4130 Steel Foil
201 Nickel
4130 Steel Baseplate
100 µm

Figure 2.11: Optical micro-images of 4130 steel welded with 201 nickel interlayers.

Table 2.4: UAM parameters used when welding 4130 steel using 201 nickel interlayers.

Welding Force	8000 N
Welding Speed	203 cm/min
Amplitude	41.36μm
Heat-plate Temperature	Room Temperature (149 C°)
Spot Dwell	300 ms
Horn Roughness	14μm (fairly worn)

2.3.2 CF Consolidation Preparation and Process

Once satisfactory results with welding 4130 steel with nickel interlayers was achieved, this technique was used to consolidate HexTow AS4C 4000 3K CF tows. Five channels were cut to house the CF tows (Figure 2.12a) and were fashioned such that two CF tows could fit into each channel (Figure 2.12b). The width and depth of the channels were 1.6 mm (0.063") x 0.30 mm (0.012") respectively. The baseplate temperature used was $93C^{\circ}$. This elevated temperature did not allow isopropanol to be used to densify the CF and situate the tows into the channels, so water was used instead.

Once the CF was placed into the channels, a thin nickel foil was manually placed over the CF tows as pictured in Figure 2.12c. Finally, a layer of 4130 steel foil was welded over the nickel and CF, shown in Figure 2.12(d). The welding parameters used for embedding CF within the steel/nickel structure were slightly different than those described in Section 2.3.1. The primary reason for this is that initial trial welds require greater weld energy input than welding over existing 4130 layers as is the case for multi-laminate UAM structures. This is because the 4130 foil layers were made of a higher strength, rolled foil, while the trial welds were made over a softer 4130 annealed baseplate. The weld parameters used to consolidate CF into the steel/nickel structure are shown in Table 2.5.

Table 2.5: UAM parameters used while consolidating CF within a steel/nickel structure.

Welding Force	7000 N
Welding Speed	203 cm/min
Amplitude (Base Layers)	40.63 μm (38.18 μm Over CF)
Heat-plate Temperature	Room Temperature (93 C°)
Spot Dwell	300 ms
Horn Roughness	14 μm (fairly worn)

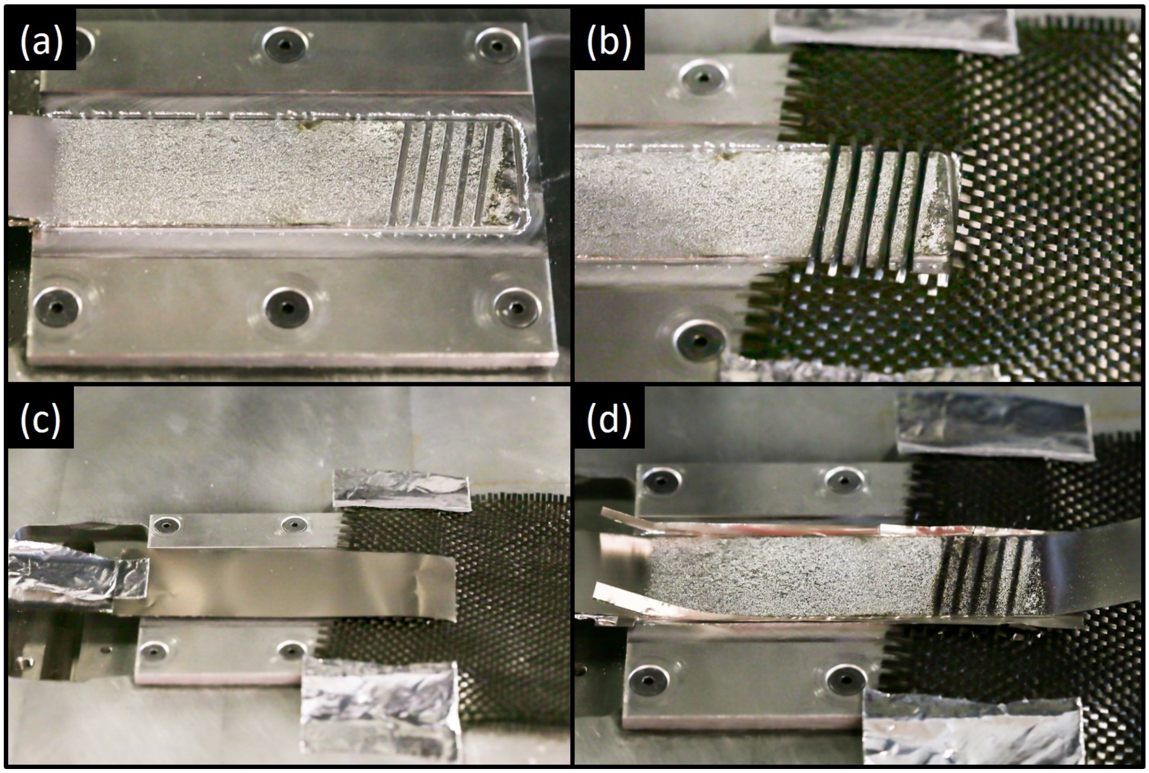

Figure 2.12: Consolidation CF into a 4130 steel/201 nickel structure. (a) Channels are cut, (b) CF placed into channels, (c) nickel interlayer placed over CF, (d) steel foil welded over nickel and CF.

2.3.3 Results and Discussion

No mechanical testing or micro-imaging was performed on the steel/nickel/CF structure. However, no damage was seen in the steel, nickel, or CF components from visual inspection. The CF tows were not completely tight in the channels. This suggests that shallower channels should be used in the future when consolidating CF into steel. This makes sense since there is less deformation of steel and nickel material into the channels when compared to the aluminum case.

Though further work on consolidating CF within steel has not been completed up to the date of this thesis, the steel/nickel/CF work discussed in this section shows an important proof of concept. In later phases of CF to metal joining work, steel will be the targeted metal. This section has highlighted methods that can be used to successfully embedded CF within steel/nickel structures.

2.4 Embedding Glass Fibers into 6061-H18 Aluminum

In addition to carbon fibers, glass fibers were consolidated into 6061-H18 aluminum. The motivation behind proof of concept work with non-conductive fibers such as glass is finding galvanic corrosion solutions for CF/Al UAM joints. One way to eliminate the galvanic couple between the CFRP and aluminum regions is to embed non-conductive fibers within the aluminum and integrate these embedded fibers with a CFRP part. This way the non-conductive fibers form an electrical current barrier between the CFRP and the aluminum.

2.4.1 Consolidation Preparation and Process

The consolidation process for embedding glass fibers is very similar to that of CF. To construct pullout specimens, channels were machined to dimensions of 1.59 mm x 0.17 mm in width and depth respectively. Single glass fiber tows from Rutan glass fabric (purchased from Aircraft Spruce Specially Co.) were removed from the fabric and situated into the channels with isopropanol. The same welding parameters used to embed the nickel coated CF were used to weld over the glass fiber tows shown in Table 2.2. After sufficient layers were welded over the glass fibers, a machining program was used to cut out pullout specimens as done in Section 2.2.1. After the specimens were removed from the baseplate, wooden tabs were added to the free ends of the glass fiber tows with epoxy to allow the load frame grips to secure the specimens without crushing the glass fiber tows. The embedded glass tows were also wet with epoxy to increase the joint pullout strength by enabling better load sharing between the fibers and adhering the fibers to the sides of the aluminum channel.

2.4.2 Mechanical Pullout Testing on Embedded Glass Fiber Tows

Pullout testing was completed using the same testing equipment as used in Sections 2.1.3 and 2.2.3. Load vs. displacement from the glass fiber pullout testing is shown in Figure 2.13. The cause for the low pullout strength when compared to CF pullout tests is not completely understood. However, these pullout specimens failed in a combined tow pullout - tow fracture mode. The fact that the glass fiber tows did not pullout cleanly suggests abrasion between glass fibers may have accelerated tow failure. If embedding glass fibers are pursued further, fully understanding the pullout failure mechanisms will need to be revisited.

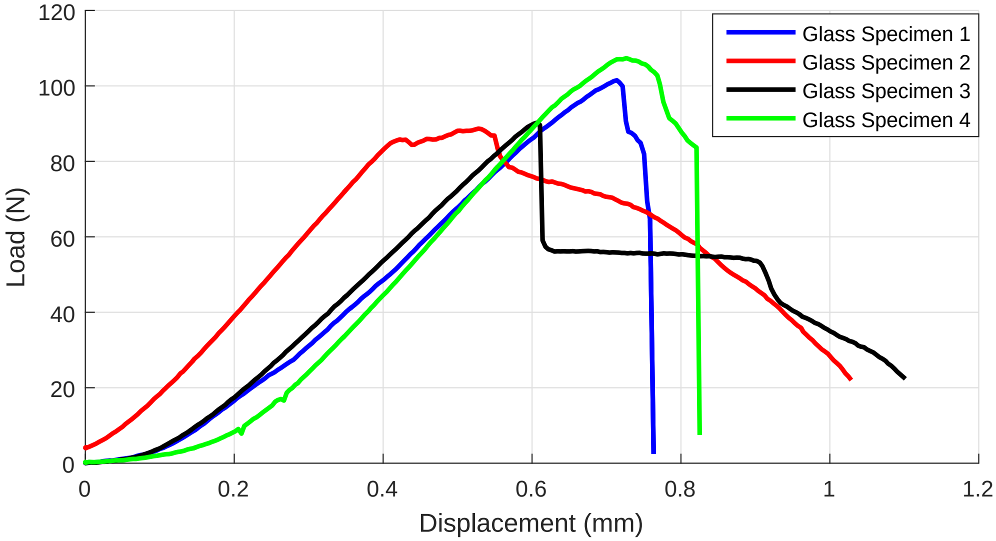

Figure 2.13: Load vs. displacement during the glass tow pullout testing.

2.5 Summary and Discussion

In this chapter, it was shown that carbon fiber tows can be embedded within aluminum using the UAM process. Furthermore, with the aid of channels for housing, successful consolidation was achieved without damaging the carbon fibers. SEM imaging verified that the embedded fibers were not crushed. The result was a CF-Al joint formed by mechanical interlocking between the fibers and aluminum, which can be strengthened by impregnation with epoxy. It was also shown that CF can be embedded within steel structures using UAM. In the case discussed in this chapter, nickel interlayers were used between the layers of 4130 steel. While embedding CF within steel is not the focus of this thesis, it is an important research area that will be explored in the future.

Pullout testing on the dry embedded CF tows showed that while the joints had sufficient strength for handling, the joint strength was weak. This was the case because of an uneven load distribution between the fibers of the tow. Only the CF on the perimeter of the embedded bundles carried load, causing them to fail and the interior fibers to pullout. After wetting the joints with epoxy, the pullout strength increased by an order of magnitude. This was the case for plain CF. However, for the nickel electro-plated CF, the maximum pullout force was actually higher for the fibers that were not wetted with epoxy. This can be explained by a higher friction coefficient between the nickel coated CF when compared to the plain CF. The important pullout strength factors include the following:

1. Mechanical interlocking or adhesive bonding between the channel walls and the periphery fibers.
2. Distribution of load between the fibers. If the fibers are all bonded together with epoxy, this load distribution will typically be even.

The experimentation and testing discussed in this chapter are important since the manufacturing and design knowledge is used in Chapter 3 to create UAM joints between CFRP and aluminum.

Chapter 3: DESIGN, CONSTRUCTION, AND TESTING OF CF-AL UAM JOINTS

This chapter describes how the consolidation fundamentals from 2 were expanded upon to create multi-layered joints which integrate CFRP with 6061-H18 aluminum. Chapter 3 walks through the development of several different joint designs, created for testing in a number of different loading conditions including tensile, cross tensile, and three-point-bending. The purpose of testing in these different loading conditions is to develop joints which are applicable in real world applications and have performance characteristics surpassing current state-of-the-art joining techniques, i.e., adhesive single lap joining. Some of the earliest UAM CF-Al joints are not covered in this thesis. Details of these early structures can be found in Bryant Gingerich's undergraduate thesis [16].

Three of the primary concerns when designing UAM CF-Al joints are increasing joint strength, maintaining a minimal joint thickness, and making the joint manufacturable. Each of these concerns are of equal importance and are the driving factors behind design decisions. A fourth concern which is touched on in Section 3.1.2 is designing for galvanic corrosion mitigation. Designing for galvanic corrosion protection is not a primary objective of this research phase, though this is an area that will be addressed rigorously in the future.

3.1 Three Layer, Straight Channel Joints

3.1.1 Joint Design and Manufacturing

One of the first UAM CF-Al joints which could be reliably manufactured featured three layers of HexTow AS4C 4000 3K CF tows embedded within the 6061-H18 aluminum structure. After the welding process, the CF tows are integrated with additional layers of bi-directionally woven CF. A schematic of the three layer, straight channel joint design is shown in Figure 3.1.

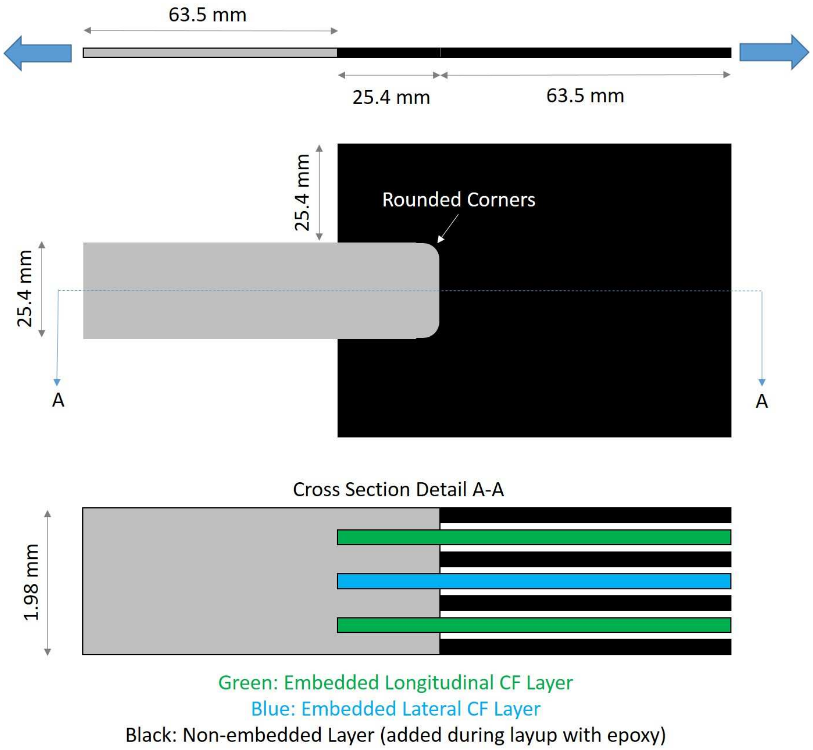
63.5 mm
25.4 mm
63.5 mm
25.4 mm
Rounded Corners
25.4 mm
A
A
Cross Section Detail A-A
1.98 mm
Green: Embedded Longitudinal CF Layer
Blue: Embedded Lateral CF Layer
Black: Non-embedded Layer (added during layup with epoxy)

Figure 3.1: Schematic of the three embedded CF layer hybrid transition structure design with straight channels.

Of the three consolidated CF layers, the top and bottom layer CF tows are orientated parallel to the weld direction while the middle layer tows is orientated perpendicular to the weld direction. Each layer of embedded CF are housed in five channels with each channel housing two CF tows. This results in a total of ten CF tows being embedded within each layer. Figure 3.2 shows the embedding sequence for each layer of embedded CF tows.

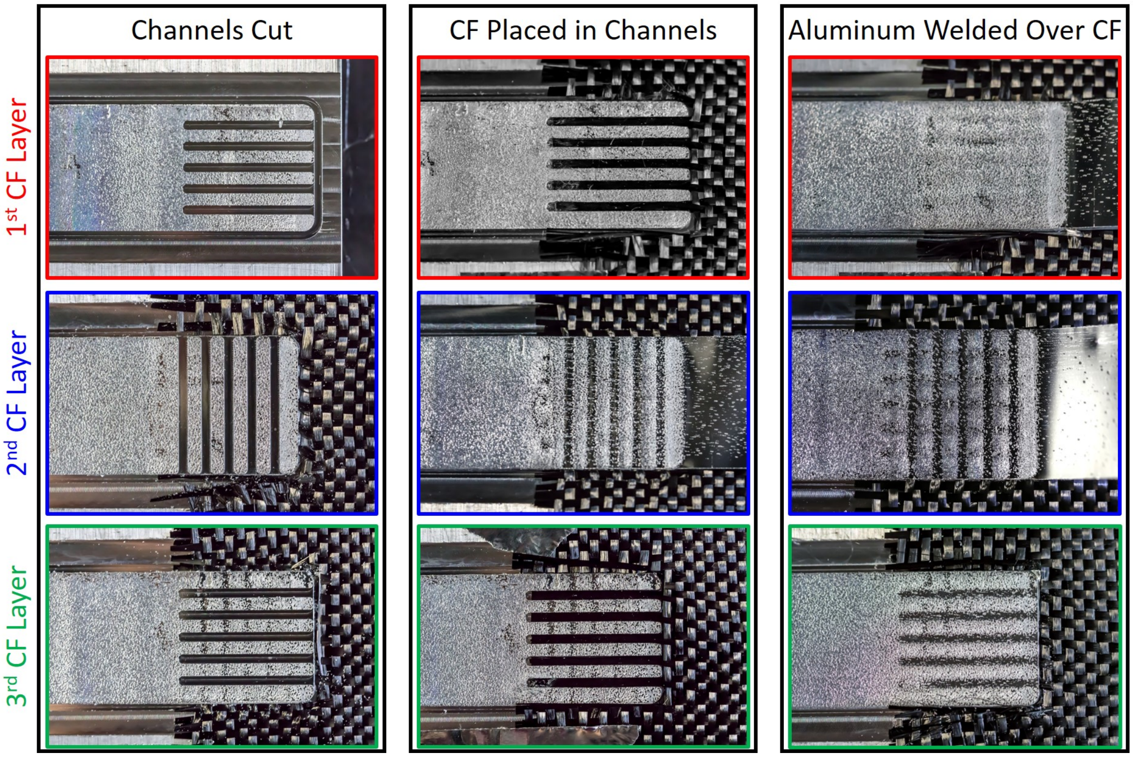
Channels Cut
CF Placed in Channels
Aluminum Welded Over CF
1st CF Layer
2nd CF Layer
3rd CF Layer

Figure 3.2: Carbon fiber embedding sequence in the three layer, straight channel CF-Al joint design.

The UAM CF-Al joints were welded onto a small, 100 mm x 75 mm x 8 mm 6061-T6 aluminum baseplate. Before any of the metal foil was welded, the baseplate was textured by running the vibrating sonotrode over the plate, but depositing no welding foil. This texturing is important because it greatly increases the bond strength between the baseplate and the first layer of welded foil. The weld parameters used for creating the joint are shown in Table 3.1. Note that the welding amplitude was reduced slightly when welding directly over the CF layers. this was done to reduce chances of the foil tearing which has been an ongoing problem occurring when welding over channels. Foil tearing is discussed in detail in Chapter 5. The stacking sequence sequence used for the three layer, straight channel joints is shown in Table 3.2. The channel widths and depths used were 1.78 mm x 0.25 mm respectively.

Table 3.1: UAM parameters used during three layer, straight channel joint construction.

Welding Force	4500 N
Welding Speed	508 cm/min
Amplitude	32μm (31μm over channels)
Heat-plate Temperature	Room Temperature (22 C°)
Spot Dwell	250 ms

Table 3.2: Three layer, straight channel HTS stacking sequence.

Description	**Cumulative Thickness**
Thickness of baseplate left on specimen	0.15 mm
First two foil layers are welded	0.46 mm
Layer 1 channels cut and CF tows inserted	0.46 mm
Four foil layers are welded over CF layer 1	1.07 mm
Layer 2 channels cut and CF tows inserted	1.07 mm
Four foil layers are welded over CF layer 2	1.68 mm
Layer 3 channels cut and CF tows inserted	1.68 mm
Two foil layers are welded over CF layer 3	1.98 mm

Once the three layers of CF were consolidated, the aluminum tab was removed from the small aluminum baseplate. This was accomplished by conventional milling operations. Once the structure had been removed from the baseplate, it was integrated with additional layers of bidirectionally woven CF fabric, shown in the lower portion of Figure 3.1. This integration process was completed by hand layup methods with Fibre Glast System 2000 epoxy resin, using the Fibre Glast 2120 hardener. The CF-Al joint before and after layup is shown in Figure 3.3. The case in Figure 3.3 shows a tensile specimen, but this same layup technique was used for the three-point-bend specimens as well.

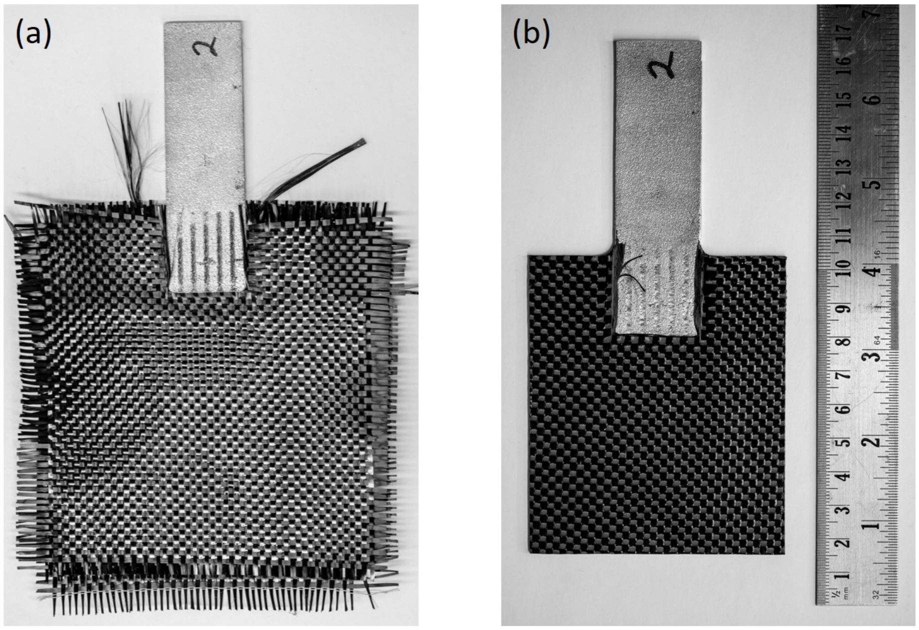

Figure 3.3: (a) Three layer, straight channel CF-Al joint after baseplate removal, (b) Tensile specimen formed after layup with additional CF bidirectional fabric layers and epoxy.

3.1.2 Corrosion Testing

Due to high susceptibility to galvanic corrosion, one of the CF-Al joints described in Section 3.1.1 was placed in a corrosive environment to qualitatively examine how UAM CF-Al joints may perform in a corrosive environment. In addition to CF-Al joints discussed in Section 3.1.1, a similar specimen featuring embedded glass fibers integrated into additional bidirectional CF fabric layers was constructed and put through the same corrosive testing as the CF-Al joint for comparison sake. The significance of a CF-GF-Al joint is that there is no electrical couple between the CF and aluminum since they are separated by non-conductive glass fibers and epoxy.

Carbon/Glass/Aluminum Joint Construction

Consolidating glass fibers from glass fabric was accomplished in a similar manner to what was described in Section 3.1.1. As before with the CF-Al joint, three layers of glass fabric tows were embedded: on the top and bottom layers the glass fiber tows were oriented parallel to the weld direction, on the middle layer the tows were oriented transverse to the weld direction. Figure 3.4 shows the middle layer after it had been embedded.

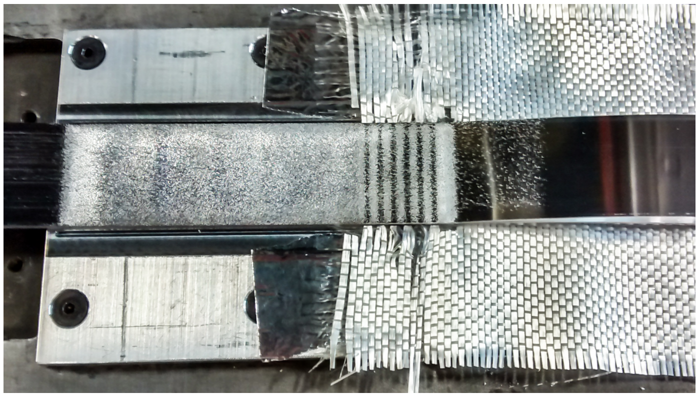

Figure 3.4: Glass fabric being consolidated into 6061-H18 aluminum.

The fiberglass used was Rutan glass unidirectional fabric which was purchased from Aircraft Spruce Specialty Co. The spacing of the fiber tows in this fabric was finer than the bidirectional CF fabric used in Section 3.1.1, so the number of channels going through the aluminum tab for each fabric layer was increased from five to six, as seen in Figure 3.4. The channel width and depth used for the glass consolidation was 1.6 mm x 0.32 mm respectively. The weld parameters used were the same as those used for the three layer, straight channel CF-Al joints (Table 3.1). The stacking sequence was also identical to that described in Section 3.1.1 (Table 3.2).

Once the three glass fabric layers were consolidated within the 6061-H18 aluminum tab, the glass layers were laid up with four CF bidirectional fabric layers to form the CF-GF-Al structure shown in Figure 3.5. Clearance space was cut out of the CF fabrics to prevent the CF from touching the aluminum tab and creating a galvanic couple. Several glass tows were placed between the CF fabrics and the aluminum tab during the layup process.

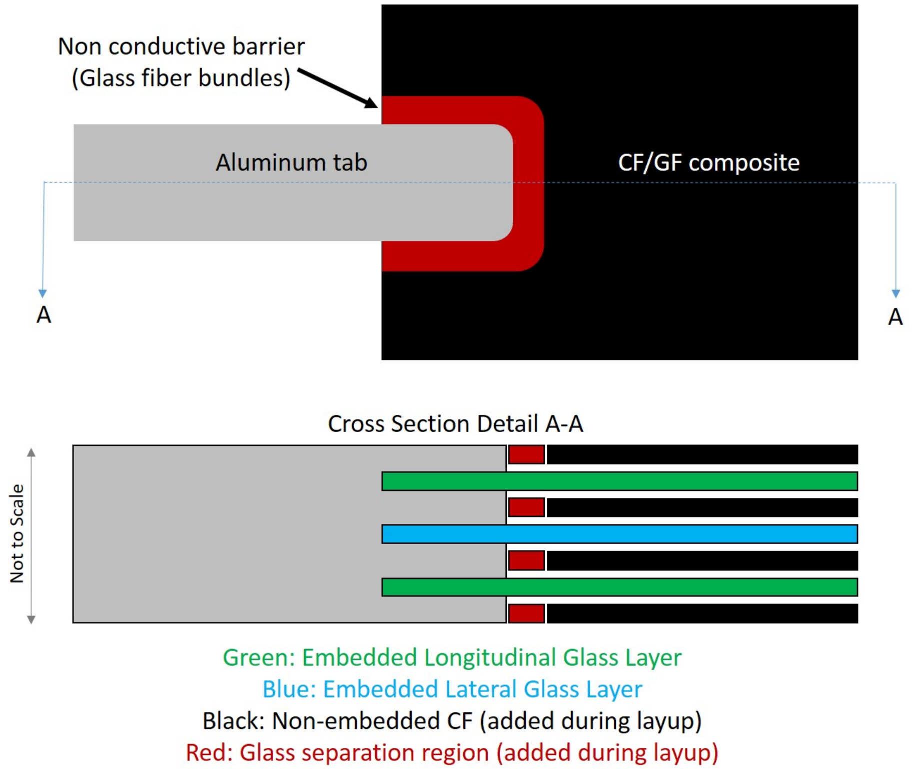
Non conductive barrier
(Glass fiber bundles)
Aluminum tab
CF/GF composite
A
A
Cross Section Detail A-A
Not to Scale
Green: Embedded Longitudinal Glass Layer
Blue: Embedded Lateral Glass Layer
Black: Non-embedded CF (added during layup)
Red: Glass separation region (added during layup)

Figure 3.5: Schematic portraying CF-GF-Al hybrid joint design.

Specimen Preparation for Corrosive Testing

Once CF-Al and CF-GF-Al joints were created and laid up with epoxy into their final structures, electrical resistance measurements were made to comparatively evaluate the current path between CF and aluminum components for both structures. The method used was simply connecting one of the ohm-meter's terminals to the aluminum tab and connecting the other terminal to the cut end of the CFRP. The CF-Al joint yielded a resistance of 50-300 ohms which fluctuated depending on the location of the CF terminal connection. The CF-GF-Al joint yielded a greater resistance at 3000 ohms. The CF-GF-Al resistance not being infinite suggests that there was still a slight current path, though the path was more restrictive than the CF-Al joint current path.

After the joints were tested for current path resistance, they were coated with a layer of epoxy to protect them from the corrosive environment. Literature suggests that the thickness of protective coating over a CF-Al joint effects galvanic corrosion greatly [32]. This is because a comprehensive coating prevents the electrolyte surrounding the specimen from reacting with the anode and cathode. The thickness of the epoxy coating was not measured, but each piece was visually inspected to make sure that no uncoated regions were present.

Corrosion Cycling Procedure and Visual Results

The corrosion cycling used featured swings in humidity, temperature, and periods of salt spray solution. This type of corrosive environment is more severe than conventional salt spray testing and therefore accelerates the corrosion process further. The two joints, CF-Al and GF-CF-Al, were placed in this environment for 20 days. Each period of 10 days of the corrosion cycling corresponds to roughly one year of corrosion in actual part use. The specimens were removed from the testing periodically throughout the 20 days of testing for imaging and progress analysis.

By the end of the 20 day corrosion cycling period, there were very few visible signs of corrosion on either specimen. One observation was a slight crazing on the surface of the epoxy coating, this was seen in both specimens. Figure 3.6 shows images of the CF-Al and CF-GF-Al joints before the corrosion cycling and after the full 20 days of testing. The only defect found after the corrosion cycling was a small region where the epoxy cracked and began to lift from the CF-Al joint. However, this defect may have been caused by epoxy weathering rather than galvanic corrosion (Figure 3.7).

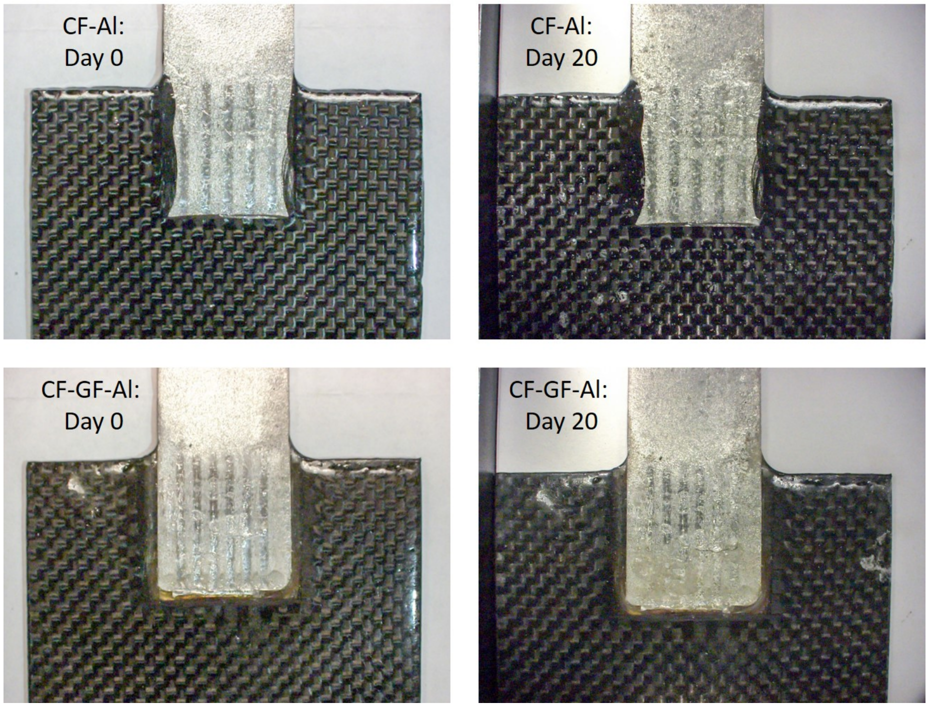

Figure 3.6: Specimen visual appearance before and after the corrosion cycling for CF-Al and CF-GF-Al joints.

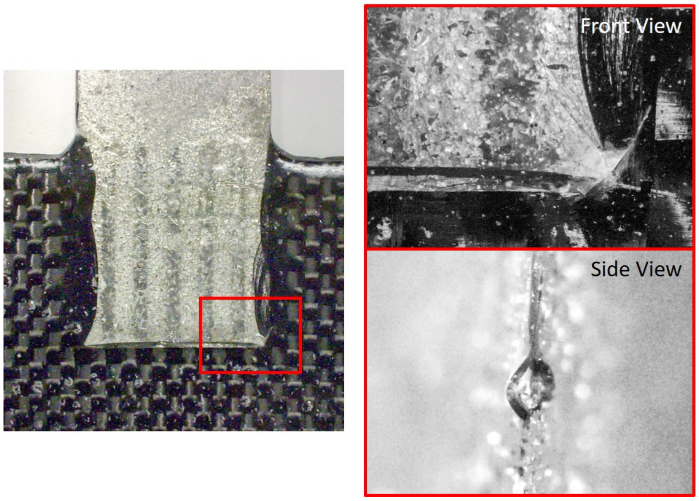

Figure 3.7: Epoxy cracking observed in corroded CF-Al joint.

Though scarcely any visible corrosion was seen on the specimens after 20 days of corrosion cycling (two year equivalent), it is possible that galvanic corrosion was at work deep within the joints. To better understand if this was the case, tensile testing was performed later on the corroded specimens. This is described in Section 3.1.3.

3.1.3 Tensile Testing

Mechanical tensile testing was completed on the corroded CF-Al and CF-GF-Al joints. Two non-corroded specimens of each type were also tested for comparison. The testing was designed in this manner to see if the the corrosion cycling caused a noticeable reduction in joint strength. The testing was completed on a Interlocken load frame powered by a MTS hydraulic system, used in conjunction with MTS grips. The testing was was controlled by a National Instruments LabVIEW VI which sends a ramp voltage input to the MTS hydraulic system controller through a National Instruments DAQ interface. During the testing, load and displacement/strain measurements were recorded through the load frame load cell and digial image correlation (DIC) system respectively. This setup is pictured in Figure 3.8.

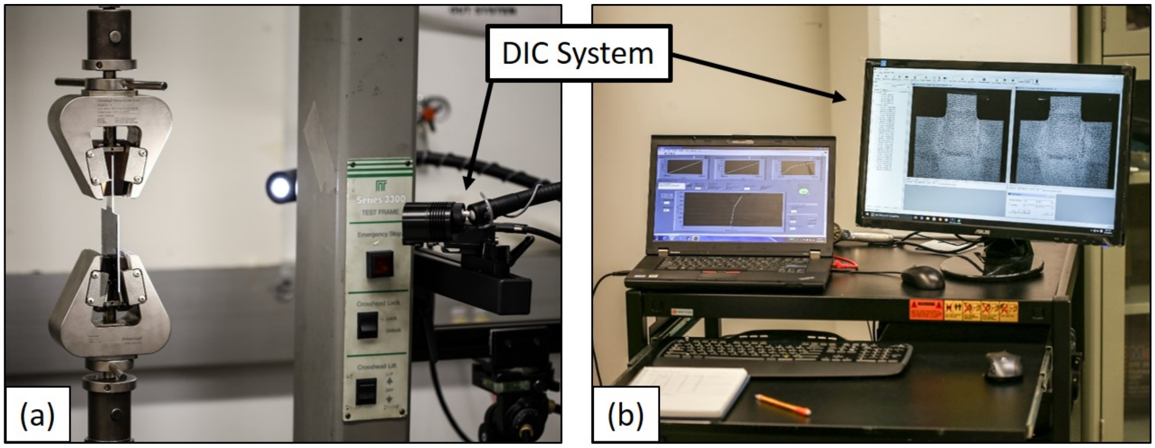

Figure 3.8: Tensile testing equipment: (a) Interlocken frame, MTS grips, and DIC camera setup. (b) Control and data aquisition center.

Digital image correlation (DIC) is a displacement and strain measurement tool which uses hundreds of images taken throughout a test to complete strain analysis over a region of interest. The DIC system consists of two cameras which view the test area from two different locations. Calibration images are taken and processed to insure accurate spacial information of each camera location and the angle between the cameras. Once proper calibration is achieved, the tensile test is run with the cameras taking images throughout the test at a user defined rate. The test piece has been painted white and speckled with black dots in a random pattern so that the cameras can track movement of each point on the specimen. Later in post processing the analysis tool tracks the deformation of the workpiece. The analysis tool can provide strain and displacement data from any two points on the test piece that have been included in the area of interest. DIC has been used throughout this research work wherever possible, providing an accurate and versatile source of strain and displacement measurements. Strain field plots for the corroded CF-Al and CF-GF-Al joints just before failure are shown in Figure 3.9.

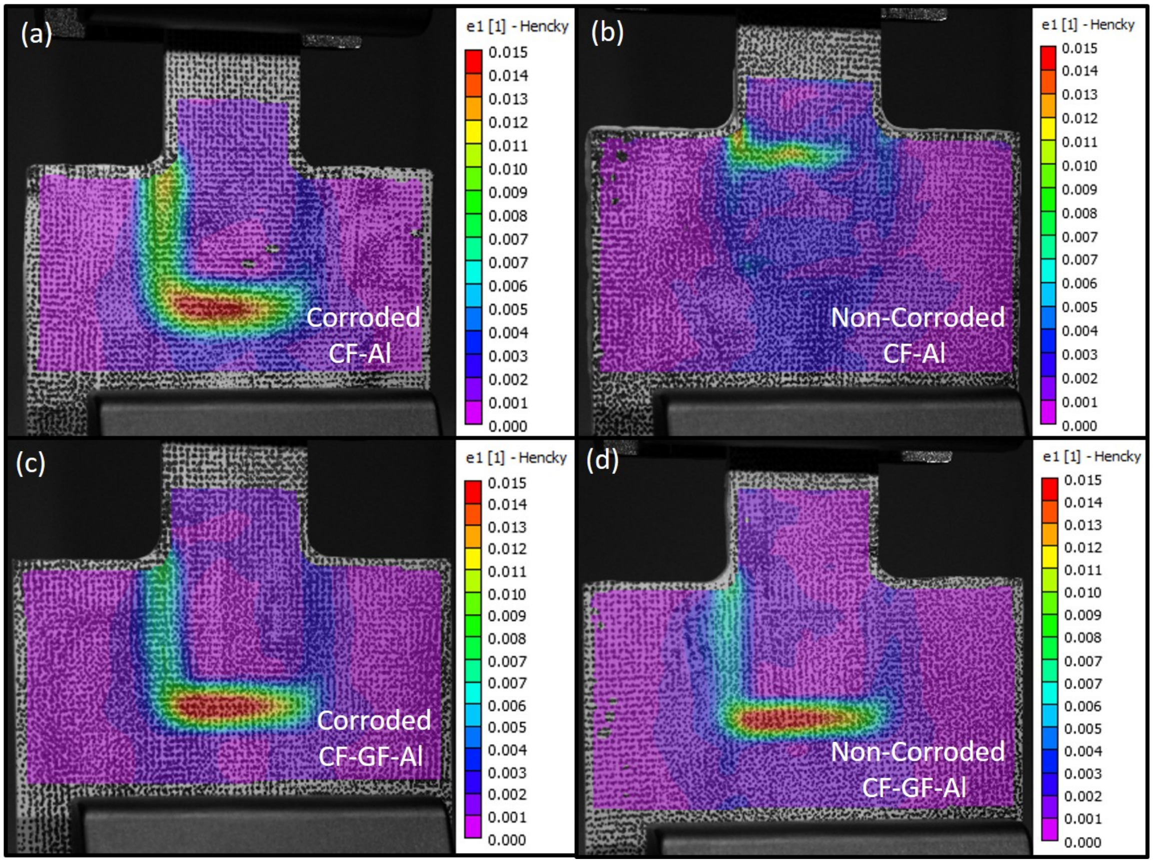

Figure 3.9: DIC strain maps of failure initiation overlaid onto tensile specimens. (a) Corroded CF-Al tensile specimen. (b) Non-corroded CF-Al tensile specimen. (c) Corroded CF-GF-Al tensile specimen. (d) Non-corroded CF-GF-Al tensile specimen.

The results from the tensile testing showed that specimens subjected to corrosion cycling did not have significantly lower strength. Both CF-Al specimens performed better than either of the CF-GF-Al specimens. This was expected since the glass fiber pullout strength is lower than the CF pullout strength as discussed in Section 2.4.2. Load vs. displacement for each of the specimens is plotted in Figure 3.10.

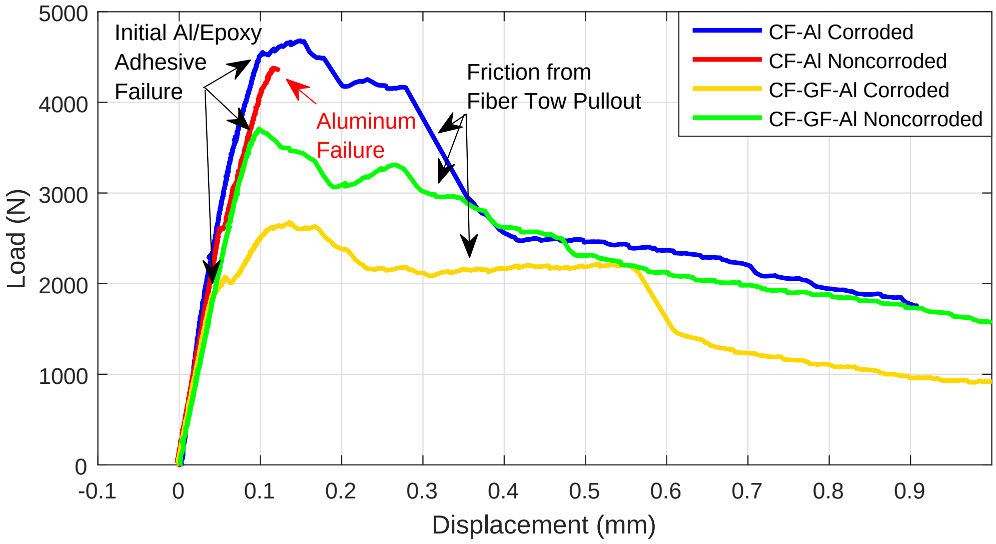

Figure 3.10: Load vs. displacement for each of the four three embedded layer tensile specimens.

The failure mode present in the corroded CF-Al joint and both of the CF-GF-Al joints was adhesive failure at the epoxy/aluminum interface followed by pullout of the longitudinally embedded fibers and shearing of the middle layer of laterally embedded fiber tows. However, the non-corroded CF-Al joint failed within the aluminum tab at the uppermost transversely oriented embedded CF layer. The aluminum cracking initiation can easily be seen in Figure 3.9(b). Failure within the aluminum tab was unexpected, but the failure probably occurred in that region because of an unobserved manufacturing defect such as a minor case of foil tearing. This paired with the aluminum material being near its yield strength resulted in failure outside of the expected failure region. Examples of the two modes of failure are shown in Figure 3.11.

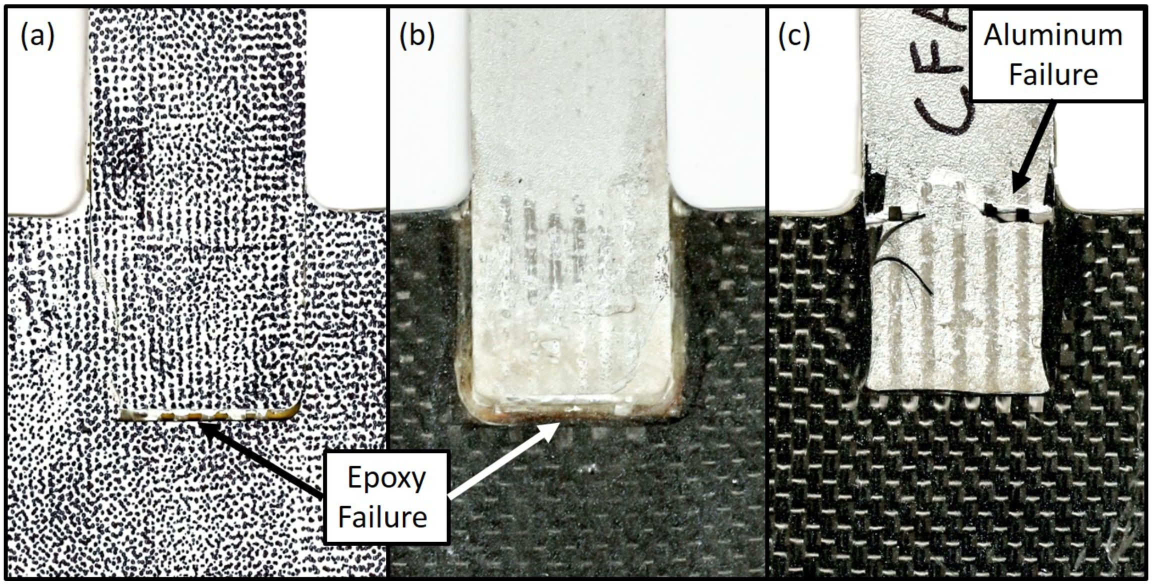

Figure 3.11: Failed specimens from tensile testing: (a) Adhesive failure in the non-corroded CF-GF-Al specimen (surface is covered with DIC speckling). (b) Adhesive failure in the corroded CF-GF-Al specimen. (c) Aluminum failure in the non-corroded CF-Al specimen.

In summary, tensile testing of the CF-Al and CF-Al-GF joints provided the following results and insight into future joint design work:

1. The three-layer, straight channel CF-Al joints reached a maximum load of 4500 N before damage occurred. The strongest of the CF-GF-Al joints reached a load of 3600 N before damage occurred.

2. The specimens subjected to corrosion cycling did not consistently perform worse than the non-corroded specimens. Future corrosion testing may need to be more severe to be able to observe a significant drop in joint performance.

3. CF-GF-Al joints have inferior performance when compared with the CF-Al joints. This is mainly due to poor pullout strength of the glass fiber tows.

3.1.4 Three-Point-Bend Testing with Adhesive Joint Comparison

Another loading condition which is of concern in CFRP to metal joints is bending. Adhesive joints are not particularly well suited for bending loads, so a three-point-bend study was conducted to compare the joint strength of the three-layer CF-Al joint described in Section 3.2 with a similarly designed adhesive joint. The three-point-bend loading configuration was chosen over four-point-bending due to the availability of necessary fixturing. Four-point-bending is often regarded as superior to three-point-bending since it provides constant bending over the specimen. However, for the chosen joint and fixturing geometry uneven bending moments were adequate due to the symmetry of the specimens and location of the joint region.

UAM Three-Point-Bend Joint Design

The three-point-bend joint design was very similar to the three-layer, straight channel CF-Al tensile specimen design. The only difference was in the composite layup process. The three-point-bend UAM specimen included two identical CF-Al joints which had their embedded CF layers integrated with each other as shown in Figure 3.12. To integrate the CF fabrics together, rectangular portions of the CF fabric were removed so that the free side of each CF fabric layer fit around the opposing CF-Al joint's aluminum tab, shown in Figure 3.13(a). The two halves of the three-point-bend specimen were integrated together using hand layup techniques and Fibre Glast 2000 system epoxy. The completed specimen is shown in Figure 3.13(b).

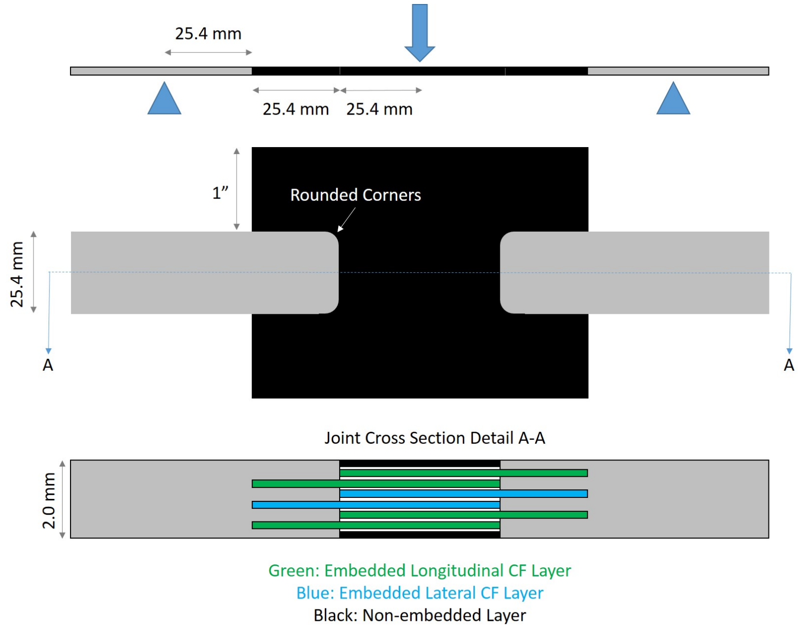
25.4 mm
25.4 mm
25.4 mm
1"
Rounded Corners
25.4 mm
A
A
Joint Cross Section Detail A-A
2.0 mm
Green: Embedded Longitudinal CF Layer
Blue: Embedded Lateral CF Layer
Black: Non-embedded Layer

Figure 3.12: Schematic showing the three-point-bend specimen design featuring three-layer CF-Al UAM joints.

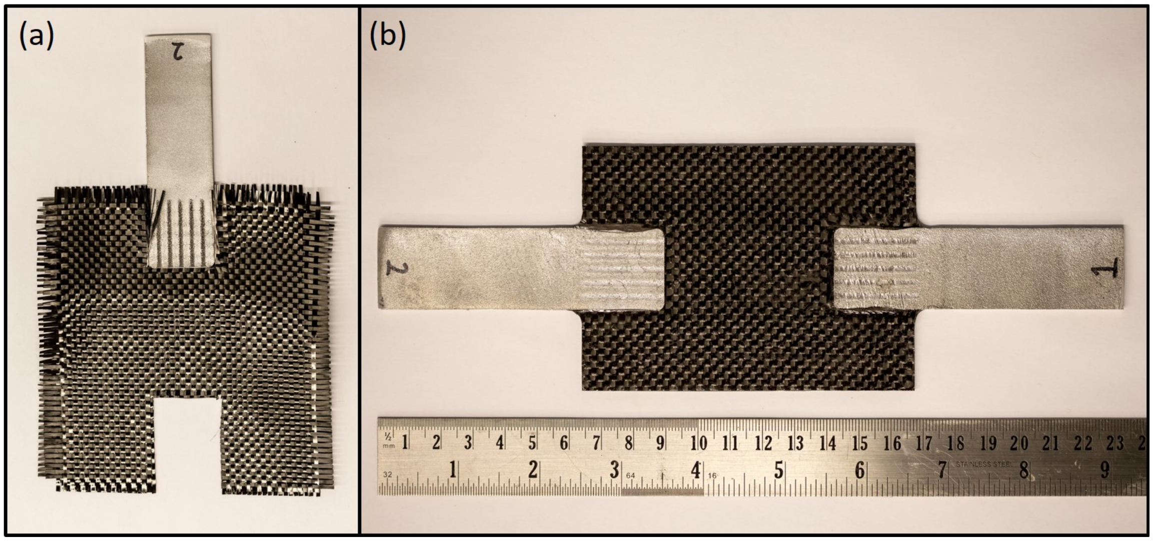

Figure 3.13: (a) CF-Al joint before layup into the three-point-bend structure. (b) Completed UAM CF-Al three-point-bend specimen.

Single Lap Adhesive Three-Point-Bend Specimen Construction

The components used to create the adhesive three-point-bend specimen include two aluminum tabs and a CFRP plate. The two aluminum tabs were made of UAM 6061-H18 material and were sized to match the three-point-bend specimen's aluminum tabs. The final thickness of the tabs was 2.0 mm. The CFRP plate was an eight-ply bidirectional CF laminate created by hand layup techniques and Fibre Glast System 2000 epoxy. The total thickness of the CFRP plate was 1.8 mm.

Prior to joining, the CFRP and aluminum surfaces were treated per ASTM standards D2093 and D2651 respectively [1] [2]. The CFRP surface treatment included an acetone wash, rinse, texturing (fine-girt sanding), a second acetone wash, and a second rinse. The aluminum surface treatment included a degreasing acetone wash, rinse light sanding, rinse, etching using 10% NaOH for two minutes, and a final rinse. The joining components with their respective surface treatments are shown in Figure

3.14(a). After the surface treatments were completed, the aluminum tabs and CFRP plate were joined with the Fibre Glast System 2000 epoxy. The epoxy was brushed onto all the joining surfaces. The components were then clamped into position as shown in Figure 3.14(b). A flat steel plate was clamped together with the CFRP and aluminum components to insure even clamping pressure throughout the joints.

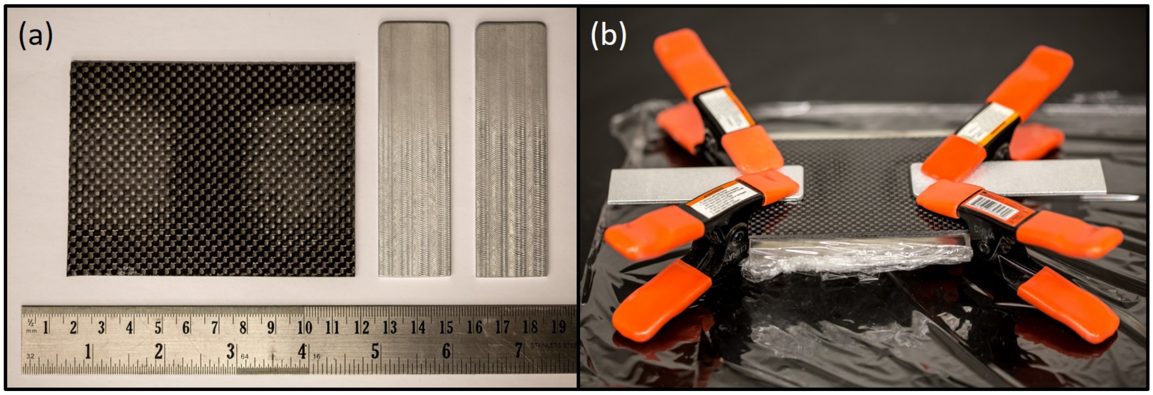

Figure 3.14: (a) Adhesive three-point-bend components, complete with treated joining surfaces. (b) Clamping the three-point-bend adhesive components together.

Three-Point-Bend Testing Procedure

The three-point-bend testing was completed for both UAM and adhesive joint specimens using the same load frame described in Section 3.1.3. NI LabVIEW was used to control the test and record load and stroke during the test (DIC was not used). The loading rate of the test was 22 mm/min. This loading rate was determined based off of the spread between the bend fixture supports (15.24 cm) and the thickness of the specimen (1.8 mm in the CF region). Figure 3.15 shows the three-point-bend fixture set up for the test. High definition motion captures of each test were recorded in addition to load and stroke data.

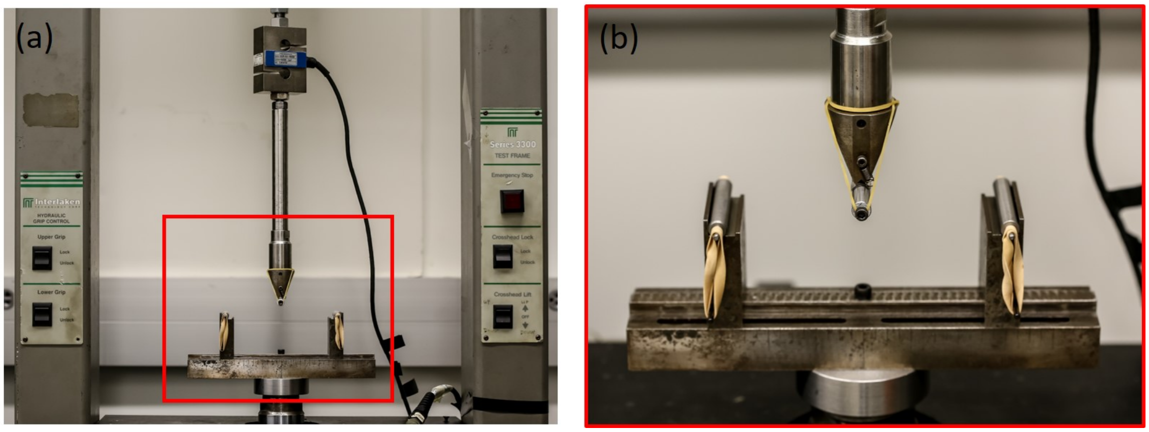

Figure 3.15: (a) Interlocken load frame set up with the three-point-bend fixture. (b) Three-point-bend fixture detail.

Three-Point-Bend Results and Comparison

Results from the three-point-bend tests showed that the UAM CF-Al joint had greater strength and energy dissipation than the adhesive single lap joint. This is illustrated by the load vs. displacement plot in Figure 3.16. The stiffness of the adhesive specimen was greater than that of the UAM CF-Al specimen as would be expected. This was due to the added material in the joint region of the adhesive specimen. The adhesive joint experienced catastrophic failure at a load of 255 N. Elements of adhesive (70%) and light-fiber-tear (30%) failures were observed in the adhesive joint specimen according to ASTM D5573 [3]. The amount of light-fiber-tear present suggests that the component surface preparation was adequate, though a greater percentage of light-fiber-tear failure would be desirable. The failed components of the adhesive joint specimen are shown in Figure 3.17.

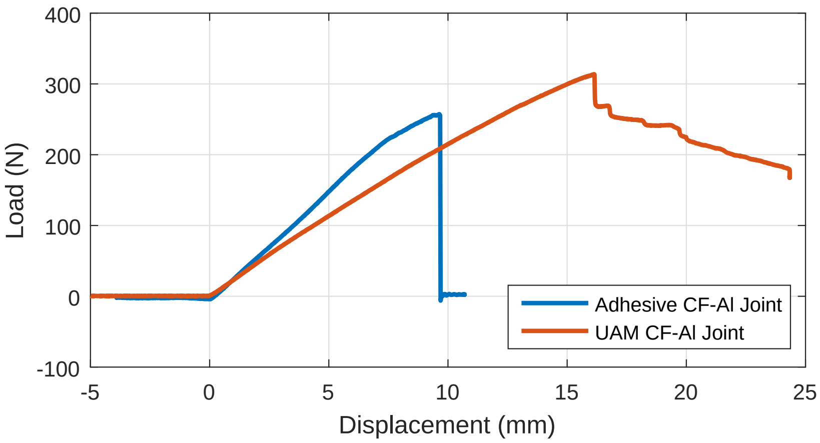

Figure 3.16: Load vs. displacement for UAM CF-Al and Adhesive CF-Al joints.

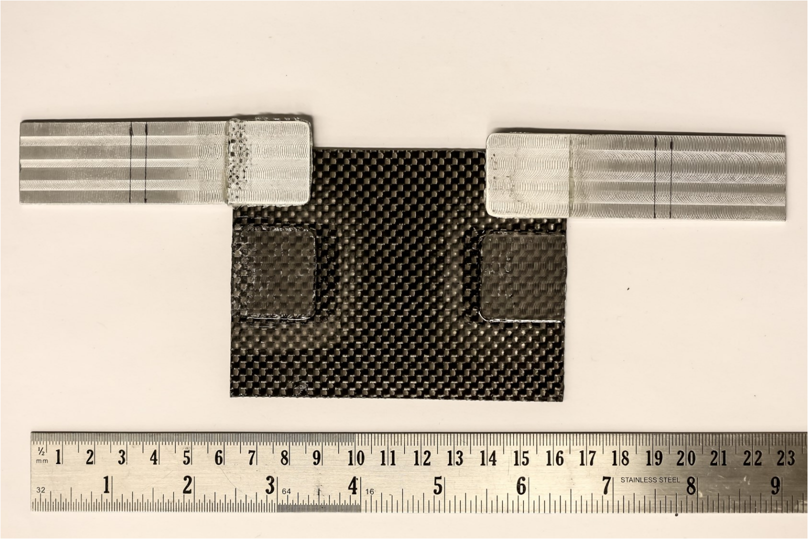

Figure 3.17: Components of the failed adhesive single lap three-point-bend speicmen.

Cracking along the inside corner interface between the CFRP and aluminum tab began in the UAM CF-Al specimen at a load of 320 N. As the displacement increased, the crack progressed, shearing off some of the transversely embedded CF. In addition to the sheared CF, the welded aluminum partially delaminated in the location of the laterally embedded CF. However, catastrophic failure did not occur. When the test was stopped, the UAM specimen was still carrying 180 N and the longitudinally embedded CF remained in-tact. After the cracking in one of the UAM joints, the specimen deformed asymmetrically for the remainder of the test, thereby reducing stress in the non-damaged joint. This resulted in only one of the joints being damaged at the end of the test. Images of the damaged UAM joint are shown in Figure 3.18.

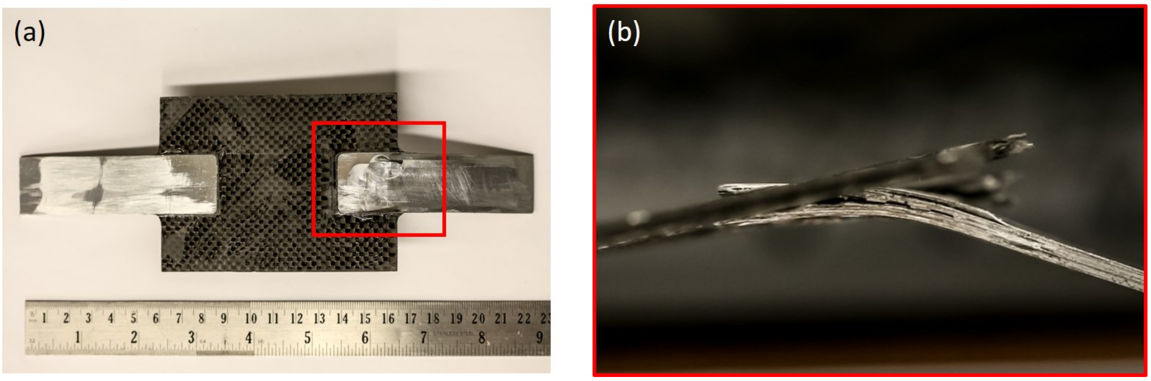

Figure 3.18: (a) Damaged UAM CF-Al joint. (b) Detail of UAM CF-Al joint damage.

3.1.5 Discussion

In summary, the UAM CF-Al joint design featuring three layers of consolidated CF tows was successfully used to manufacture tensile and three-point-bend specimens. A similar design was also used to create CF-GF-Al tensile joints by embedding glass fibers and integrating with additional CF fabric layers. Results from corrosion cycling on the CF-Al and CF-GF-Al tensile specimens suggested harsher corrosion cycling is needed before the effects of galvanic corrosion significantly affect joint performance.

Tensile testing results provided a number to place on the UAM CF-Al joint strength, with a maximum load of 4600 N. The three-point-bend testing showed that the UAM CF-Al joint had superior bending performance when compared to adhesive single lap joining in both strength and energy dissipation.

3.2 Five Layer, Straight Channel Joints

With the success of UAM CF-Al joints with three layers of embedded CF, investigation of thicker joint designs with five layers of embedded CF was pursued. From a theoretical standpoint, the strength of UAM CF-Al joints should scale proportionally to the thickness and number of embedded CF tows. The purpose of the thicker five-layer specimens was to obtain joints with a greater load capacity.

3.2.1 Joint Design and Manufacturing

The joint design of five layer CF-Al joints was similar to that described in Section 3.1.1, but with a few distinct differences. The first is that this design features five layers of embedded CF tow layers. The five layers can be broken down in to three layers of embedded tows oriented parallel to the weld direction and two layers of tows oriented at an angle roughly perpendicular to the weld direction. Figure 3.19 presents the building sequence of the embedded layers.

As can be seen in Figure 3.19, the transverse channels were no longer oriented exactly perpendicular to the welding direction. These channels were set at slight angle to create a even substrate stiffness as experienced by the sonotrode during welding. This modification was made in an attempt to reduce foil tearing when welding over the transversely oriented channels. However, intermittent foil tearing persisted and it was determined that no benefits were gained from the angled channels.

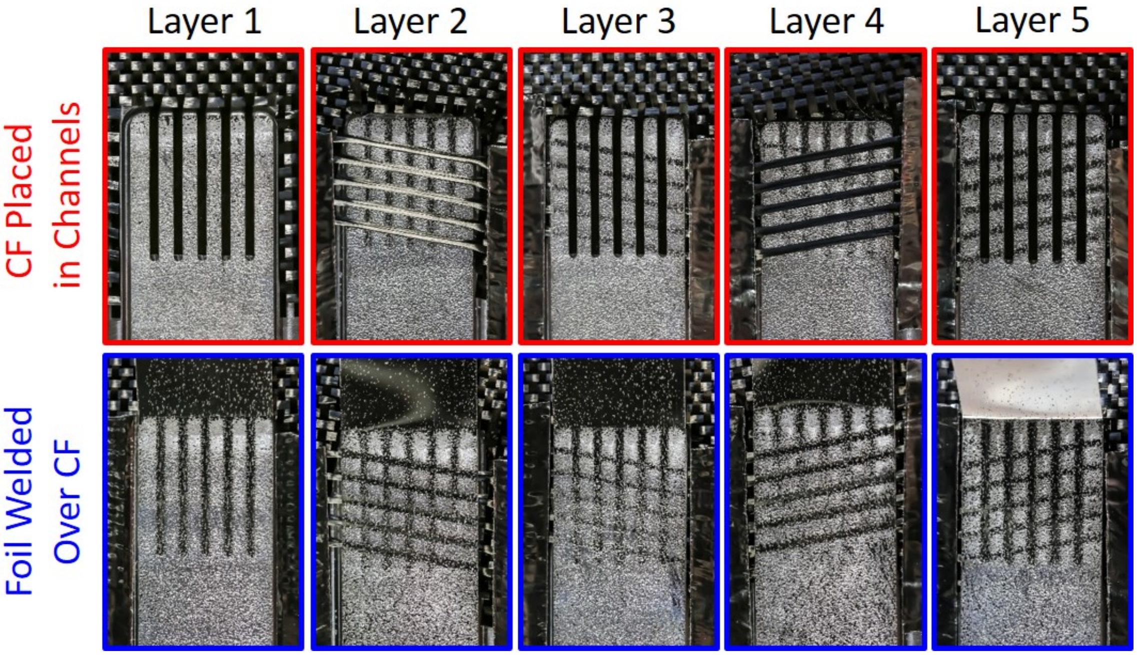
Layer 1
Layer 2
Layer 3
Layer 4
Layer 5
CF Placed in Channels
Foil Welded Over CF

Figure 3.19: Embedding sequence for the five layer CF-Al joint manufacturing process.

The channel dimensions used for embedding the HexTow AS4C 4000 3K tows were 1.59 mm x 0.28 mm in width and depth respectively. The weld parameters used throughout the five embedded layer CF-Al joint manufacturing process are shown in Table 3.3. The stacking sequence used for the five embedded layer joints is shown in Table 3.4. After the welding process was completed and the joints were removed from the aluminum baseplates, the CF layers were integrated with additional bidirectional CF layers and epoxy to form the finished specimens.

Table 3.3: UAM parameters used for five layer CF-Al joints.

Welding Force	4500 N (2500 N over channels)
Welding Speed	508 cm/min
Amplitude	32.3 μm
Heat-plate Temperature	Room Temperature (22 C°)
Spot Dwell	250 ms
Sonotrode Roughness	14 μm

Table 3.4: Five layer CF-Al joint stacking sequence.

Description	**Cumulative Thickness**
Thickness of baseplate left on specimen	0.15 mm
First two foil layers are welded	0.46 mm
Layer 1 channels cut and CF tows inserted	0.46 mm
Three foil layers are welded over CF layer 1	0.91 mm
Layer 2 channels cut and CF tows inserted	0.91 mm
Three foil layers are welded over CF layer 2	1.37 mm
Layer 3 channels cut and CF tows inserted	1.37 mm
Three foil layers are welded over CF layer 3	1.83 mm
Layer 4 channels cut and CF tows inserted	1.83 mm
Three foil layers are welded over CF layer 4	2.29 mm
Layer 5 channels cut and CF tows inserted	2.29 mm
Two foil layers are welded over CF layer 5	2.59 mm

3.2.2 Tensile Testing Results

Tensile testing was performed on one of the five embedded layer CF-Al joints. As would be expected, the load carrying capacity increased substantially compared to the three embedded layer CF-Al joints. Figure 3.20 shows a load vs. displacement curve comparison between the five layer joint and the highest performing three layer joint from Section 3.1.3.

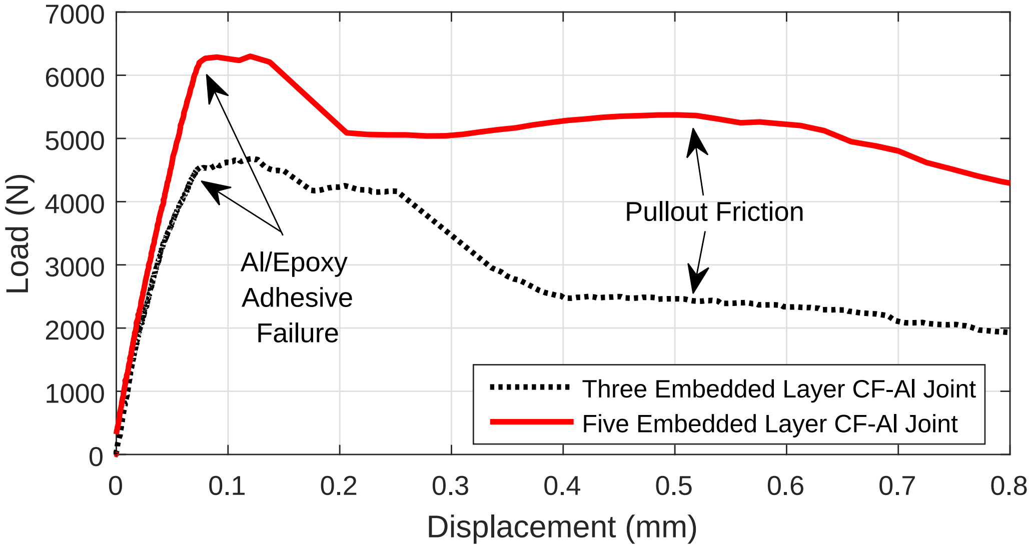

Figure 3.20: Tensile results from the five layer CF-Al tensile test compared with three embedded layer CF-Al joint performance.

The mode of failure for the the five layer joint was the same as most of the three layer joints: fracture of the aluminum/epoxy interface around the perimeter of the joint, followed by pullout of the longitudinally embedded CF tows. The transversely embedded CF tows failed in a combined shear/tensile loading. One difference in the initial failure with the five layer joint was that the aluminum/epoxy interface cracking began at the end of the aluminum tab instead of at one of the inside corners between the CFRP and aluminum tab. This can be easily seen from a processed DIC strain map animation. Two of the animations frames are shown in Figure 3.21. These show strain maps overlaid on the five layer specimen immediately before and after the initial cracking at the end of the aluminum tab. Images of the failed five layer joint are shown in Figure 3.22.

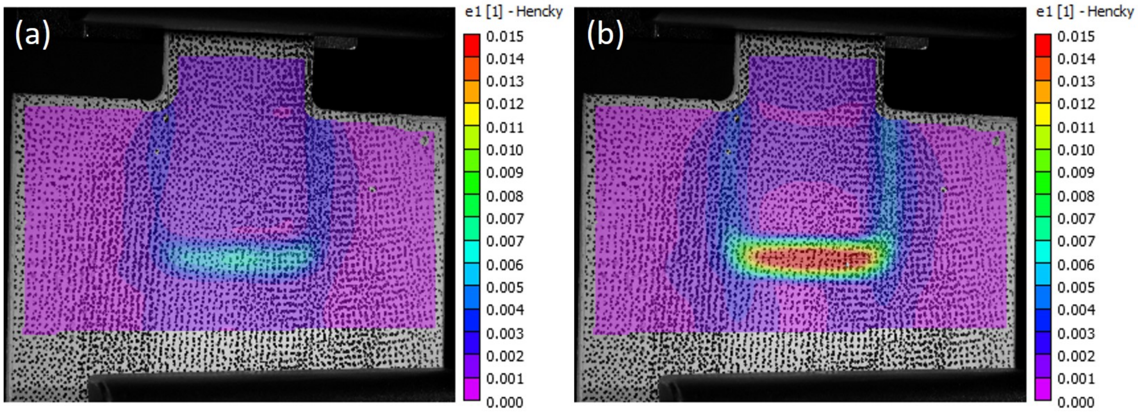

Figure 3.21: Strain mapping overlaid on the five embedded CF-Al specimen. (a) Immediately before initial cracking at the base of the aluminum tab. (b) Immediately after initial cracking at the base of the aluminum tab.

The five layer tensile specimen had a slightly different channel design than the other five layer specimens. From Figure 3.22 it can be seen that the longitudinally embedded CF tows and the channels that house them are not of even length. For the particular joint that was tested, this channel length staggering was incorporated to reduce the severity of end of channel stress concentrations and cross sectional area reduction. Shortening the length of these longitudinal channels has little effect on the pullout strength of the CF tows being housed since the largest stresses occur within two CF tow diameters from the front edge of the joint [22]. Additionally, the epoxy used is only able to impregnate the CF tows up to about 7 mm deep into the aluminum structure. This implies that the additional length of embedded CF carries little load until failure occurs and pullout friction becomes the main load-bearing component.

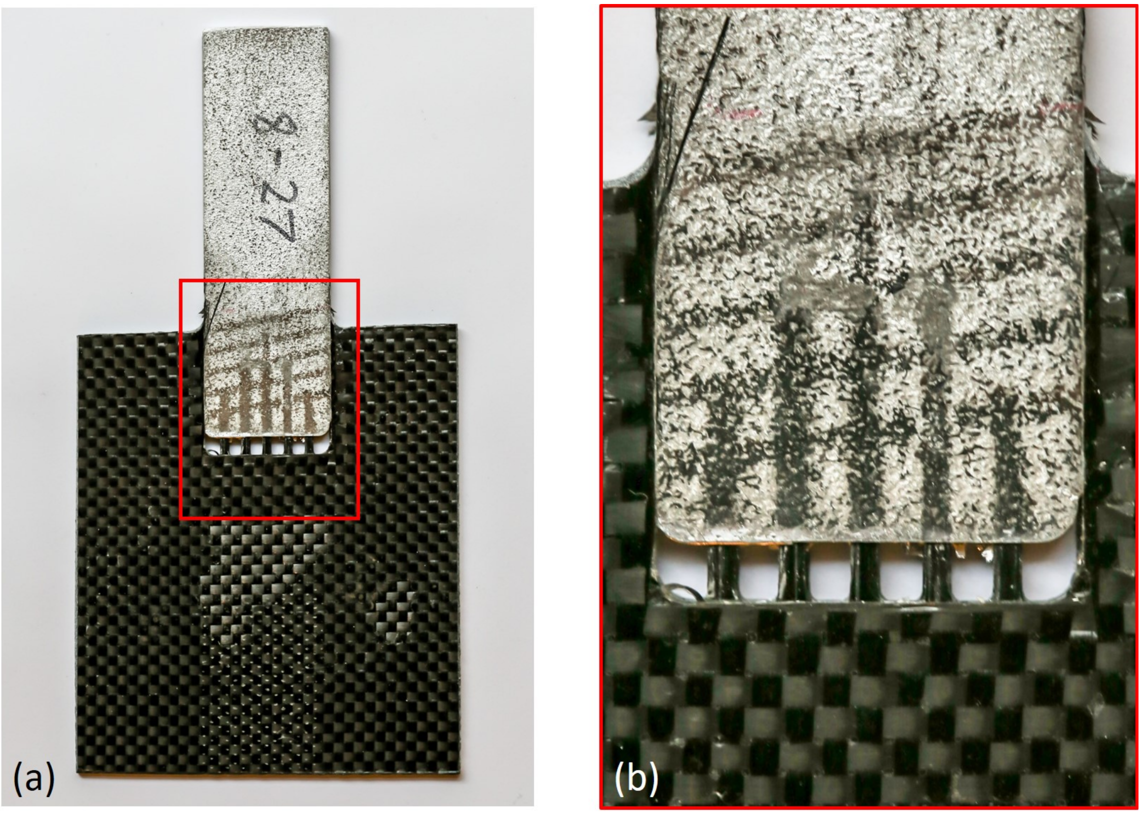

Figure 3.22: (a) The five embedded layer CF-Al joint after tensile testing. (b) Failed joint detail.

3.2.3 Three-Point-Bend Testing and Results

In addition to tensile testing, three-point-bend testing was completed with the five layer CF-Al joint design. The three-point bend specimen was created in the same manner as the three layer design discussed in Section 3.1.4. The two CF-Al joints were integrated together by overlapping the CF fabrics as shown in Figure 3.23.

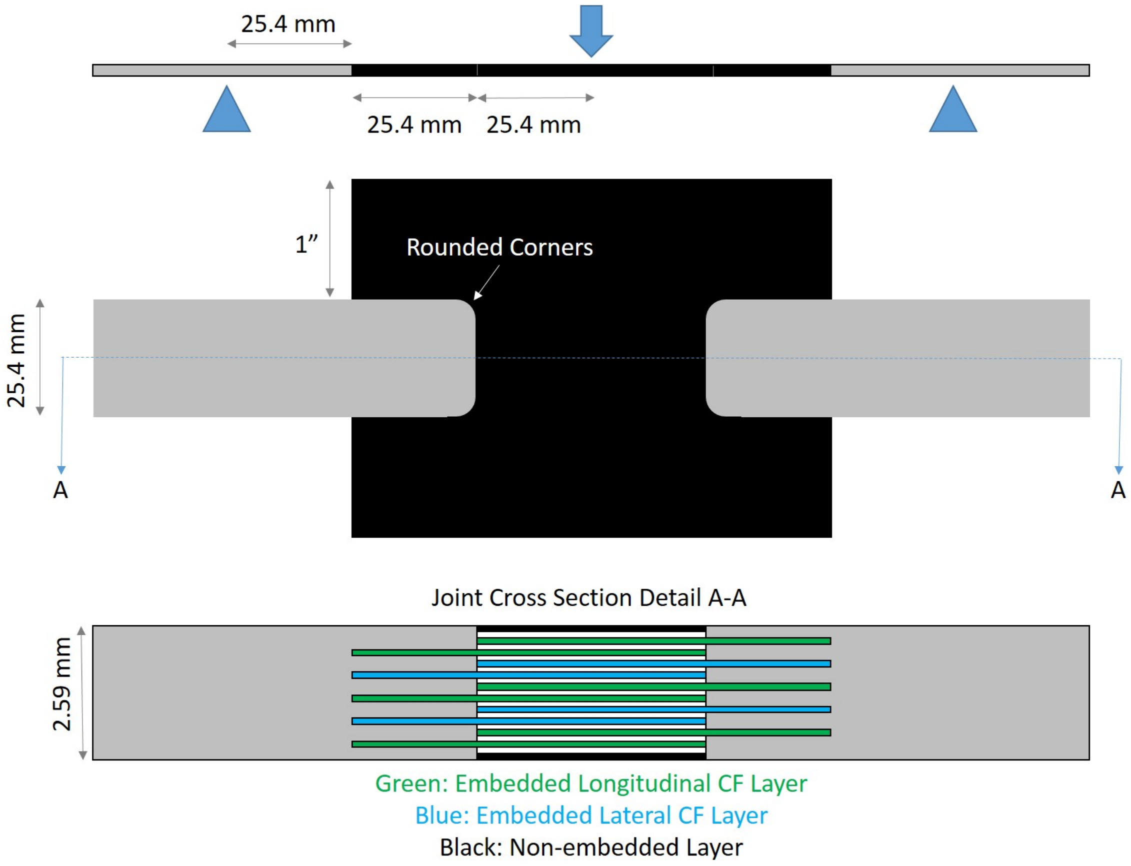
25.4 mm
25.4 mm
25.4 mm
1”
Rounded Corners
25.4 mm
A
A
Joint Cross Section Detail A-A
2.59 mm
Green: Embedded Longitudinal CF Layer
Blue: Embedded Lateral CF Layer
Black: Non-embedded Layer

Figure 3.23: Schematic of the five embedded layer three-point-bend specimen.

The same load frame and three-point-bend fixture were used as described earlier in Section 3.1.4. However, for this testing, DIC analysis was used in addition to load and displacement data from the load frame LVDT. The DIC cameras were setup on either side of the upper bending support, shown in Figure 3.24(a). Since the bending support was directly between the two cameras, the DIC analysis yielded two separate strain mappings, one for each CF-Al joint of the specimen, shown in Figure 3.24(b). The value of the DIC in this case was solely to provide strain data over the joint region since the test displacement data was taken directly from the LVDT.

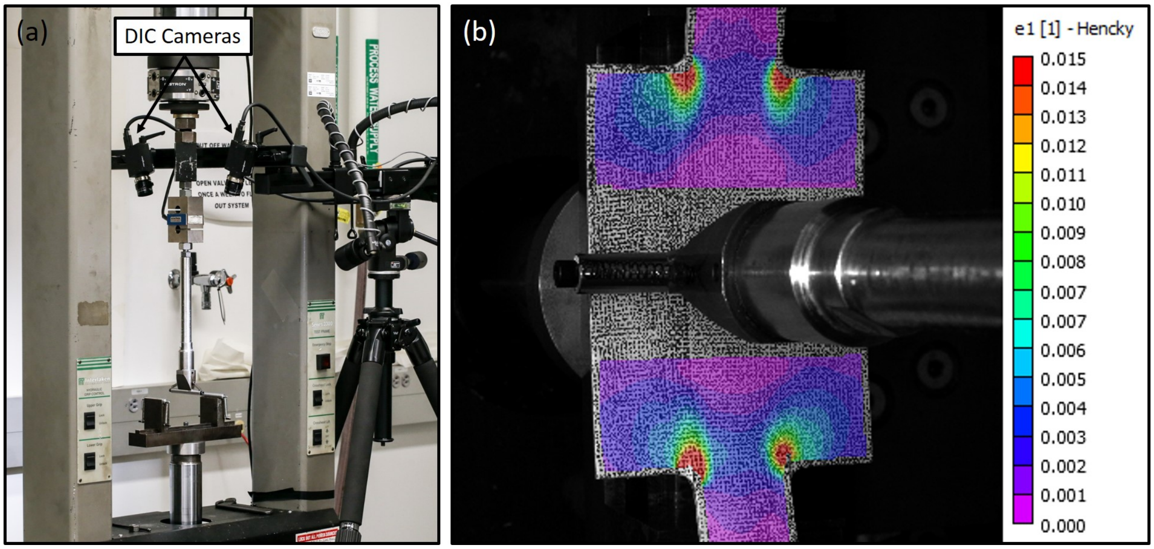
(a)
DIC Cameras
(b)
e1 [1] - Hencky
0.015
0.014
0.013
0.012
0.011
0.010
0.009
0.008
0.007
0.007
0.006
0.005
0.004
0.003
0.002
0.001
0.000

Figure 3.24: Three-point-bend DIC setup. (a) Camera positioning. (b) DIC strain mapping results.

Failure in the five embedded layer three-point-bend specimen occurred within one of the aluminum tabs before either of the aluminum epoxy interfaces failed. This occurred at a load of 590 N, a sizable increase in load bearing capability when compared to the three embedded CF layer joint (Figure 3.25). The maximum displacement before failure with the five layer joint was less than that of the three layer joint due to the aluminum tab failure. This aluminum tab failure occurred because of reduced cross sectional area and stress concentrations from the numerous channels housing CF in the region of failure (Figure 3.26). This is an area where improvements in joint design could be used to optimize joint performance in future phases of this research.

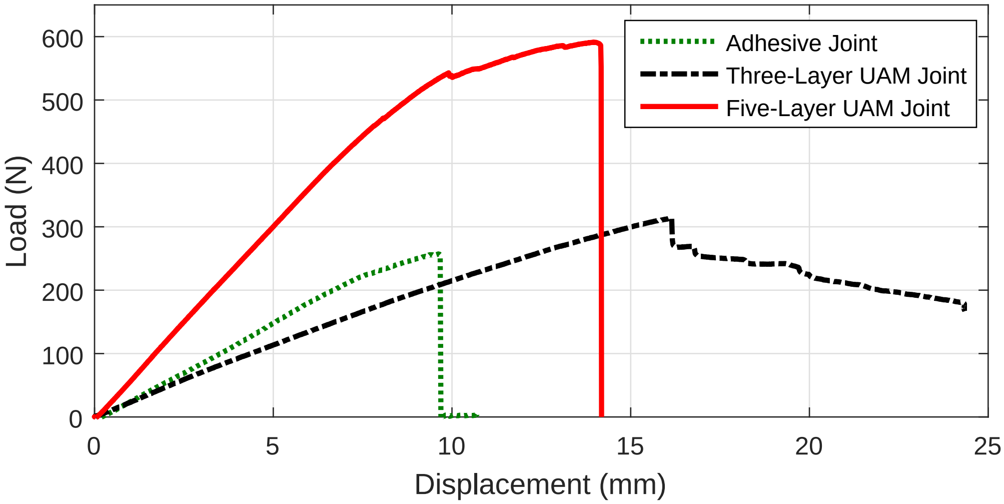

Figure 3.25: The five layer three-point-bend load vs. displacement curve compared with the three layer and adhesive joints.

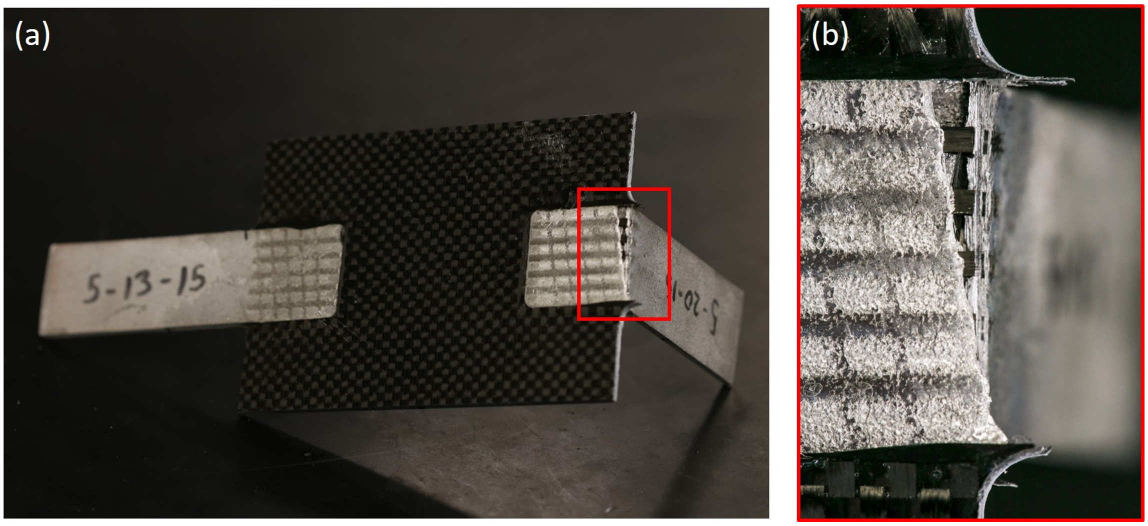

Figure 3.26: (a) Failed five layer three-point-bend specimen. (b) Detail of aluminum tab failure.

3.2.4 Discussion

This section has discussed manufacturing and testing of CF-Al joints with five layers of embedded CF. Manufacturing of these joints has been a feat in and of itself. These joints have more embedded CF than any created before. Embedding multiple layers of CF can easily present manufacturing issues since the substrate compliance increases with each additional embedded layer, making it difficult to achieve quality inter-laminate bonds. In this case, initial attempts at creating the five layer joints failed due to foil tearing, a phenomenon that often occurs when welding over filled channels that is discussed further in Chapter 5. Through trial and error it was discovered that by reducing the weld normal force while welding directly over the CF, foil tearing could be avoided.

The load carrying capacity of these joints was shown to be superior to the CF-Al joints with three layers of embedded CF. This was demonstrated through both tensile and three-point-bend tests. This increased load carrying capacity is due to the increased thickness of the five layer joints and increase in number of embedded CF tows. Further research work will be focused on increasing the joint load carrying capacity while maintaining a designated joint thickness.

3.3 Curved Channel CF-Al Joints

CF-Al joints utilizing straight channels to house the embedded CF have several problems. First of all, the maximum load is realized just before the aluminum/epoxy interface around the perimeter of the aluminum tab breaks. This means that the full potential of the embedded CF is not being used for carrying load. Another feature of the straight channel design that is not desirable are the blind channels with embedded

CF ends. Additionally, embedding free ended CF within blind channels would not be optimal in a mass manufacturing environment. The CF embedding process involves placing CF tows precisely into channels, this task becomes more difficult when the free end of the CF tows cannot be constrained or supported.

Because of reasons mentioned in the previous paragraph, an improved channel design was developed, featuring curved arc channels to house CF tows. The curved channels allow the CF tows to be constrained at two entry points into the aluminum structure. The curved channel CF-Al joints are also easier to manufacture since foil tearing is much less of a concern when purely transverse channels are not used as they were with the straight channels.

3.3.1 Joint Design and Manufacturing

Curved channel CF-Al joints are manufactured in a similar manner to straight channel designs with the primary difference being the channel design. The curved channel specimens feature three layers of embedded CF. The process starts by preparing the CF to be embedded. To accomplish this, a section of the bidirectionally woven HexTow AS4C 4000 3K CF is cut out. Some of the tows are removed as shown in Figure 3.27(a) such that two CF tows can be placed in each of four channels. Each layer of embedded CF tows is laid into a series of curved channels as pictured in Figure 3.27(c). For the curved channel design, it is important that the CF tows be wet with isopropanol while they are being situated into the channels. Making the CF to conform to the curvature is difficult otherwise.

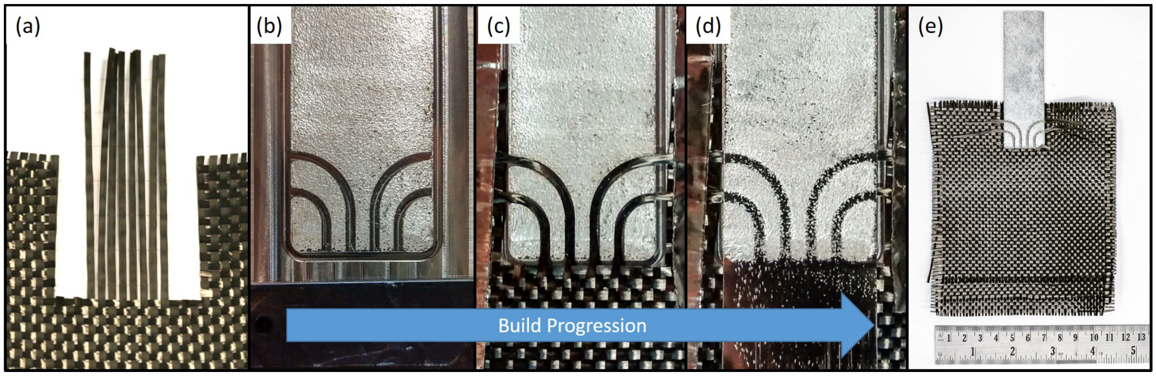

Figure 3.27: Curved channel CF-Al joint manufacturing progression. (a) CF is prepared for embedding by cutting and removing unwanted tows. (b) Channels are cut into base foil layers. (c) CF tows are placed into channels. (d) Aluminum foil is welded to consolidate the CF. (e) The joint is removed from the aluminum baseplate when the welding process is completed.

Once the CF is secured with adhesive tape and the isopropanol has evaporated, the CF tows are consolidated by welding 6061-H18 aluminum foil over them. This consolidation process is repeated for three layers of CF. The welding parameters that were typically used for creating the curved channel CF-Al joints are shown in Table 3.5. The stacking sequence used for the curved channel CF-Al joint construction was similar to what was used for the three layer straight channel design shown in Table 3.2. The channel dimensions used were 1.6 mm x 0.28 mm in width and depth respectively. As with earlier CF-Al joints, the aluminum baseplate was removed using UAM center subtractive milling operations (Figure 3.27(e)).

Table 3.5: UAM parameters used for curved channel CF-Al joints.

Welding Force	4000 N (2500 N over channels)
Welding Speed	508 cm/min
Amplitude	33 μm
Heat-plate Temperature	Room Temperature (22 C°)
Spot Dwell	300 ms
Sonotrode Roughness	14 μm

With the curved channel design, each of the three embedded layers were stacked directly over one another. Stacking the channels in this manner can be problematic because it reduces the aluminum cross sectional area over the channel region. However, stacking the channels in this manner increases the bonding quality throughout the channel region because of the aluminum continuity in the islands between the channels. This lends towards improved substrate stiffness of the overall structure. This paired with eliminating the transverse straight channels (perpendicular to the weld direction) greatly improved manufacturing repeatability. Foil tearing can still occur occasionally when welding over the curved channels filled with CF tows. However, by using a sufficiently low normal force, i.e. 2500 N, foil tearing occurrence becomes abnormal.

3.3.2 Tensile Testing

During curved channel CF-Al joint manufacturing, specimens with a number of different thicknesses were created. The first two designs had thicknesses of 1.60 mm and 2.03 mm. Each specimen had three layers of embedded CF tows housed in curved channels. These tensile specimens were loaded into the Interlocken load frame described in Section 3.1.3 and were pulled to failure. The DIC system described in Section 3.1.3 was used to obtain displacement data and strain mapping. The displacement data used in the load vs. displacement curves was determined by placing a virtual extensometer across the tensile joint region within the DIC analysis software. The length of the virtual extensometer was kept at 46 mm for each of specimen. Figure 3.28 shows load vs. displacement curves for the two curved channel CF-Al designs and compares them with the highest performing three layer, straight channel joint from Section 3.1.3.

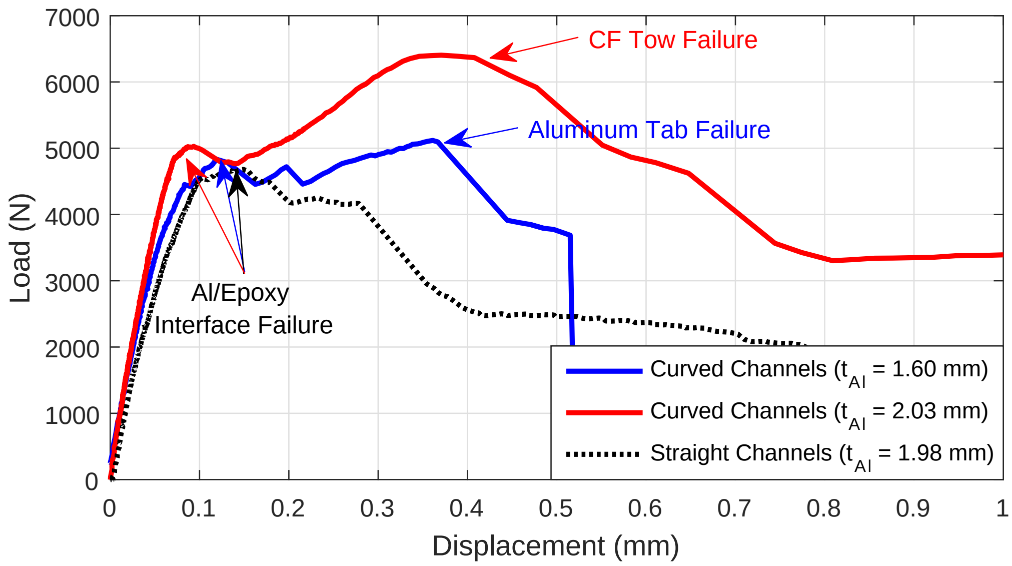

Figure 3.28: Load vs. displacement for two thicknesses of curved channel CF-Al joints compared with the straight channel design.

The maximum load of the thinner of the curved channel specimens was 4800 N, while the thicker of the curved channel specimens had a maximum load of 6400 N.

Like the three layer, straight channel design, each specimen had aluminum/epoxy interfacial failure somewhere between 4700 N and 5000 N. After this point in the testing, the failure modes observed for the specimens were all different. After the aluminum/epoxy adhesive failure, the straight channel specimen continued to loose load as CF tow pullout occurred. Both of the curved channel specimens began to gain load again after the initial adhesive failure. The aluminum tab of thinner curved channel specimen failed at 5100 N at the area of reduced cross section at the location of the large arc channels. The thicker of the curved channel specimens did not fail in the aluminum, but continued to gain load until the CF tows began to break within the curved channels at 6400 N. The thinner curved channel failure sequence is shown in Figure 3.29 by DIC strain overlaid onto the specimen.

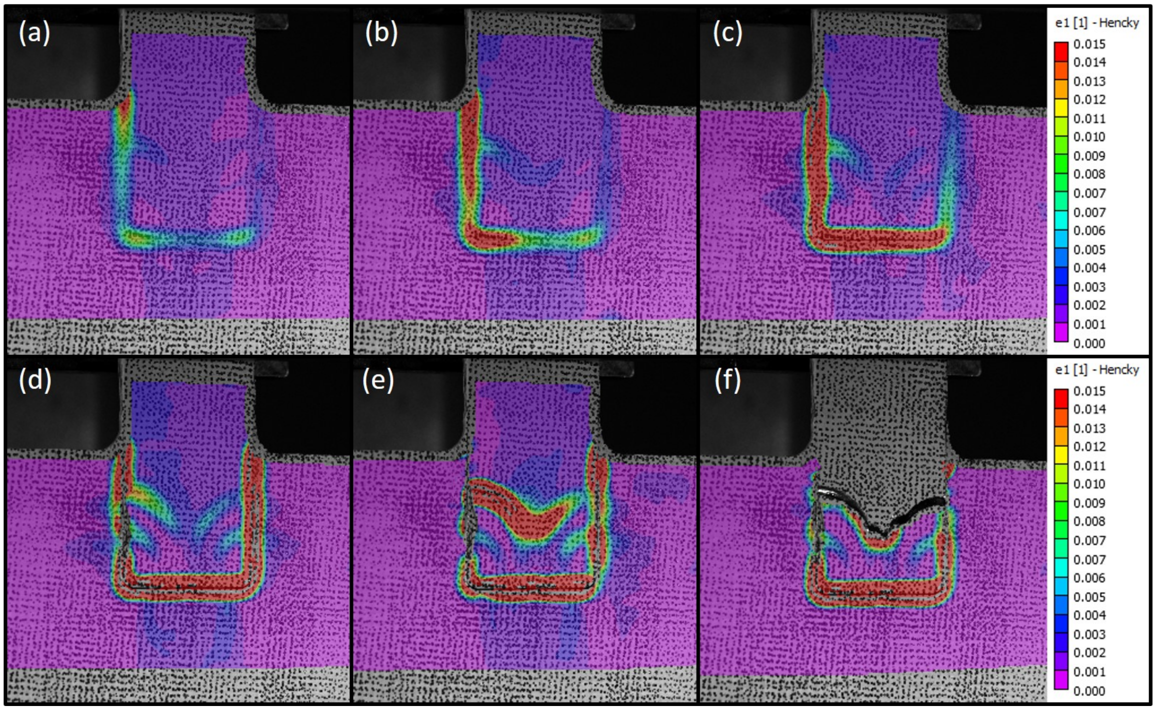

Figure 3.29: Thin curved channel CF-Al joint failure sequence: (a) Cracking initiates in the left inside corner between the aluminum tab and CFRP plate. (b) Cracking propagates. (c) Cracking continues to propagate. (d) Entire aluminum tab interface has separated from the bulk CFRP. (e) Crack initiates in aluminum tab at upper left channel. (f) Aluminum tab failure.

After the CF tows began to break during testing of the thicker specimen, the test was continued while the broken CF tows were pulled out of the aluminum structure. Figure 3.30 shows images of both failed specimens. The CF tows in the thicker specimen broke in a combined shear/tensile loading near the mid-section of the channel arcs, shown in Figure 3.30(c).

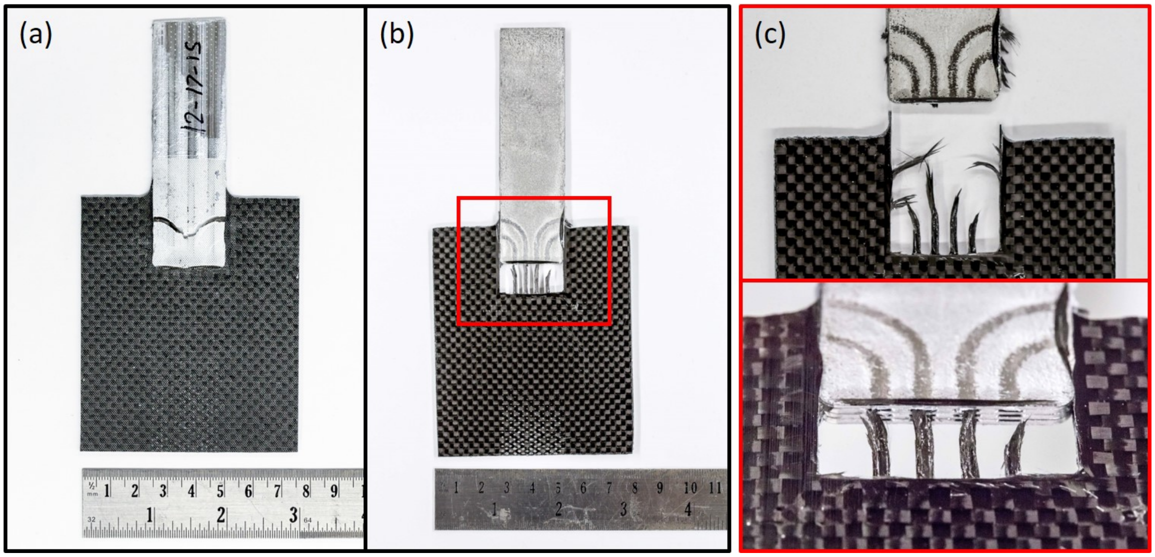

Figure 3.30: (a) Failed thin curved CF-Al tensile specimen. (b) Failed thicker CF-Al tensile specimen. (c) Detail of failed thicker CF-Al tensile specimen.

3.3.3 Discussion

Tensile testing showed that the curved channel CF-Al joints show more promise than the straight channel CF-Al joints. The load at initial failure was similar between both joint designs, but for CF-Al joints of the same thickness, the curved channel design had a greater peak load as well as greater energy dissipation. The main problem with each of the designs is that the initial failure is purely based on the adhesive interface around the perimeter of the aluminum tab. Design features are needed to equip the CF-Al joints with a greater adhesive surface area to increase the load at which the specimens first experience damage.

3.4 Curved Channel Joints with Increased Adhesive Joining Area

Since the CF-Al joints discussed in Section 3.3 showed first damage during testing at the adhesive interface around the perimeter of the aluminum tab, two concepts for increasing the adhesive joining surface area were generated. The first method was to increase the adhesive surface area by extending aluminum foil layers further into the CFRP portion of the joint construction. This concept is referred to as the flange joint. The other concept was extending layers of bidirectional CF fabric over the upper and lower surfaces of the aluminum tab. This second concept is referred to as the CF sandwich joint.

3.4.1 Joint Design and Manufacturing

CF-Al Curved Channel Flange Joint

The curved channel CF-Al joint utilizing the flange concept was created by welding two oversized foil layers over the first and second layers of embedded CF tows. The oversized aluminum foil was the exact same 6061-H18 aluminum rolled material as was used for the aluminum tab. The flange layers were made to overhang 6.4 mm over the perimeter of the aluminum tab. These layers were cut out of a sheet of 0.15 mm thick 6061-H18 aluminum material and manually laid onto the welding substrate as shown in Figure 3.31. After the flange joint specimen welding was completed, the baseplate was removed by UAM center subtractive milling operations. The flange portion was then trimmed away except for the joint region. The joint was then laid up with epoxy and additional bidirectional CF layers using hand layup techniques and vacuum bagging. The completed thickness of the aluminum tab was 1.60 mm.

Figure 3.32 shows the completed structure which looks identical to the curved channel specimens from Section 3.3.1 since the flange is completely integrated within the CFRP.

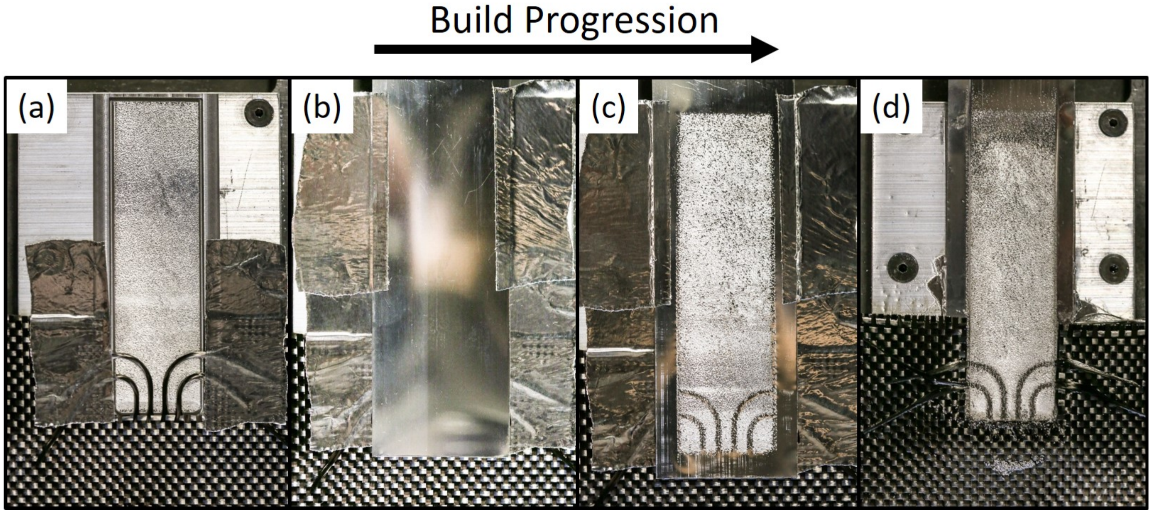

Figure 3.31: CF-Al joint construction featuring the flange concept. (a) CF is placed into channels, (b) Flange material is manually laid over channels, (c) Flange material is welded over the CF, (d) Completed structure with two integrated flanges.

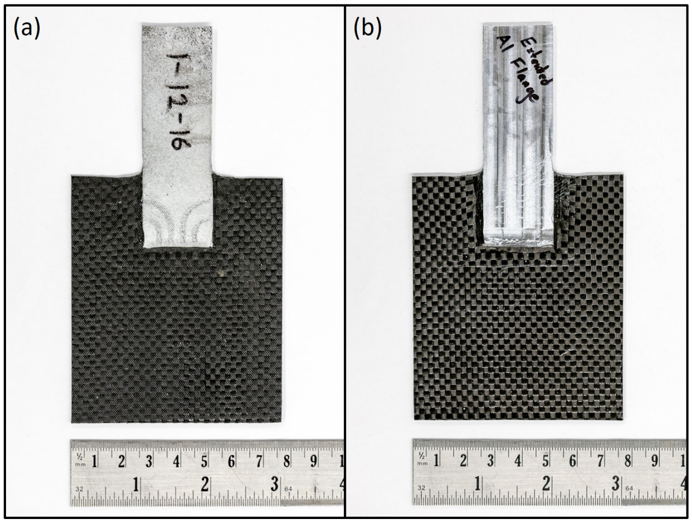

Figure 3.32: CF-Al curved channel tensile specimen with the flange feature. (a) Front, (b) Back.

CF-Al Curved Channel Joint with CF Sandwich Feature

The CF-Al curved channel joint with the CF sandwich feature is manufactured via UAM in exactly the same manner as the curved channel joints discussed in Section 3.3.1. The only difference in design comes into play during the layup process when additional bidirectional CF layers are integrated into the structure on the upper and lower surfaces of the joint area as pictured in Figure 3.33. The total thickness of the aluminum tab for this joint was 1.60 mm.

This CF sandwich design essentially produces a joint that is a hybrid of UAM embedded CF integration and adhesive double lap joining. This design is more representative of how a UAM CF-Al joint might be integrated into a structural application than previous designs. However, since the joint involves adding adhesive lap components which cover the embedded CF features, it is more difficult to do analysis and joint performance optimization on the embedded CF portion of the joint. This is particularly true since the DIC measurement system can only resolve strains that cameras can view on the exterior of the structures.

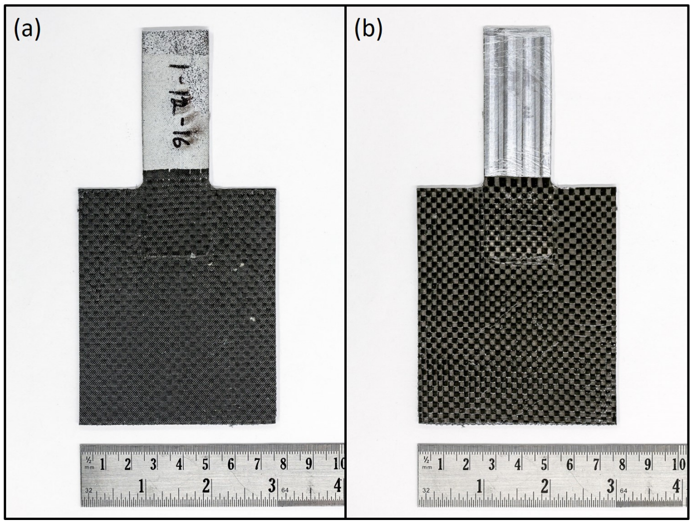

Figure 3.33: CF-Al curved channel tensile specimen with the CF sandwich feature. (a) Front, (b) Back.

3.4.2 Tensile Testing

The same tensile testing methods used in Section 3.3.2 were used on the CF-Al joints with curved channels and increased adhesive bonding area. A loading rate of 1.27 mm/min was used. Once again, the DIC system was used to capture displacement and strain mapping for the two specimens, while load was input into the DIC program from the load cell on the Interlocken frame.

The results for the two different methods of increasing the adhesive surface area were strikingly different. In each case, the increased adhesive bonding area prevented early failure around the aluminum tab perimeter. However, for the aluminum flange case, the flange material did not prevent the crack from initiating in the inside corner of the specimen between the aluminum tab and CFRP region. This crack quickly propagated to the beginning of the large arc channel and continued through the aluminum tab at the area of reduced cross section, causing complete failure at 4500 N. This performance was poorer than the CF-Al joints without any additional surface bonding area. DIC strain maps overlaid on the structure illustrate the crack initiation and propagation, shown in Figure 3.34. The downfall of aluminum flange design is that as manufactured, the flange actually makes the joint more vulnerable to crack initiation and aluminum tab failure.

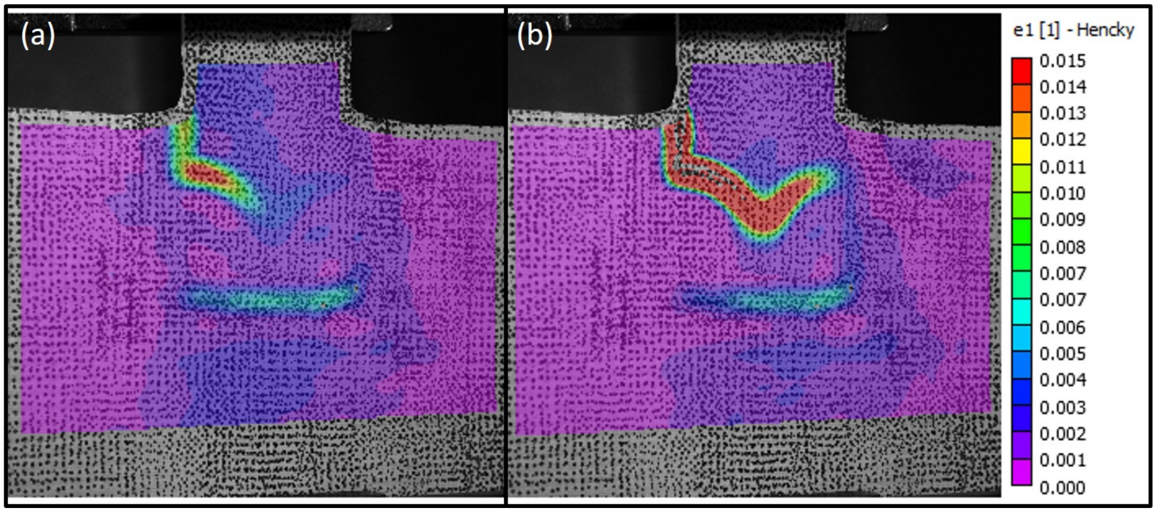

Figure 3.34: DIC strain mapping of the CF-Al joint with curved channels and the aluminum flange feature. (a) Crack initiation, (b) Crack propagation.

The curved channel CF-Al joint with the CF sandwich feature performed significantly better than the joint with the flange feature. The CF bidirectional fabrics covering the upper and lower aluminum tab surfaces provided extensive adhesive surface area. They also were effective in preventing crack initiation at the inside corners between the aluminum tab and CFRP structure. This resulted in a maximum failure load of 8500 N, nearly twice the load achieved for the joint with the flange feature. Load vs. displacement curves for the two CF-Al joints with increased surface area are compared with the original CF-Al curved channel joint in Figure 3.35.

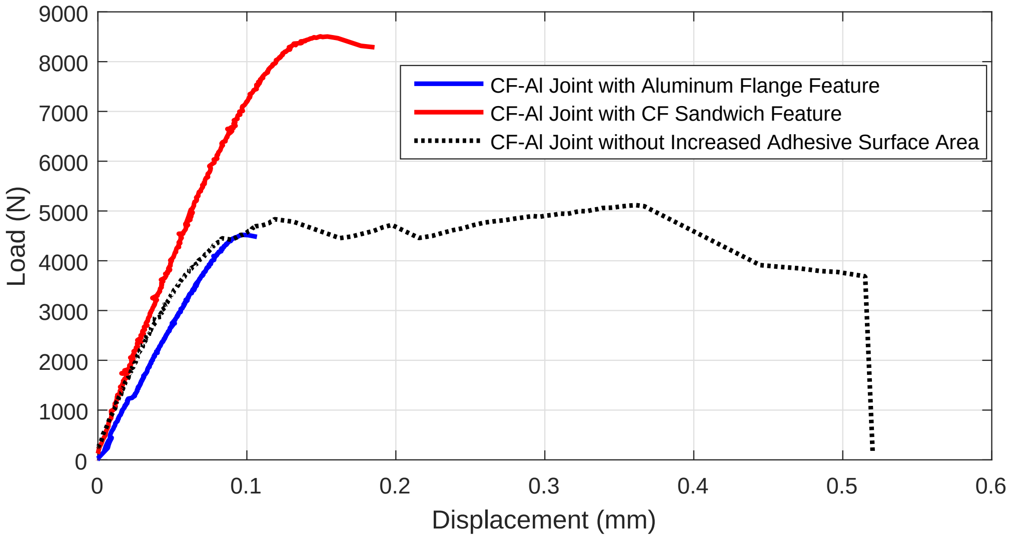

Figure 3.35: Load vs. displacement curves for CF-Al joints with increased adhesive bonding area features compared with the original CF-Al curved channel design.

After initial one-off joint construction and testing was completed with the CF sandwich feature joint, five additional specimens with the sandwich feature were created for a study comparing its strength to that of adhesive single lap joining, since adhesive single lap joints are currently the standard method of joining aluminum and CFRP in industry. Though five such specimens were created, the fifth one was defective due to severe foil tearing during the manufacturing process, meaning that only the first four specimens are used in the comparison. The specimens were created slightly thicker than the one-off joints, with an aluminum tab thickness of 1.75 mm. In addition to the five CF-Al tensile specimens with the sandwich feature, a sixth specimen was created with the sandwich feature, but with no embedded CF. This was done to evaluate the load carrying contribution of the embedded CF. The completed six specimens are shown in Figure 3.36. Load vs. displacement curves for each of the test specimens are shown in Figure 3.37 and the tensile test results summary is provided in Table 3.6.

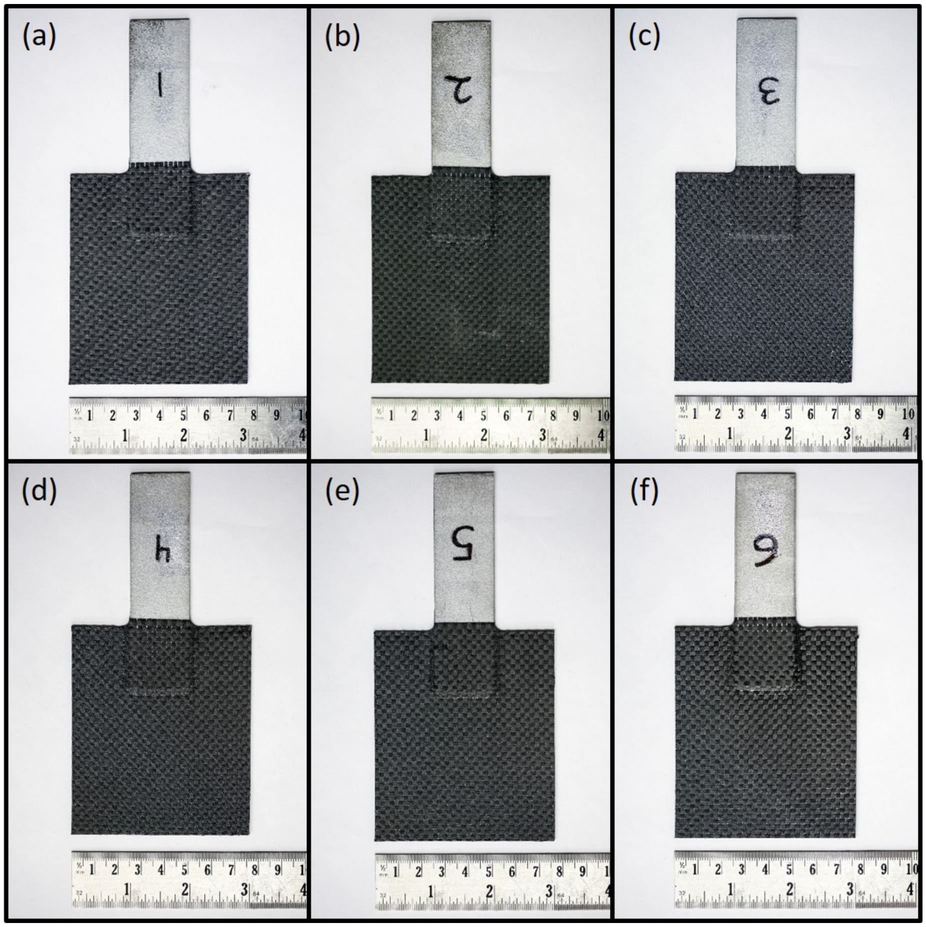

Figure 3.36: (a-e) CF-Al joints with curved channels and CF sandwich features. (f) CF-Al sandwich feature joint without embedded CF.

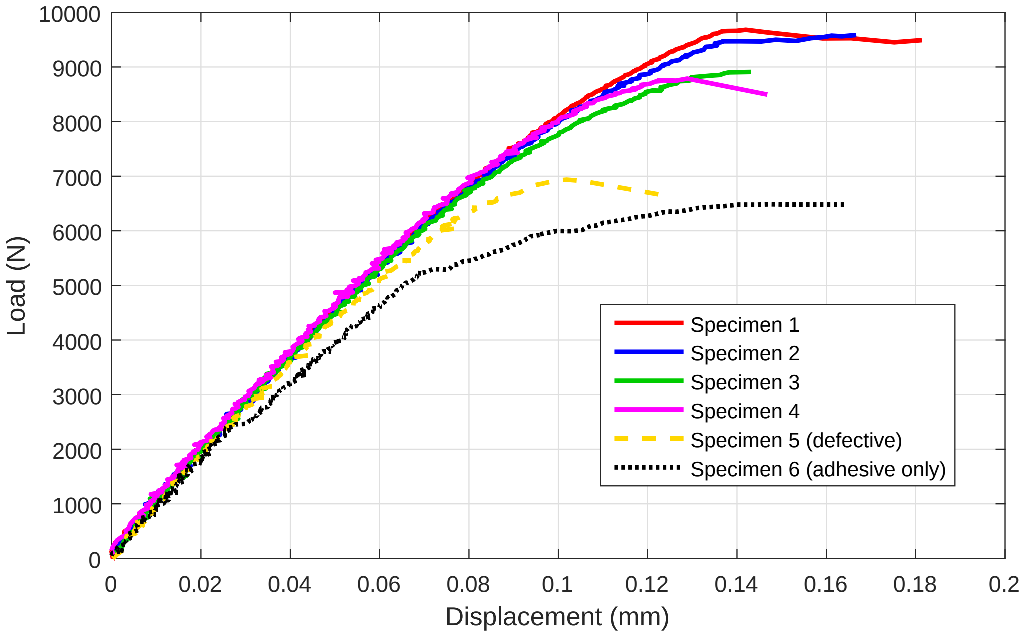

Figure 3.37: Tensile testing load vs. displacement curves CF-Al joints with CF sandwich features.

Table 3.6: Tensile testing summary for CF-Al joints with CF sandwich features.

Joint	**Peak Load**	**Failure Mode**
Specimen 1	9681 N	Adhesive and Al tab failure
Specimen 2	9585 N	Adhesive and Al tab failure
Specimen 3	8909 N	Adhesive and Al tab failure
Specimen 4	8787 N	Adhesive and Al tab failure
Specimen 5 (defective)	6937 N	Adhesive and Al tab failure
Specimen 6 (adhesive only)	6486 N	Adhesive failure
Average (Specimens 1-4)	**9241 N**	
Standard Deviation (Specimens 1-4)	**458 N**	

Tensile testing results from the CF-Al joints with curved channels and sandwich features confirmed that the use of the sandwich features are influential for increasing the joint strength up to nearly 10 kN. Test specimen 6 which had no embedded CF failed at less than 6500 N. This maximum load is greater than UAM CF-Al joints without sandwich features, but far less than the joints with both embedded CF and the CF sandwich feature. This confirmed that the embedded CF does contribute substantially to the joint load carrying capability. DIC strain maps of the failure processes also confirm that the embedded CF helps to prevent adhesive failure at the end of the aluminum tab. For specimen 6 (sandwich feature only, purely adhesive), failure initiated at the end of the aluminum tab at a load of 6486 N, shown in Figure 3.38(a). For specimens 1-5, failure did not initiate at the end of the aluminum tab. Instead, failure occurred at the edge of the CF covering the tab and at a much higher load, shown in Figure 3.38(b). Failure for these specimens consisted of two simultaneous failures: adhesive failure of the aluminum/epoxy interface and aluminum tab failure at the region of reduced cross section over the large arc channels. The failed specimens 1-6 are shown in Figure 3.39.

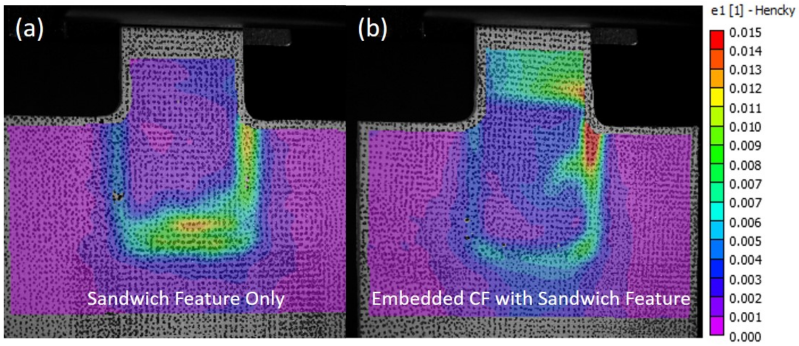

Figure 3.38: Strain maps overlaid on specimens during failure. (a) DIC strain map of a CF-Al joint with the sandwich feature and no embedded CF. (b) DIC strain map of a CF-Al joint with curved channels and the sandwich feature.

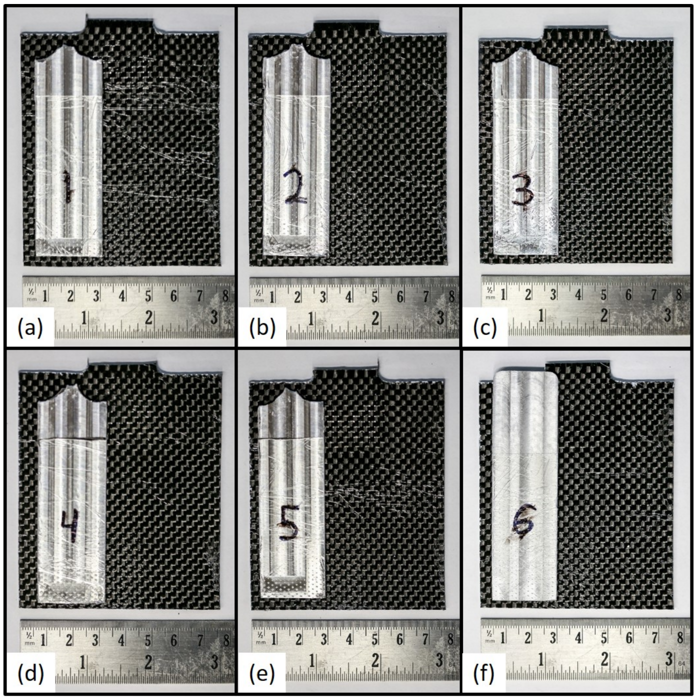

Figure 3.39: (a-e) Failed CF-Al joints with CF embedded in curved channels and sandwich features. (f) Failed CF-Al adhesive sandwich joint.

3.4.3 Discussion

In conclusion, two concepts for increasing the adhesive bonding area were built and tested: one of them utilizing an extension of the aluminum tab into the CFRP structure (flanged concept) and a second using two additional bidirectional CF layers to cover the upper and lower sides of the aluminum tab (CF sandwich concept). Each increased the adhesive bonding surface area and each prevented cracking from propagating around the perimeter of the aluminum tab. However, the aluminum flange concept did not help prevent cracking from initiating in the joint inside corner stress concentrations and did not provide reinforcement to the aluminum tab over its region of reduced cross sectional area. The CF sandwich concept on the other hand did strengthen the joint inside corners and region of reduced cross sectional area. These factors resulted in a high maximum load (avg. - 9241 N) for the joints featuring the sandwich concept.

Incorporating a design with CF covering the aluminum tab was an important step in UAM CF-Al joint design. However, the joints in this section are still far from being optimized for maximum strength. The most immediate problem with this design is that the the reduced cross sectional area over the channels forces failure in the aluminum tab. Ideally a channel design should be implemented that has less stress concentrations and a less severe cross sectional area reduction caused by the channels housing the CF. This is all work that future research should address.

3.5 Cross Tensile Joints

In addition to tension and three-point-bend testing, cross tensile testing was performed on UAM CF-Al joints. Cross tensile loading is an important testing condition for a number of joining technologies, most notably resistive spot welding. Comparing UAM CF-Al joints with existing joining technologies is the primary motivation for this testing. Unfortunately, the geometry of the CF-Al specimens used for the tensile and three-point-bend testing is not appropriate for cross tensile testing. Because of this, an entirely new joint geometry was developed. The cross tensile test and joint geometry chosen was based primarily off of the JIS Z 3137 standard.

3.5.1 Joint Design and Manufacturing

Cross tensile testing involves a joint of two materials which are joined in a cross pattern. A cross tensile testing fixture is used to secure either end of both of the joint materials and constrain them from displacement or rotation outside of the loading direction. During the test, the two halves of the cross tensile testing fixture are pulled apart, thereby pulling the cross tensile specimen to failure. A schematic for two of the UAM CF-Al cross tensile testing specimen designs is shown in Figure 3.40. The first design includes only embedded CF through the aluminum tab, while the second design includes both embedded CF and the CF sandwich feature which was introduced in Section 3.4.1.

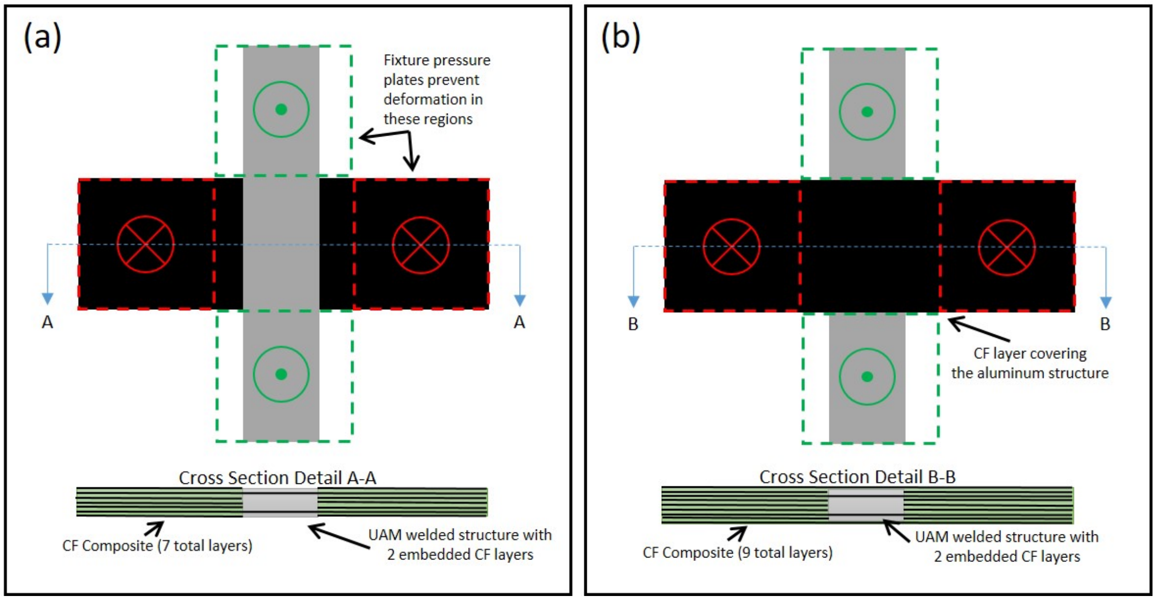
(a)
Fixture pressure plates prevent deformation in these regions
A
A
Cross Section Detail A-A
CF Composite (7 total layers)
UAM welded structure with 2 embedded CF layers
(b)
B
B
CF layer covering the aluminum structure
Cross Section Detail B-B
CF Composite (9 total layers)
UAM welded structure with 2 embedded CF layers

Figure 3.40: Cross tensile CF-Al joint schematics: (a) Without sandwich feature. (b) With sandwich feature.

The UAM portion of the manufacturing processes for the two cross tensile specimen designs shown in Figure 3.40 are identical. The only difference comes into play during the composite layup process. The specimens were created by welding 6061-H18 aluminum foil onto a large 30 cm x 15 cm 6061-T6 aluminum baseplate. After four layers of foil were welded, nine straight channels were cut across the width of the aluminum with width and depth of 1.59 mm x 0.30 mm respectively. The spacing between channels was 4.23 mm to fit the CF weave spacing. Bidirectional fabric made of HexTow AS4C 4000 3K CF tows was prepared for consolidation by removing unwanted CF tows. The two remaining portions of bidirectional CF fabric were connected by eighteen CF tows which were placed into the channels, two tows per channel. Isopropanol was used to situate the CF nicely into the channels. After the isopropanol had evaporated, five layers of the aluminum foil were welded over the

CF tows. At this point, a second set of channels were cut and the second layer of CF tows were laid into the channels. Two final layers of aluminum foil were welded over the second layer of embedded CF tows, completing the welding process. After the specimens were welded, mounting holes were cut into the aluminum tabs and the specimens were removed from the baseplate. The total cross tensile joint aluminum thickness was 1.65 mm. The building process setup is illustrated in Figure 3.41(a) and the welding parameters used are shown in Table 3.7.

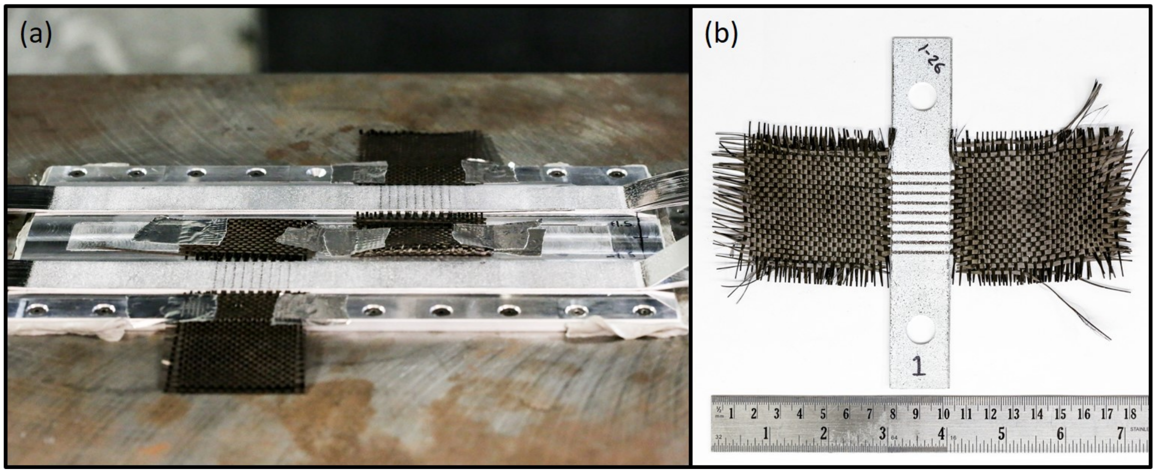

Figure 3.41: (a) Cross tensile specimens being manufacturing in UAM center. (b) One of the cross tensile joints after baseplate removal.

Table 3.7: UAM parameters used for cross tensile CF-Al joints.

Welding Force	4000 N (2000 N over channels)
Welding Speed	508 cm/min
Amplitude	32.4 μm
Heat-plate Temperature	Room Temperature (22 C°)
Spot Dwell	300 ms
Sonotrode Roughness	14 μm

After baseplate removal, the specimens were laid up with additional bidirectional CF fabric layers and Fibre Glast System 2000 epoxy by hand layup techniques. Vacuum bagging was used to remove air and excess epoxy from the laid up specimens. After allowing the epoxy to cure, fixture mounting holes were drilled into the CFRP plate to finish out the specimens. Figure 3.42 shows images of the two completed CF-Al cross tensile joints. The first with only embedded CF layers and the second with embedded CF and the CF sandwich feature.

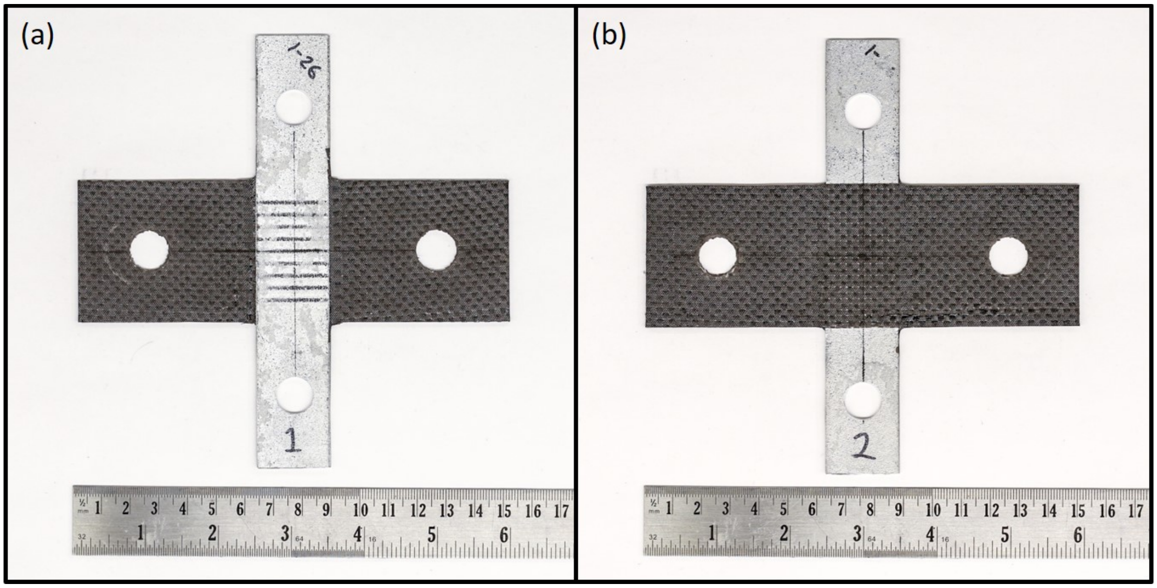

Figure 3.42: Finished cross tensile joints. (a) CT joint with embedded CF only. (b) CT joint with embedded CF and CF sandwich feature.

3.5.2 Cross Tensile Testing

Cross tensile testing was competed in accordance with Japanese standard JIS Z 3137. The loading rate used for the test was 5 mm/min. The built in-house JIS Z 3137 fixture was used in conjunction with the SMSL Interlocken load frame and MTS grips, shown in Figure 3.43(b). Load and displacement were recorded during the testing by a National Instruments data acquisition system and laptop computer with LabVIEW in conjunction with a 5000 N load cell and load frame LVDT. The DIC system was not used for the cross tensile testing since the cross tensile fixture prevents any optical viewing of loaded specimens.

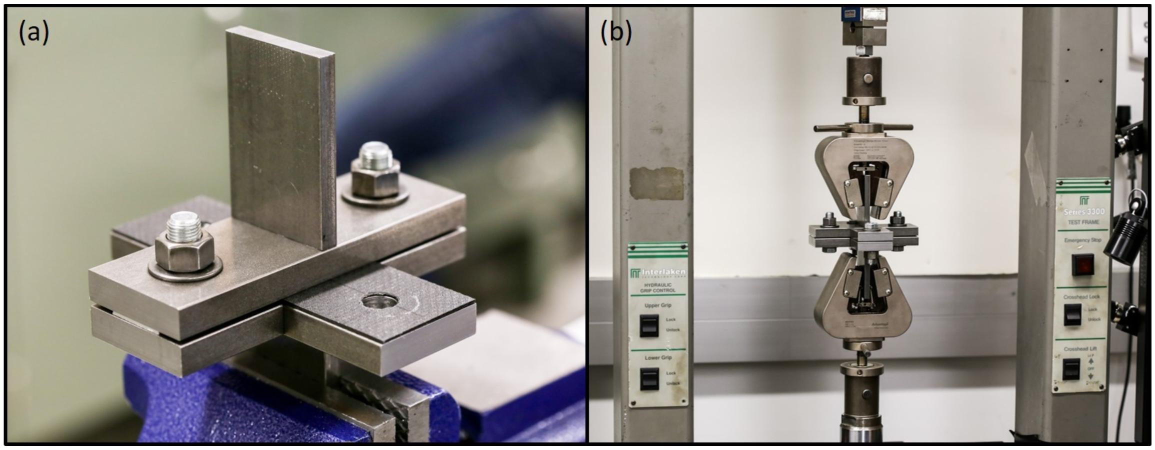

Figure 3.43: (a) Mounting a cross tensile specimen into the cross tensile loading fixture. (b) Cross tensile testing setup, with Interlocken load frame, MTS grips, and in-house built loading fixture.

The two cross tensile specimen designs performed similarly, each failing in the aluminum tab where the outermost CF tows were embedded (Figures 3.45). As expected, the specimen with CF covering the aluminum tab was the stiffest because of the added material over the joint and CFRP areas. The maximum loads at failure were similar at around 2500 N, with the specimen with the CF sandwich feature performing slightly better (Figure 3.44). However, the first signs of damage occurred in the joint with the sandwich feature before the specimen with only embedded CF. This was because of initial cracking of the CF sandwich layers covering the aluminum tab. Complete aluminum failure occurred in only one side of the aluminum tab for each specimen. After this initial failure, the fixture halves became misaligned since only one side of the CF/Al joint remained intact to carry load. Because of the misalignment after the initial failure, the tests were stopped before the remaining sides of the aluminum tabs broke off.

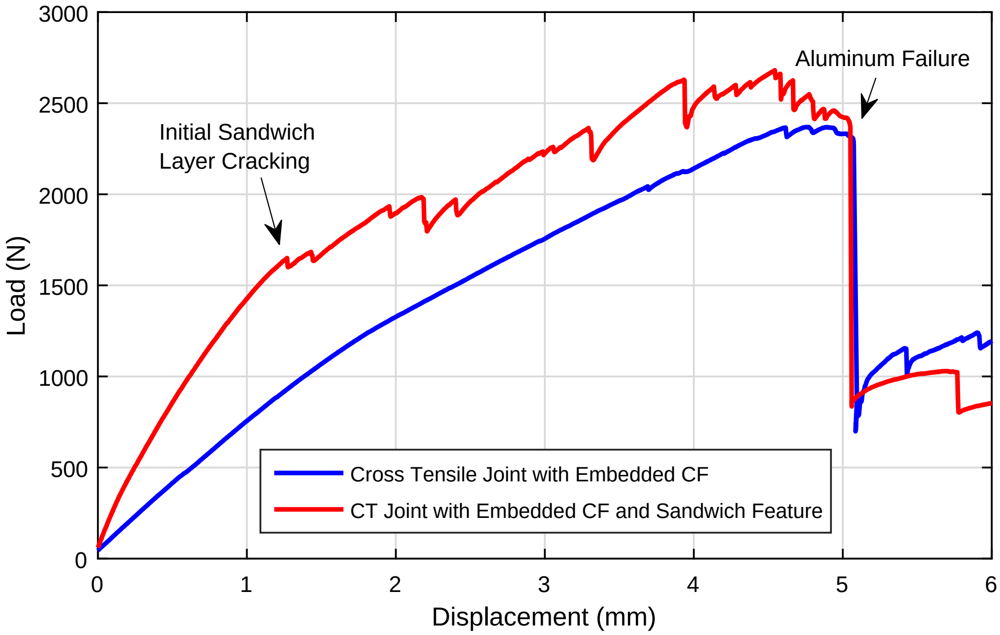

Figure 3.44: Cross tensile CF-Al joint load vs. displacement curves.

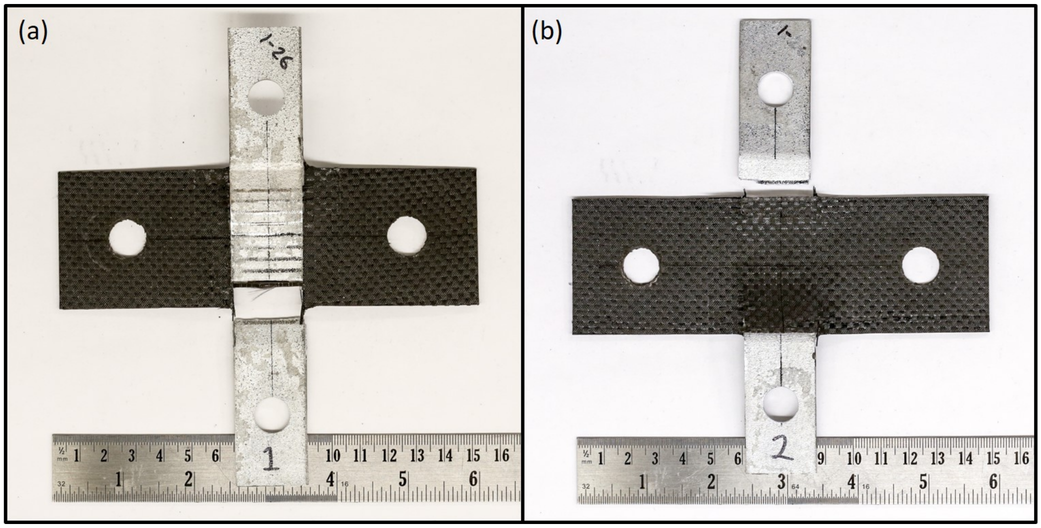

Figure 3.45: Failed cross tension joints. (a) Cross tensile joint with embedded CF only. (b) Cross tensile joint with embedded CF and CF sandwich feature.

The results from the cross tensile testing showed that using the sandwich feature for the cross tensile loading condition does not greatly improve the CF-Al joint performance. However, since the sandwich feature was used for the five tensile joints discussed in Section 3.4, a batch of four cross tensile CF-Al were constructed with sandwich features for consistency between tensile and cross tensile designs. In addition, a fifth cross tensile specimen was created with the CF sandwich feature, but no embedded CF. This was done to evaluate the load bearing contribution of the embedded CF compared to the exterior CF sandwich layers. The aluminum tab thickness of each of these five specimens was 1.75 mm (to match the thickness used for the tensile specimen patch). Images of the batch of cross tensile specimens is are shown in Figure 3.46.

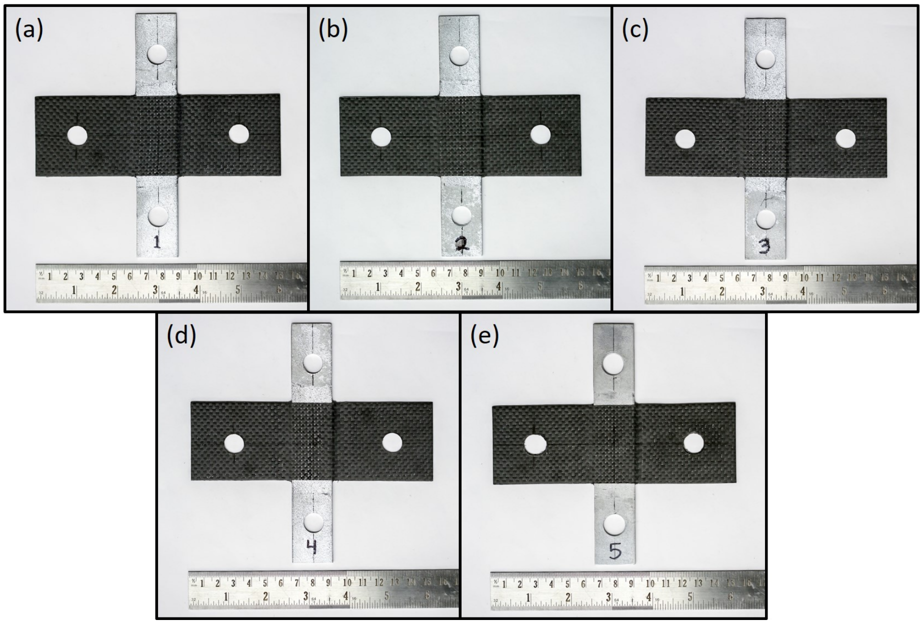

Figure 3.46: (a-d) CF-Al cross tensile joints with embedded CF and CF sandwich features. (e) CF-Al joint with sandwich feature, but no embedded CF.

The same cross tensile testing procedure explained earlier in this section was used on the batch of five cross tensile specimens. The average peak load of the joints with both embedded CF and the CF sandwich feature was 3370 N with a standard deviation of 363 N. The cross tensile without embedded CF attained a slightly lower maximum load at 2766 N. For each of the specimens, initial CF sandwich layer cracking occurred at around 1800 N and continued cracking up to the ultimate load where one side of the aluminum tabs failed. Cross tensile specimen 5 (no embedded CF) failed by the CF sandwich layer shearing off in some regions and delaminating from the aluminum tab and remaining CFRP shown in Figure 3.48(f). The testing load vs. displacement curves can be found in Figure 3.47. Additionally, images of the failed cross tensile specimens are shown in Figure 3.48. Finally, Table 3.8 provides a summary of the cross tensile testing of the 1.75 mm thick CF-Al cross tensile joints.

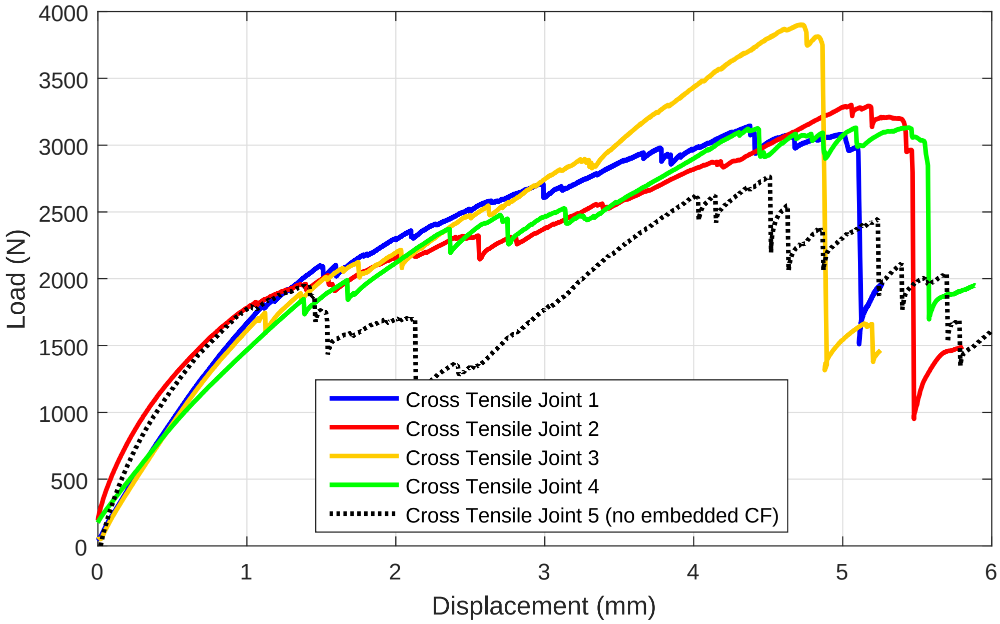

Figure 3.47: Load vs. displacement of CF-Al cross tensile testing.

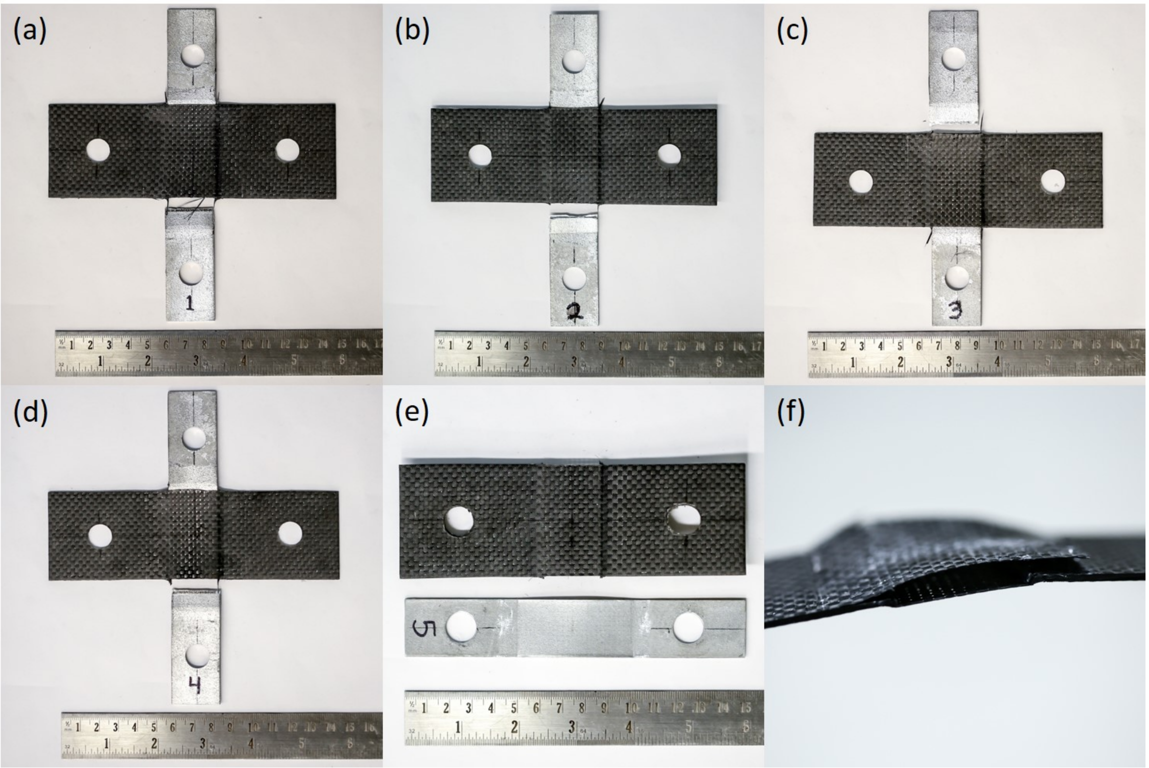

Figure 3.48: Failed CF-Al cross tensile joints. (a-e) Joints with embedded CF and sandwich features. (e) Joint with no embedded CF, adhesive only. (f) Detail of CF sandwich delamination and shearing from specimen 5.

Table 3.8: Cross tensile testing summary for CF-Al joints with CF sandwich features.

Joint	**Peak Load**	**Failure Mode**
Specimen 1	3145 N	Aluminum tab failure
Specimen 2	3300 N	Aluminum tab failure
Specimen 3	3902 N	Aluminum tab failure
Specimen 4	3132 N	Aluminum tab failure
Specimen 5 (adhesive only)	2766 N	CF fracture and delamination
Average (Specimens 1-4)	**3370 N**	
Standard Deviation (Specimens 1-4)	**363 N**	

3.5.3 Discussion

In conclusion, CF-Al cross tensile joints were designed that would be compatible with the JIS Z 3137 cross tensile testing standard. Two types of UAM CF-Al cross tensile specimens were created: one that used two embedded layers of CF tows to joint the CFRP and aluminum components, the other included the embedded CF but also incorporated CF sandwich layers as introduced for the tensile specimens in Section 3.4. The results from this first cross tensile testing comparison showed that the addition of the CF sandwich layers did not provide substantial additional strength. However, for consistency with the tensile joints from Section 3.4.2, the CF sandwich feature was incorporated with the batch of four cross tensile specimens. These specimens ended up having an average maximum load of 3370 N. This maximum load will later be compared with that of adhesive single lap joints in Section 4.3.

The reason why the addition of the CF sandwich features do not greatly increase the maximum achievable load is because the aluminum tab is the weakest component. In every case, failure occurred at the region of reduced cross sectional area at either the first or last of the nine channel locations. Specimen 5 which had no channels going though the aluminum structure experienced substantial yielding in the aluminum, but did not break within the aluminum. Instead this cross tensile joint failed from the CF sandwich layers delaminating from the aluminum and remaining CFRP components. The maximum load seen during testing of this joint was slightly lower (2766 N) than the joints which used embedded CF tows. This validates the use of embedded CF. However, design optimization would be very helpful for increasing the strength of the aluminum at the region of reduced cross section over the channels.

It could be argued that the cross tensile joints do not relate directly to the curved channel CF-Al joints since the joint and channel geometries are quite different. This is certainly a valid point. What the two joints do have in common in addition to the joint thickness is the method of construction. Using this train of thought, the curved channel joints and cross tensile joints though different in design, feature the same joining technology, which is UAM CF consolidation. They are both examples of how the UAM process can be used to create joints specific to a particular loading condition.

3.6 CF-Al UAM Joint Summary and Discussion

This chapter has discussed how the concept of consolidating CF tows via UAM technology can be used to create joints between CFRP and 6061-H18 aluminum. A number of different CF-Al joint designs utilizing embedded CF tows were constructed. These included three layer-straight channel joints, five layer-straight channel joints, curved channel joints, curved channel joints with sandwich features, and finally joints designed specifically for cross tensile testing. Mechanical testing was used to determine joint performance. Ultimate load at failure and observed failure mechanisms were used to guide the CF-Al joint design process from the initial three layer joints to the curved channel joints with CF sandwich features.

The purpose of using UAM technology to create CF-Al joints is to develop a joint whose performance is superior to adhesive joining in both profile and strength. UAM CF-Al joints can be made essentially flush, meaning that there is no overlapping as there is with adhesive lap joints. Depending on the application, this flush feature could be an important advantage of UAM CF-Al joints. This chapter has discussed UAM

CF-Al joint development from a strength standpoint. Most of the efforts discussed thus far have been focused on increasing joint strength from build to build using mechanical tensile testing and failure analysis to direct subsequent joint designs. The three layer - straight channel CF-Al joint was compared to an equivalently sized adhesive joint and was shown to be superior in strength and ductility. Chapter 4 will discuss tensile and cross tensile adhesive joint testing. The results from these tests will then be compared to results from tensile and cross tensile testing discussed in this chapter.

Chapter 4: ADHESIVE LAP JOINT BENCHMARKING

Benchmarking UAM CF-Al joints against the existing state-of-the-art jointing techniques is an important evaluation step to discern if UAM CF-Al joint provide improved performance. This was accomplished by creating four single lap adhesive tensile and cross tensile joints. The materials and geometry of these joints were the same as the UAM CF-Al joints which used sandwich features discussed in Chapter 3 for the most applicable comparison possible.

4.1 Adhesive Joint Construction

UAM welded 6061-H18 aluminum stock was used to create the metal portions of the joints. Nine-ply CFRP was created in house out of bidirectional woven CF fabric with HexTow AS4C 4000 3K tows. The epoxy used for the layup was Fibre Glast System 2000. Vacuum bagging was used with an exterior peel-ply layer to insure a uniform composite with no air voids. Once the bulk aluminum and CFRP materials were created, they were cut to size as needed to create the tensile and cross tensile CF-Al single lap adhesive joints.

The adhesive used was LORD Fusor 147/148 Plastic Bonding Adhesive. This is a two part adhesive designed for automotive repair of metal to plastic parts. The adhesive instructions were followed including surface preparation steps. The aluminum parts were cleaned, scuff sanded, then primed with Eastwood two part epoxy primer. After the primer had cured, the surfaces were scuff sanded once again and cleaned off with a lint free cloth. The CFRP parts were cleaned with acetone, scuff sanded, then wiped clean with a lint free rag.

The LORD Fusor 147/148 adhesive was applied to both sides of the joints with a two part adhesive mixing gun. The two parts were then pushed together and moved from side to side to insure excellent glue dispersion throughout the joint. Once the joints were all put together, weights were used to clamp the pieces together, shown in Figure 4.1(f). Excess glue was allowed to squeeze out the edges of the joints. One of each adhesive tensile and cross tensile specimens are shown in Figure 4.2. Spacers were added to either end of the tensile specimens to prevent bending during testing, pictured in Figure 4.2(c).

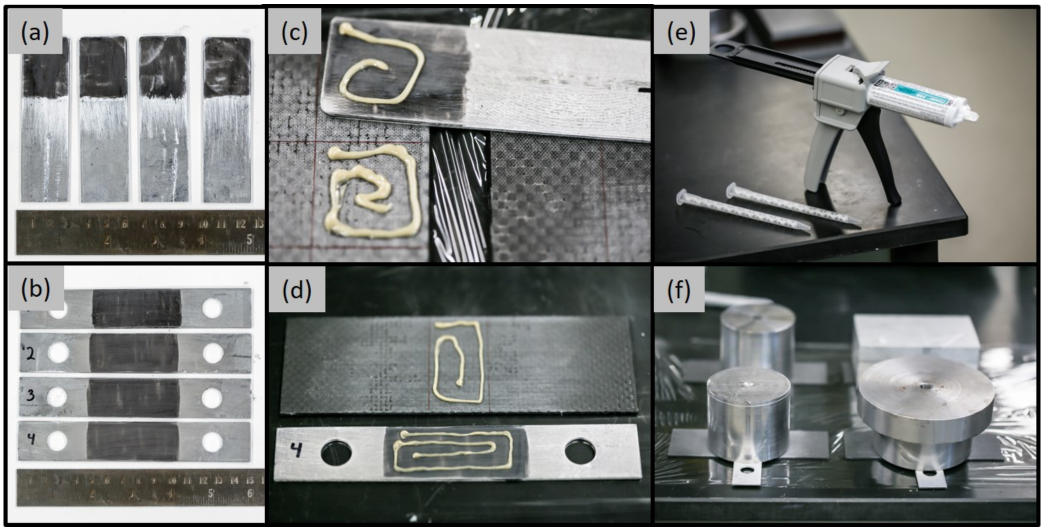

Figure 4.1: Adhesive joint assembly process. (a) Prepared aluminum tensile specimen parts, (b) prepared aluminum cross tensile specimen parts, (c) Glueing a tensile specimen, (d) Glueing a cross tensile specimen, (e) two part adhesive applicator gun with mixing tips, (f) Clamping with weights.

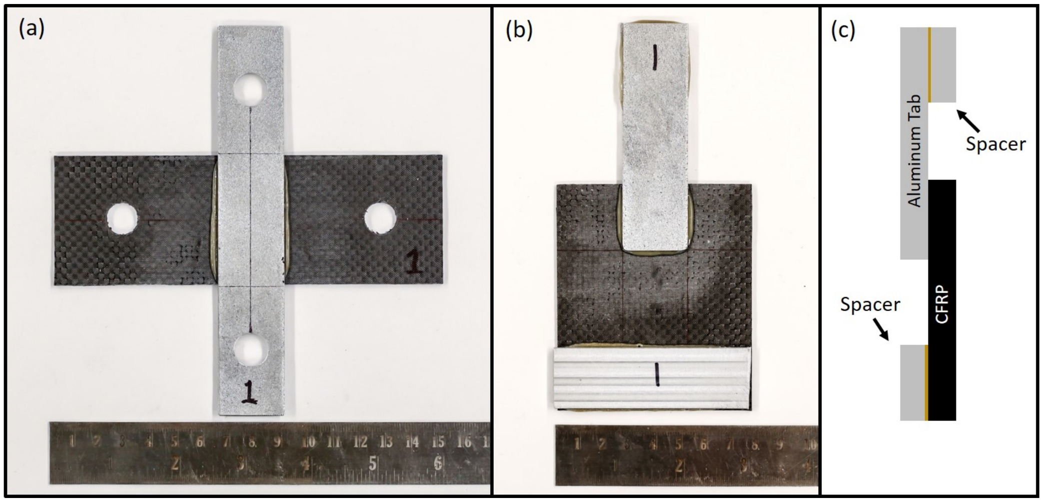

Figure 4.2: Completed adhesive joints. (a) Adhesive cross tensile joint. (b) Adhesive tensile joint. (c) Side profile of adhesive tensile joint. The specimen thickness is exaggerated for clarity.

4.2 Adhesive Joint Testing

4.2.1 Tensile Specimens

Tensile testing was completed using the same load frame and data acquisition system as described in Section 3.4.2. Once again, DIC was used to provide accurate displacement data throughout the testing. The results showed substantial variability between the specimens in joint stiffness and maximum load at failure. This could be from a variety of factors, but a likely cause is variation in the adhesive thickness used to join the aluminum and CFRP components. The load vs. displacement curves of the tensile tests are shown in Figure 4.3.

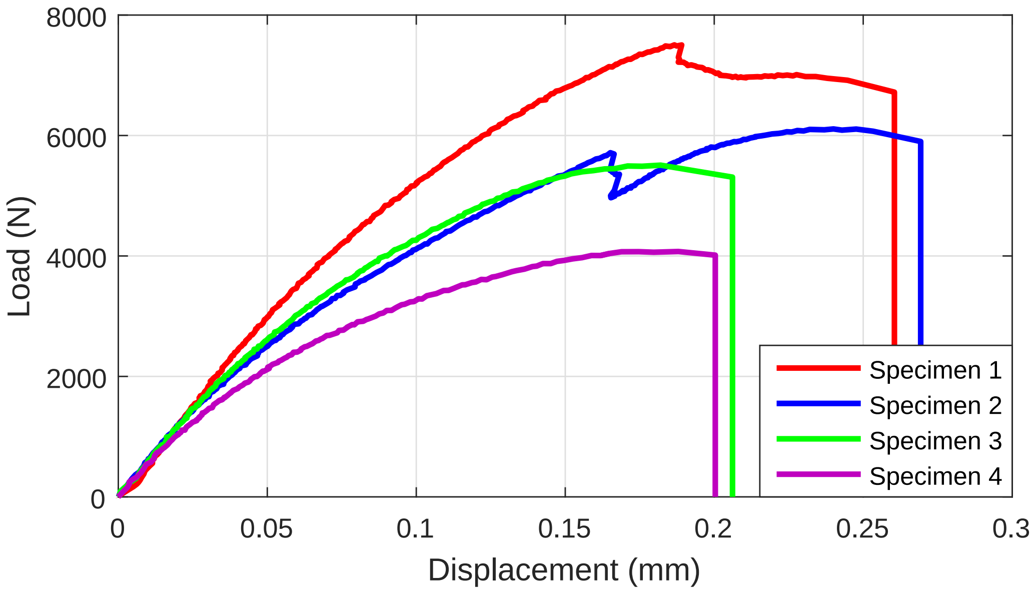

Figure 4.3: Load vs. displacement curves taken during the adhesive tensile testing.

In the first two specimens, the initial damage occurred before catastrophic failure. The adhesive used has excellent toughness properties making interfacial crack propagation less abrupt than would be the case with epoxy. For the third and fourth specimens, the load eventually plateaued and began to decrease before failure occurred. The failure classifications for the first two joints were a mixture of adhesive and cohesive, with the adhesive failure consisting of the adhesive separating from the epoxy primer. The third and fourth specimens exhibited solely adhesive failure. The average peak load for the adhesive tensile specimens was 5799 N with a standard deviation of 1422 N. Images of the failed joints are shown in Figure 4.4.

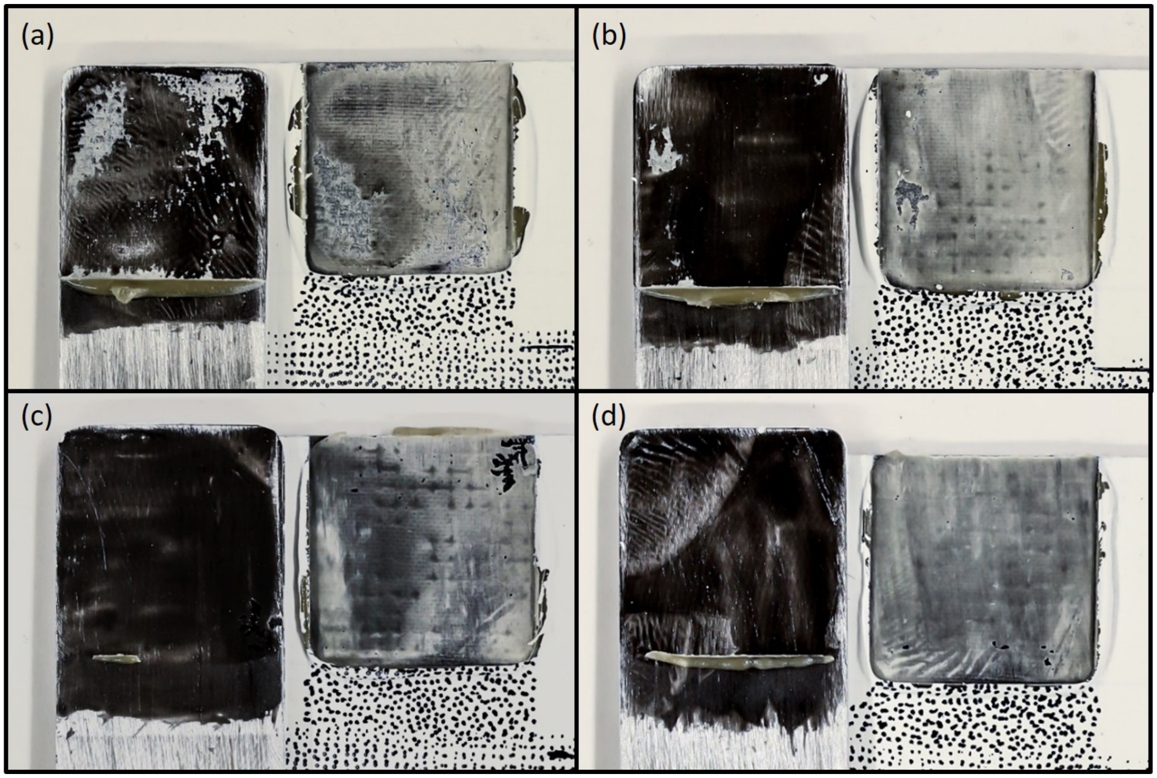

Figure 4.4: Adhesive tensile joint failure classification. (a) Specimen 1: mix of adhesive and cohesive failure. (b) Specimen 2: Adhesive failure with a small amount of cohesive failure. (c) Specimen 3: adhesive failure. (d) Specimen 4: adhesive failure.

4.2.2 Cross Tensile Specimens

The cross tensile testing of the adhesive CF-Al joints was performed in the same manner as the testing described in Section 3.5.2. The adhesive strength in the cross tensile loading condition was particularly poor. This is primarily due to adhesive joining's poor peel strength. The failure classification for each of the cross tensile specimens was adhesive failure between the epoxy primer and the adhesive. One interesting observation was the dual peak failure in the fourth specimen. This is telling of the adhesive's excellent toughness. Data from the second specimen was not recorded due failure from user error during the clamping process into the cross tensile fixture. The average peak load during these cross tensile tests was 1680 N with a standard deviation of 265 N. Load vs. displacement curves from the tests are shown in Figure 4.5.

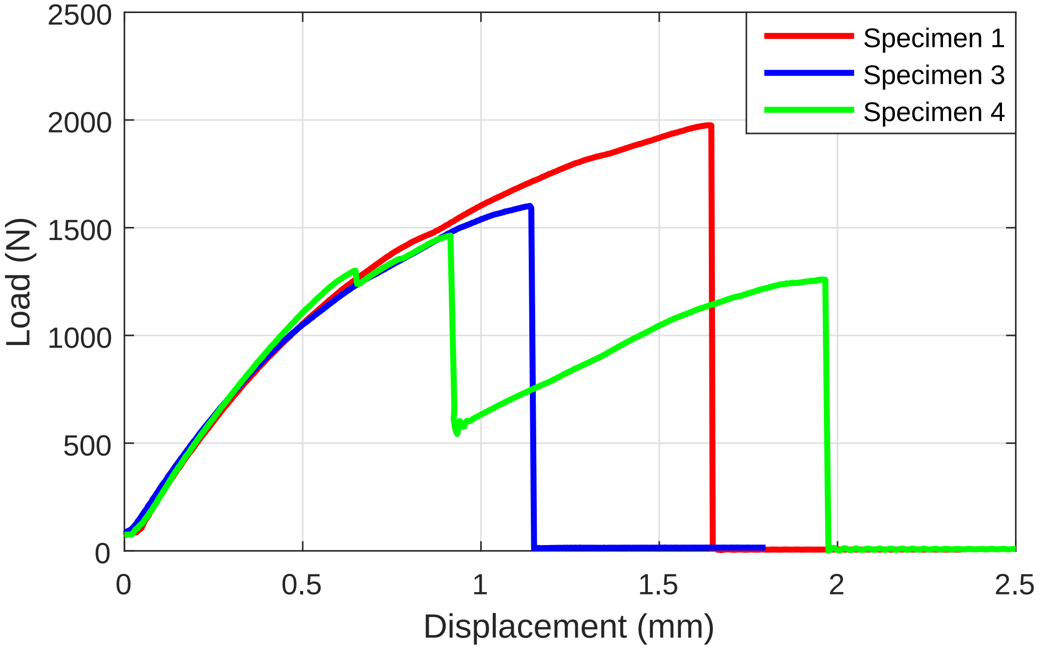

Figure 4.5: Load vs. displacement curves of the adhesive cross tensile joint testing.

4.3 Comparison: Adhesive Joints vs. UAM Joints

The single lap adhesive CF-Al joint tensile and cross tensile testing provided benchmarking information to compare with the UAM built CF-Al specimens from Chapter 3. The UAM built specimens that were compared were the groups of four tensile and four cross tensile joints which included the CF sandwich features. The bar graph in Figure 4.6 compares the peak load from the testing results. In both tensile and cross tensile categories, the UAM joints showed a substancial superiority in strength compared to their adhesive equivalents. The adhesive CF-Al joint tensile specimens showed greatest variation in peak load. This indicates that the adhesive joint manufacturing process is sensitive to construction parameters such as adhesive thickness.

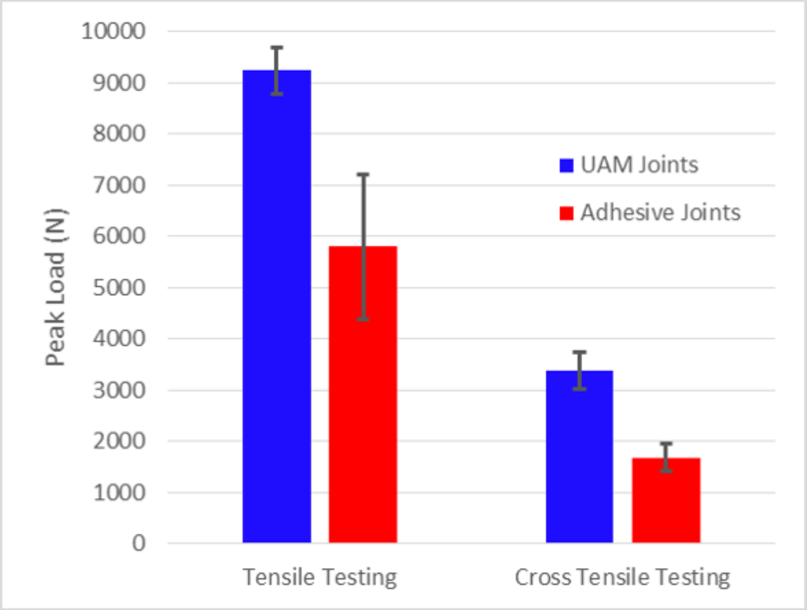

Figure 4.6: UAM and adhesive CF-Al joints compared for tensile and cross tensile testing cases.

One important difference between the UAM and adhesive joint testing results is in the failure modes present. The adhesive joints all failed by adhesive failure or a adhesive/cohesive combination. The UAM joints also underwent adhesive failure between the epoxy and aluminum, but additionally failed within the aluminum because of reduced cross sectional area from the embedded CF tows. The UAM joints were designed so that more than just adhesive failure is necessary to separate the two bulk components: the CFRP and the aluminum. Either the aluminum or the CF must break since the materials are interlocked with each other mechanically.

To summarize the comparison, the UAM CF-Al joints were shown to have greater strength than adhesive single lap joints. This benchmarking was an important step in UAM CF-Al joint research because it validates that the joining technique can compete with the current state-of-the-art joining methods in strength.

Chapter 5: UAM FOIL TEARING

5.1 Introduction

Since the earliest stages of embedding CF within aluminum, foil tearing has been a troublesome issue. Foil tearing is when the metal foil being welded tears, creating discontinuity in the welded foil. Foil tearing typically occurs when welding over surface substrate abnormalities, channels being the prime example. Foil tearing can be detrimental to the quality of a UAM produced part, particularly if the tearing occurs when welding over a channel, since the channel has already reduced the part cross sectional area in that region. Though there are exceptions, if foil tearing occurs throughout the build process of CF-Al joints, the construction is considered defective and must be scrapped.

Typically if foil tearing has occurred, it becomes difficult to weld additional foils over the defect without the cracking continuing through the subsequent layers. This generally means that once foil tearing has occurred, the structure being welded is not salvageable unless the defective region is machined away using the UAM center's subtractive capabilities. During CF-Al joint construction, machining off welded aluminum layers while avoiding damage to embedded CF tows followed by re-texturing the substrate surface can be very difficult to accomplish. For these reasons foil tearing must be alleviated in order to allow repeatable manufacturing of CF-Al joints.

The most common circumstance where foil tearing appears is when welding over a channel filled with CF which is oriented transverse to the welding direction. However, in some cases, foil tearing can also occur when the channels are oriented parallel to the welding direction. Figure 5.1 shows several foil tearing examples. The tearing is easy to pick out in these images, but often, foil tearing is more subtle, appearing as a hairline crack that does not always continue the whole way through the width of the foil.

5.2 Experimental Observations

Determining the root cause of foil tearing is an important step necessary for choosing UAM process parameters and build geometries which eliminate this manufacturing defect. Trial and error experimentation was used to understand factors which play into the foil tearing situation. This section focuses on a number of experiments and design/parameter modifications which build a case for what actually happens to cause the foil to tear. The factors that have the greatest effect on foil tearing are weld normal force, oscillation amplitude, and channel depth / amount of CF in the channel. During this trial and error process there were also a number of factors that did not greatly effect foil tearing. These are discussed in the following section.

5.2.1 Factors Not Substantially Affecting Foil Tearing

Stabilizing the UAM Normal Force

One hypothesis for the cause of foil tearing was UAM normal force instability. To investigate the weld downforce profile, the UAM diagnostics were setup to record the

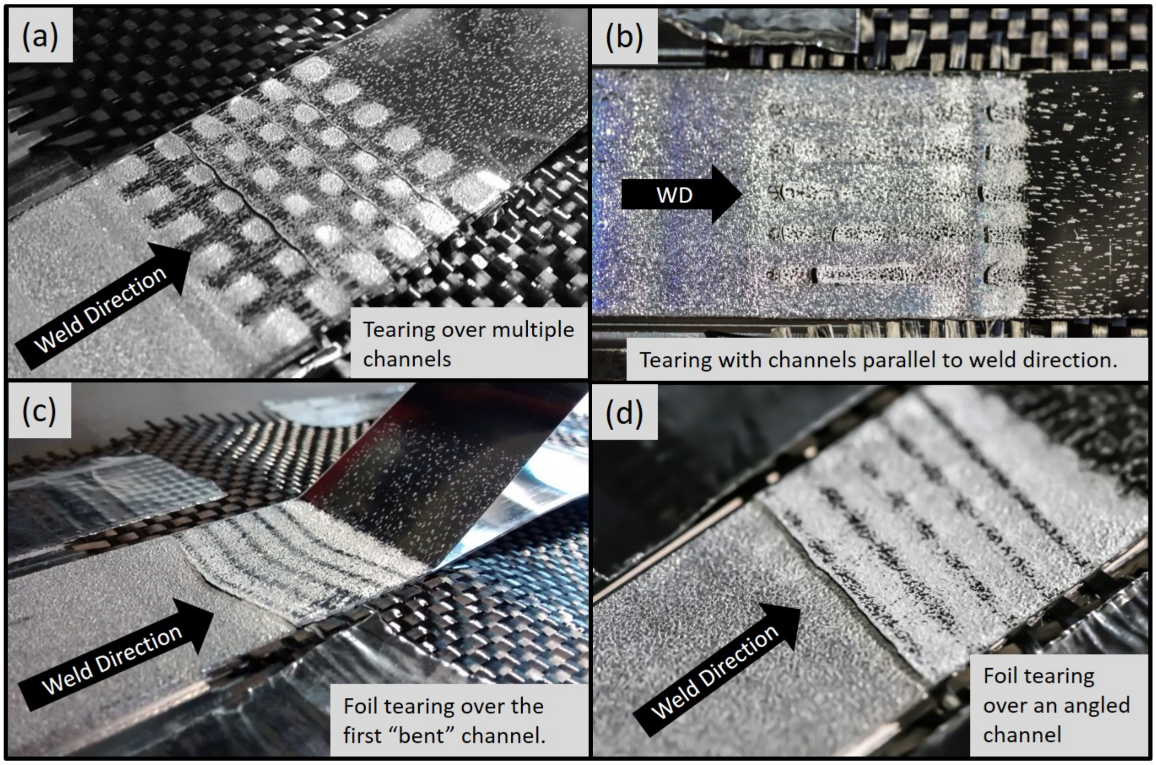
(a)
Weld Direction
Tearing over multiple channels
(b)
WD
Tearing with channels parallel to weld direction.
(c)
Weld Direction
Foil tearing over the first "bent" channel.
(d)
Weld Direction
Foil tearing over an angled channel

Figure 5.1: Foil tearing examples. (a) Multiple tear locations while welding over cross-hatch channels filled with CF tows. (b) Case of foil tearing where the channels run parallel to the welding direction. (c) Foil tearing over the first channel with a "bent" channel design. (d) Foil tearing over the first channel with a angled design.

force measured by the machine's load cell during welding operation. This data was retrieved from the machine and filtered to smooth out the uneven traces due to the 50 Hz sampling rate. After observing the force profile for the first time, it was apparent that there were normal force control stability issues.

The welding normal force profile before any machine modifications were made exhibited oscillating swings of around 1000 N about a nominal force value of 3000 N. The frequency of the oscillations was about 4 Hz. This suggests that the UAM normal force controller was overshooting its targeted load, in this case meaning that the controller gain needed to be reduced. The controller uses a control algorithm which is similar to PID with $\mathrm{C}_1\mathrm{x}, C_2\mathrm{x}^2$, and $\mathrm{C}_3\mathrm{x}^3$ terms. The gain term was reduced from $5x10^{-5}$ to $5x10^{-7}$ which resulted in a much improved normal force profile. Figure 5.2 shows the welding normal force profile for two welds from before and after the controller gain modification.

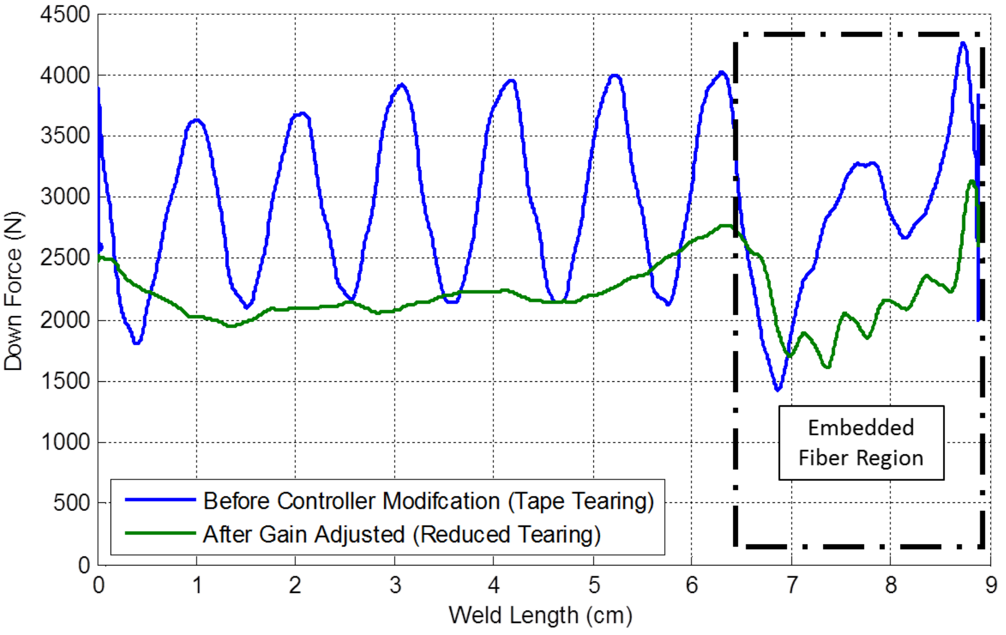

Figure 5.2: Normal force profile when welding a foil layer directly over cross-hatch channels before and after the controller gain adjustments.

Foil tearing continued to be an issue after the gain modification, though the severity of the tearing lessened slightly. This suggests that the massive swings in weld normal force were not the sole cause of the foil tearing issue. Since this normal force study was completed, it has been discovered that lowering the normal force greatly reduces tearing. This suggests that the reduced tearing experienced when the controller gain was adjusted was because of the reduced normal force over the embedded fiber region as seen in Figure 5.2. The normal force was reduced since the lower controller gain slowed the system's response to the lower substrate stiffness caused by the channels. This resulted in a normal force over the channels of about 2000 N even though the nominal force value was set to 3000 N.

Improving 6061-H18 Aluminum Foil Ductility

It has been known that 6061-H18 aluminum has poor mechanical properties for being a 6061 alloy. This is particularly true in the post welded condition. Knowing this, it was hypothesized that the foil tearing might be avoided by improving the aluminum foil ductility. A simple aging heat treatment was performed on a roll of 6061-H18 aluminum foil to accomplish this. The roll was put into an oven at 160 C° for 18 hours, then removed. Prior to the heat treating, several short lengths of foil were cut off of the roll for tensile testing. More lengths of foil were cut off from the roll after the heat treating. Both sets of UAM foil were pulled to failure on a small Test Resources load frame. Stress vs. strain from these tests are shown in Figure 5.3.

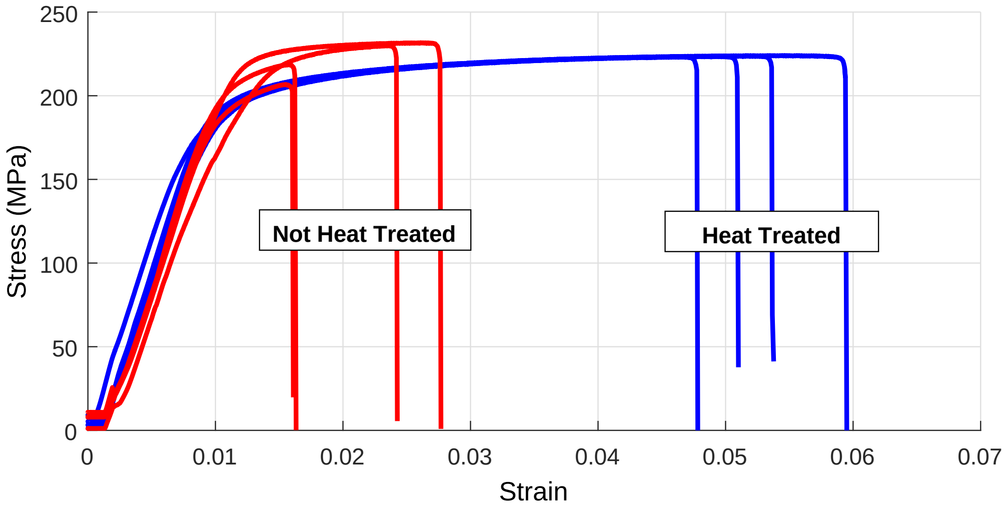

Figure 5.3: Stress vs. strain curves for 6061-H18 aluminum tape, before and after 18 hour aging at 160 $C°$.

The results from the foil tensile test showed that the ultimate strain increased to more than 200% of the value after the aging process. The roll of foil that had been heat treated was then used to weld over the same type of aluminum substrate that had exhibited tearing with the non-heat treated foil. However, no tearing reduction was observed. This suggests that whatever mechanism causes the foil tearing is not closely tied to the material ultimate strain. Though it is possible that a much more ductile material would eliminate the foil tearing.

Creating Even Substrate Compliance in the Channel Region

Related to the hypothesis that sudden changes in the welding normal force promotes foil tearing is the hypothesis that sudden changes in the substrate compliance also affects foil tearing. As seen in the adjusted gain normal force profile in Figure 5.2, the normal force fluctuates as the sonotrode welded over each of the channels in the embedded fiber region. To determine whether fluctuations in substrate compliance experienced by the sonotrode cause foil tearing, two channel designs were used which create even substrate compliance over the channel region. One of the designs used angled channels with the right side channel inlet directly across from the previous channel outlet on the left side. The other design featured bent channels which start at an angle, make a turn at the center of the structure, and angle back as the channel approaches the other side of the build. This design does not create a completely even substrate compliance, but was certainly an improvement over straight horizontal channels. After welding several specimens using each of these channel designs, it was found that foil tearing was not reduced, meaning that uneven substrate compliance is not to blame for foil tearing. Images of these transverse channel designs are shown in Figure 5.4.

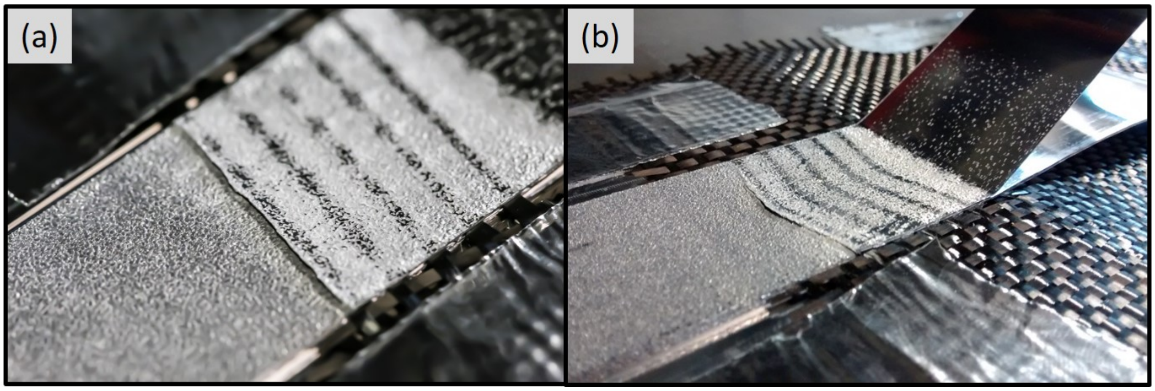

Figure 5.4: Examples of foil tearing on builds with channel arrangements specifically designed for even substrate compliance over the embedded fiber region. (a) Foil tearing persists with angled channels. (b) Foil tearing at the front channel of a build utilizing the "bent" channel design to minimize substrate compliance over the channel region.

5.2.2 Factors Affecting Foil Tearing

No rigorous design of experiment study was completed to determine factors that are statistically relevant with respect to foil tearing. However, many hours of welding CF-Al specimens and making process modifications based on observed outcomes have provided valuable insight into this problem. The following sections explain how the parameters of channel depth, normal force, and oscillation amplitude play a roll in foil tearing occurrence. A predicted foil tearing root cause was made based off of these factors and used to formulate an FEA model.

Channel Depth

While experimental observations have shown that multiple factors have a roll in causing foil tearing, the most influential factor is channel depth. This was first distinctly observed when a series of channels shown in Figure 5.5(a) were cut with dimensions 1.8 mm x 0.28 mm in width and depth respectively. These channels were then welded over with a standard set of welding parameters. No foil tearing was observed, shown in Figure 5.5(b). Next, another set of identical channels were cut and CF tows were placed into the channels. when the CF was embedded, foil tearing was observed in several locations as seen in Figure 5.5(c).

Many other experimental observations have supported this fact, that tearing is not likely to occur without CF tows in the channels. Furthermore, it has been observed that the when CF are in the channels, the channel depth is an extremely important factor affecting foil tearing. For example, in a straight, transverse channel housing two HexTow AS4C 4000 3K tows, given proper welding parameters and a channel width of 1.59 mm, foil tearing will not occur if the channel depth is 0.28 mm. However, if the channel depth is decreased to 0.23 mm which is deeper than the packed CF height, tearing will occur. These observations suggest that the amount of support given from the CF to the foil being welded plays a large roll in the foil tearing failure mechanism.

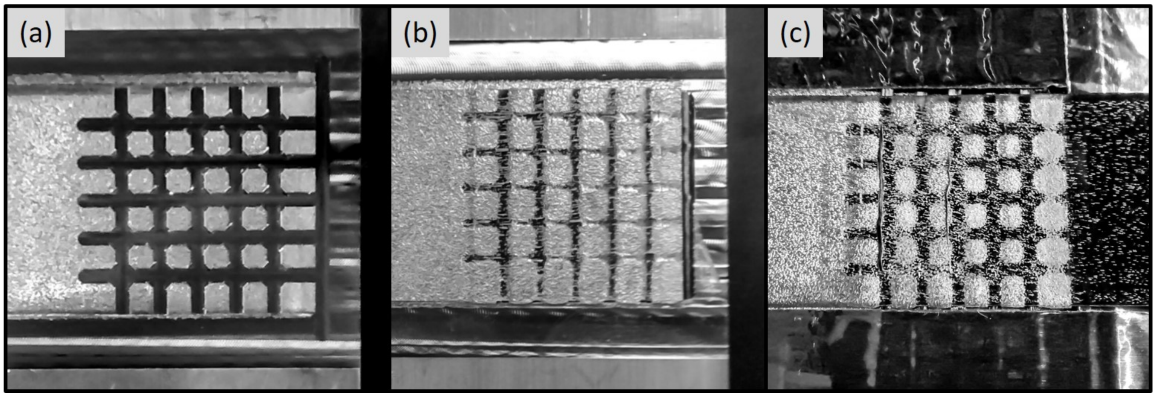

Figure 5.5: The effect of having CF tows in the channels. (a) Channels are cut at 1.8 mm x 0.28 mm in width and depth respectively. (b) Layer of aluminum foil is welded over the unfilled channels. This resulted in no foil tearing. (c) Layer of foil is welded over channels filled with CF tows. Several foil tears are produced.

Normal Force

The other key factor influencing foil tearing phenomena is the welding normal force. As already mentioned and shown in Figure 5.2, lowering the normal force has been correlated with reduced foil tearing. For a concrete example, during cross tension CF-Al joint construction discussed in Chapter 3, a normal force of 4000 N was used for welding the bulk material layers of the cross tension specimens. However, if a 4000 N normal force was used for the layer welded over the straight horizontal channels, foil tearing would occur. Instead, when welding directly over the horizontal channels, a normal force of 2000 N was used and no foil tearing was observed. These results strongly suggest that the normal force is a key factor influencing foil tearing.

Other Factors

Other factors that may play into foil tearing in a less direct way include, channel width, oscillation amplitude, and weld speed. Experimental observations suggest that foil tearing is more likely to occur when welding over wide channels than narrow ones. From an experimental standpoint, this has little influence on tearing mitigation since narrow channels are also more desirable from a structural integrity standpoint. Oscillation amplitude certainly factors into foil tearing as this parameter greatly affects the energy input into a weld. However, a formal DOE study using 6061-H18 aluminum has shown that reducing the oscillation amplitude has a large negative effect on inter-laminate bonding strength [39]. For this reason, reducing the oscillation amplitude substantially is not advised. Finally, weld speed also plays a roll into foil tearing. Experimental observations have shown that reducing the weld speed increases the amount of foil tearing. This makes sense since reducing the weld speed increases the energy going into the weld which means more energy is available to tear the foil.

5.2.3 Predicted Root Cause

Given the experimental observations described in the previous section, a root cause of foil tearing was predicted. The predicted root cause says that the foil is welded securely up to the leading edge of the channel housing CF tows. Once the sonotrode moves to weld directly on top of the channel, the CF filled channel provides enough support to allow the sonotrode to grip the foil effectively. At this point, the foil is moving along with the sonotrode substantially since there is high friction between the sonotrode and foil, and low friction between the CF and foil due to carbon fiber's graphite nature. When the foil is pulled from side to side by the sonotrode while the welded foil is rigidly bonded to the base layers, there is a region of extreme shear stress in the foil which is unsupported between the front edge of the channel and the sonotrode location. This is the location where foil tearing has been experimentally observed and is predicted by the hypothesis stated above. The predicted foil tearing root cause is illustrated by the schematic in Figure 5.6.

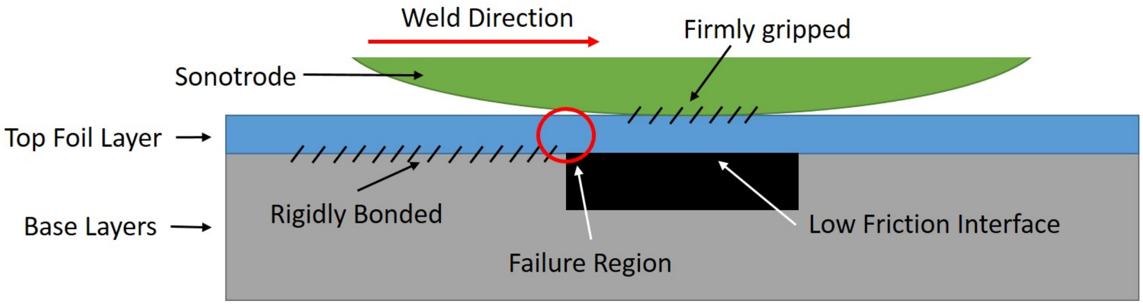
Weld Direction
Firmly gripped
Sonotrode
Top Foil Layer
Base Layers
Rigidly Bonded
Low Friction Interface
Failure Region

Figure 5.6: Schematic showing the predicted root cause of foil tearing.

5.3 Finite Element Analysis Model

To determine whether the predicted foil tearing root cause is plausible or not, a finite element analysis (FEA) model was developed. The goal of the model was to determine if the shear stresses in the failure region are beyond the ultimate shear strength of the foil.

5.3.1 Assumptions

While setting up the FEA model, a number of assumptions must be made to determine the appropriate boundary conditions to the problem. One of the most foundational assumptions of the model is that this problem can be solved for a static loading case even though in reality, the sonotrode is moving the foil back and forth at 20 kHz. This assumption is necessary, but excludes factors such as ultrasonic lubrication and material heating.

The chosen value of friction coefficient was estimated using an energy balance and measured values of normal force and average electric power. Measurements while welding over channels have shown the weld normal force to be 2000 N for a nominal force machine input of 3000 N when welding in the channel region. This reduction in normal force is due to the added substrate compliance in the channel region. The electric power ($P_{e,avg}$) used while welding over the same channel region was 1800 W. Equation 5.1 can then be used to estimate the welding shear force (F_s) [4].

$$F_s = \frac{P_{e,avg} e}{\delta \pi \omega} \tag{5.1}$$

Assuming a welder efficiency (e) of 80% [4], sonotrode amplitude (δ) of 16 μm, and operating frequency (ω) of 20 kHz, the estimated shear force is 1400 N. Knowing the shear force as well as the measured normal force (F_n) of 2000 N, the coefficient of friction upper bound can be estimated as 0.7 by Equation 5.2.

$$\mu = \frac{F_s}{F_n} \tag{5.2}$$

This friction coefficient estimate is considered the upper bound because experimental measurements show that sonotrode to foil relative velocities vary greatly within the length of a typical weld. The coefficient of friction is likely the cause of this fluctuation, meaning that while coefficient values as high as 0.7 are possible, much lower friction coefficient values between the sonotrode and foil may be at play during the same weld. For the purposes of this analysis two friction cases were chosen with friction coefficient values of 0.5 and 0.2.

Another assumption dealt with reducing the size of the model for computational efficiency. To accomplish this, a section 1/5 of the sonotrode, base, and foil width was used. The only input difference in the problem with this reduced width is that the normal force input must be divided by a factor of 5 to arrive at the correct contact pressure between the sonotrode and foil. The solid model of the part geometries used is shown in Figure 5.7.

The base of the welded base layer structure was assumed an encastre condition (no displacement or rotation). In reality, the baseplate and vacuum chuck supporting the welded foils have a sizable amount of compliance. While this amount of base compliance is not negligible, it was accounted for by reducing the sonotrode displacement input. Another assumption made was that the foil welded up to the front edge of the channel was rigidly bonded to the base layers. This was done in the form of a tie constraint.

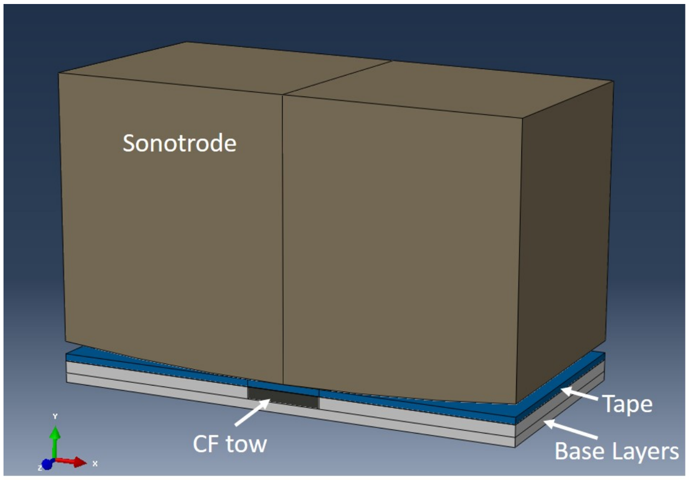

Figure 5.7: Solid model of the part assembly used in the FEA model

5.3.2 Inputs

Material Properties

The aluminum material properties used in the model were based off of in house material characterization. Figure 5.8 shows actual stress vs. strain data and a simplified curve with flat plasticity which was used in the model. The material properties used for the steel sonotrode were assumed standard annealed 4130 steel properties. The elastic modulus for the carbon fiber in the channel was assumed as 50 GPa. Unfortunately it would be difficult to accurately estimate what the packing modulus of dry CF tows actual is. The value of 50 GPa was chosen because it is slightly lower than the modulus of aluminum. A lower value could have been chosen, but the model is designed to present a worst case scenario of the problem. Choosing the higher modulus for the CF simulates the case when the channel is full of CF, which is the case where the worst foil tearing has been observed. For simplicity, the CF was given isotropic properties. The material properties used in the model are summarized in Table 5.1.

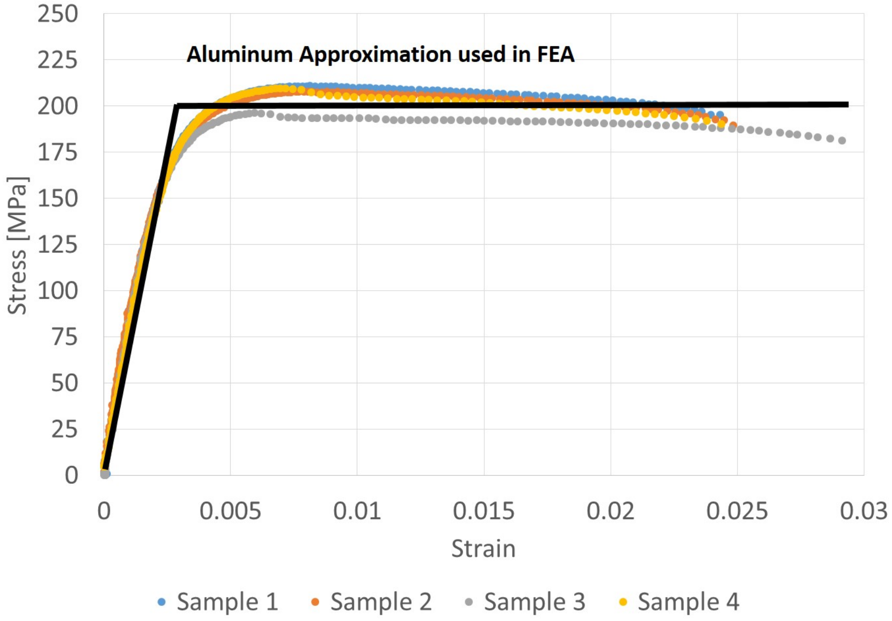

Figure 5.8: Stress vs. strain approximation used in the FEA model overlaid onto experimental stress vs. strain curves. The experimental testing was completed on 6061-H18 aluminum samples post UAM welding.

Table 5.1: Material properties used in the FEA model.

Material	**Elastic Modulus**	**Poisson's Ratio**	**Yield Stress**
Carbon Fiber	50 GPa	0.3	NA
Aluminum Base Layers	74 GPa	0.33	200 MPa
Aluminum Foil Layer	74 GPa	0.33	200 MPa
Steel Sonotrode	205 GPa	0.29	435 MPa

Boundary Conditions and Loads

The boundary conditions and loads used for the FEA model include an encastre condition on the bottom of the base tape layer structure, normal force from the sonotrode, and displacement from the sonotrode. The encastre condition prevents any movement (displacement or rotation) of the bottom of the base structure. The normal force used was input as a pressure to the upper surface of the sonotrode. The value of pressure used corresponds to 2000 N for normal force over the full width of a 25.4 mm wide foil.

The typical sonotrode displacement used during welding has an amplitude of 16 μm (32 μm peak-to-peak). In reality, however, this welding amplitude usually decreases by about 10 % during welding because of the load imparted on the sonotrode from the workpiece [4]. Additionally, as the weld substrate height increases, the relative motion between the sonotrode and the substrate decreases [4]. It is common for the relative velocity between the sonotrode and substrate to be half of the sonotrode velocity [13]. Because of these factors, a relative displacement between the sonotrode and base substrate of 8 μm was chosen. Figure 5.9 shows how the boundary conditions were applied to the model.

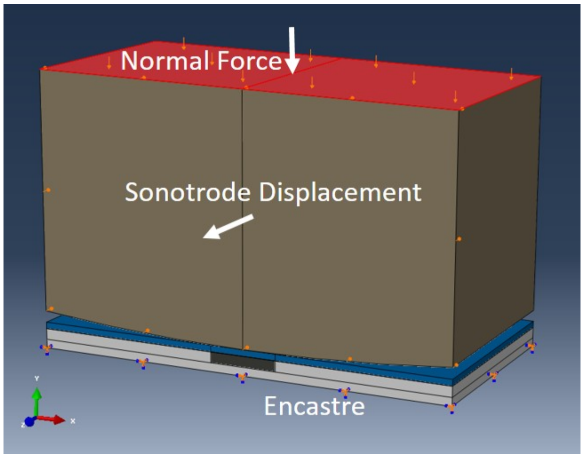

Figure 5.9: Boundary conditions applied to the FEA model.

Surface Interactions and Constraints

Any surfaces that were assumed rigidly welded were given tie constraints in the FEA model. These surface pairs include the base structure to top foil in the welded region. Another surface pair that was given a rigid tie was the bottom of the channel to the bottom of the CF.

Contact interactions include the following:

1. The non-welded base to top foil layer
    - Assumes frictionless tangential behavior
    - Assumes "Hard" contact normal behavior using the penalty constraint enforcement method with a stiffness scale factor of 0.1.
2. The carbon fiber to top foil layer. Assumes the same interaction properties as described in 1.
3. The sonotrode to top foil layer

- Assumes a penalty friction formulation for tangential behavior with a friction coefficient of 0.2 and 0.5 for different scenarios described later.
- Assumes "Hard" contact normal behavior using the penalty constraint enforcement with a non-linear contact stiffness.

Element Type and Mesh Sizing

The elements used for each part in the model were solid 20-node 3-D bricks. Additional resolution was achieved by not using reduced integration. The size of the mesh size was approximately 0.4 mm. This mesh is only slightly smaller than the width of the region of interest at the sonotrode/foil contact region. However, a refinement study was completed which showed similar FEA results with even larger mesh sizes. Because of this, the chosen mesh size of 0.4 mm was deemed acceptable.

5.4 FEA Model Results

Before a discussion of the FEA model results, a short word on foil tearing failure mechanisms should be entertained. The UAM process uses high frequency oscillations of the sonotrode coupled with a normal force imparted on the foil being welded to scrub the foil against a fixed metal substrate. The combination of pressure and substrate/foil relative motion causes high shearing forces at the substrate/foil interface which eventually leads to metallurgical bonding. The point is that this FEA model predicts material yielding in a number of locations. Yielding should be expected within the welding zone as it is necessary for bonding. However, foil tearing is a phenomenon that occurs when the material undergoes high shear stresses in regions that are unsupported by the sonotrode. In fact, based off the predicted failure root cause pictured in Figure 5.6, the stress state that should be telling of failure in the foil is S_{13} which is depicted in Figure 5.10. This is an important observation because if one simply considers Von Mises stress as failure criterion, failure would be predicted in areas of material yielding due to compressive and shearing forces within the weld zone which are requirements for the UAM process. Using S_{13} as the critical stress state will help avoid confusion when viewing the FEA results.

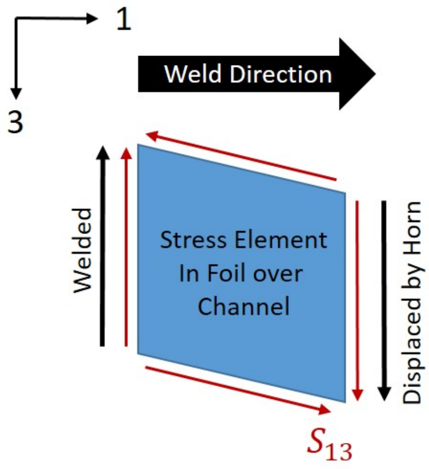

Figure 5.10: S_{13} stress state which is an indicator of foil tearing failure.

The Von Mises stress can be related to individual stress components by the Von Mises stress definition, shown in Equation 5.3 [12].

$$S_{vm} = \sqrt{\frac{(S_{11} - S_{22})^2 + (S_{22} - S_{33})^2 + (S_{33} - S_{11})^2 + 6(S_{12}^2 + S_{23}^2 + S_{13}^2)}{2}} \tag{5.3}$$

In a scenario where the shear stress, S_{13}, is the only stress component, the Von Mises equation reduces to a simple expression shown in Equation 5.4. By this equation it is now possible to predict failure based solely on the S_{13} stress component. In the case of post welded 6061-H18 aluminum, the Mises failure stress is approximately 200 MPa, this corresponds to an S_{13} component of 115 MPa.

$$S_{vm} = \sqrt{3} S_{13} \tag{5.4}$$

5.4.1 Results at the Center and End of Channel Locations using Standard Assumptions

Two primary sonotrode locations were considered for the FEA analysis. Initially five sonotrode location cases were analyzed: before the sonotrode reached the channel, at the channel front edge, in the middle of the channel, at the end of the channel, and when the sonotrode is past the channel. The two locations showing the most relevant information were the center of channel and end of channel sonotrode locations. These are the locations that are discussed.

The FEA results from the two locations with sonotrode to foil friction coefficients of both 0.5 and 0.2 are shown in Figure 5.11. For each location, the two friction cases were run in the model for worst and best case estimations. For the end of channel position with high friction case, yielding in the foil was predicted with the S_{13} stress was over 115 MPa. However, for the end of channel position case with reduced friction, yielding was not predicted. This shows the significance of the friction coefficient and how its value can affect the failure outcome.

The FEA results for the sonotrode location over the center of the channel predicted yielding in the foil material for both cases of friction coefficient, at 0.5 and 0.2. The case with the higher friction coefficient showed more severe yielding throughout the foil at the front edge of the channel. The case with the lower friction coefficient predicted a smaller region of failure across the width of the foil, though yielding was still predicted. Since these cases in the middle of the channel position showed more extreme stresses than the end of channel position cases, the middle of the channel position will be used for special FEA cases discussed in the rest of this Chapter.

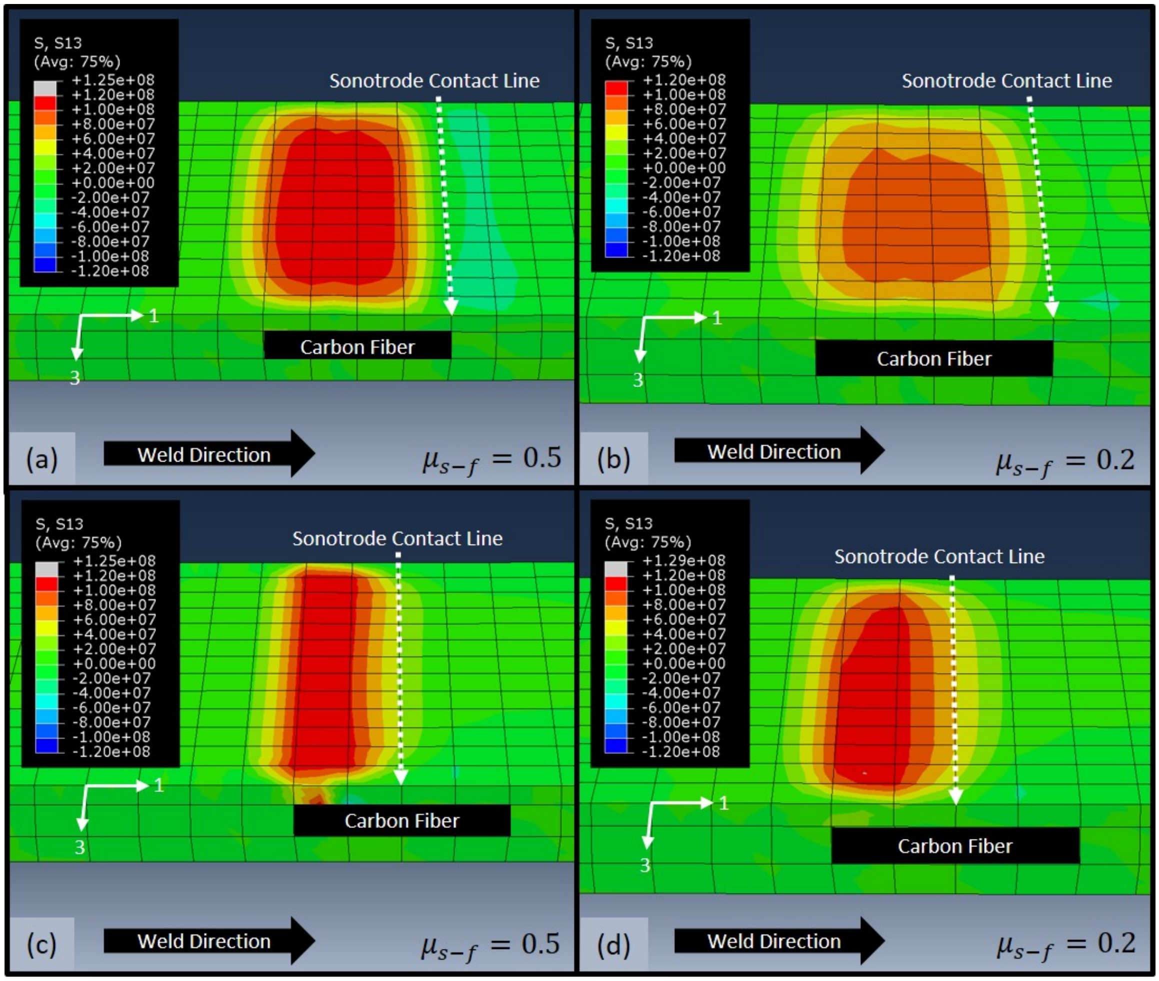
S, S13
(Avg: 75%)
+1.25e+08
+1.20e+08
+1.00e+08
+8.00e+07
+6.00e+07
+4.00e+07
+2.00e+07
+0.00e+00
-2.00e+07
-4.00e+07
-6.00e+07
-8.00e+07
-1.00e+08
-1.20e+08
Sonotrode Contact Line
1
3
Carbon Fiber
(a)
Weld Direction
$\mu_{s-f} = 0.5$
S, S13
(Avg: 75%)
+1.20e+08
+1.00e+08
+8.00e+07
+6.00e+07
+4.00e+07
+2.00e+07
+0.00e+00
-2.00e+07
-4.00e+07
-6.00e+07
-8.00e+07
-1.00e+08
-1.20e+08
Sonotrode Contact Line
1
3
Carbon Fiber
(b)
Weld Direction
$\mu_{s-f} = 0.2$
S, S13
(Avg: 75%)
+1.25e+08
+1.20e+08
+1.00e+08
+8.00e+07
+6.00e+07
+4.00e+07
+2.00e+07
+0.00e+00
-2.00e+07
-4.00e+07
-6.00e+07
-8.00e+07
-1.00e+08
-1.20e+08
Sonotrode Contact Line
1
3
Carbon Fiber
(c)
Weld Direction
$\mu_{s-f} = 0.5$
S, S13
(Avg: 75%)
+1.29e+08
+1.20e+08
+1.00e+08
+8.00e+07
+6.00e+07
+4.00e+07
+2.00e+07
+0.00e+00
-2.00e+07
-4.00e+07
-6.00e+07
-8.00e+07
-1.00e+08
-1.20e+08
Sonotrode Contact Line
1
3
Carbon Fiber
(d)
Weld Direction
$\mu_{s-f} = 0.2$

Figure 5.11: FEA S_{13} stress results at the middle and end of channel positions. Cases for sonotrode to foil friction coefficients of 0.5 and 0.2 are shown. The dark red color indicates yielding. (a) End of channel position with friction coefficient of 0.5. Yielding predicted. (b) End of channel position with a friction coefficient of 0.2. No yielding is predicted. (c) Middle of channel position with a friction coefficient of 0.5. Yielding is predicted. (d) Middle of channel position with a friction coefficient of 0.2. Yielding is predicted.

An approximation of the FEA end of channel, high friction S_{13} result can be found easily by performing a simple stress analysis. Consider the section of foil over the channel. Let the edge of the foil at the beginning of the channel be fixed/welded. Assuming that the sonotrode/foil friction is sufficient to grip the foil without slip, let the foil at the end of the channel be displaced in the 3-direction by 8 μm. Knowing these boundary conditions, the channel width (1.59 mm), and the shear modulus of aluminum (24 GPa), the shear stress, S_{13}, can be determined assuming no plasticity or yielding by Equation 5.5 [12]. This FEA validation is shown graphically in Figure 5.12. Using Equation 5.5 and plugging in values for shear modulus, G, channel width, l, and sonotrode displacement, Δx, the predicted shear stress, S_{13}, is slightly over the material shear yield stress at 121 MPa.

This technique can also be used to predict how problematic foil tearing would be with other foil materials such as steel. For the case of annealed 4130 steel with a yield strength of 460 MPa and shear modulus of 80 GPa, the resulting shear stress for a end of channel foil displacement of 10 μm would be 533 MPa. Since the maximum shear stress in this position is greater than the material yield stress, foil tearing could occur. However, other factors such as friction and foil ductility cannot be considered using this simple approximation. For this reason, FEA and experimental testing are required to fully investigate foil tearing issues.

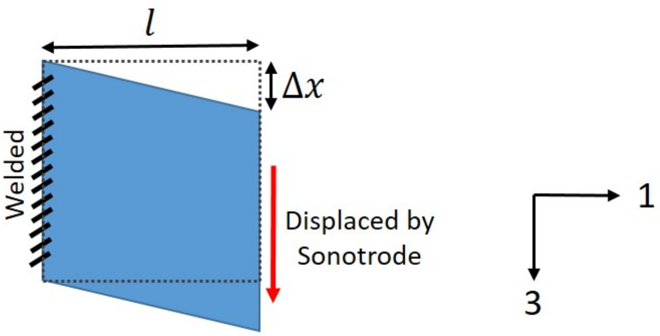

Figure 5.12: Schematic showing FEA validation technique.

$$S_{13} = \frac{G\Delta x}{l} \tag{5.5}$$

This technique was used to validate the FEA results, given the assumptions used. It can also be used to explain why the yielding in the middle of channel position cases were most severe. Since the force displacing the foil is closer to the front edge of the channel where the foil is welded, the distance, l, is reduced, thereby increasing the shear stress, S_{13}.

The FEA results seem to line up well with experimental observations in that foil tearing is predicted when the channels are packed with CF tows. However, experimental observations have also shown that increasing the channel depth to reduce CF packing can eliminate foil tearing issues. Removing this CF support from the channel results in the sonotrode skipping over the channel without applying a large normal force to grip it well. Unfortunately it isn't possible to measure this normal force value accurately since the UAM machine outputs record at only 50 Hz. To simulate this case via FEA, the center of channel position was used, the normal force was reduced to a value of 500 N, and the friction coefficient was kept at 0.5. The results do not predict failure, which agrees with the experimentally observed result. Figure 5.13 shows the S_{13} results for this case compared with the original, higher normal force case. A summary of the five different FEA cases discussed thus far are shown in Table 5.2.

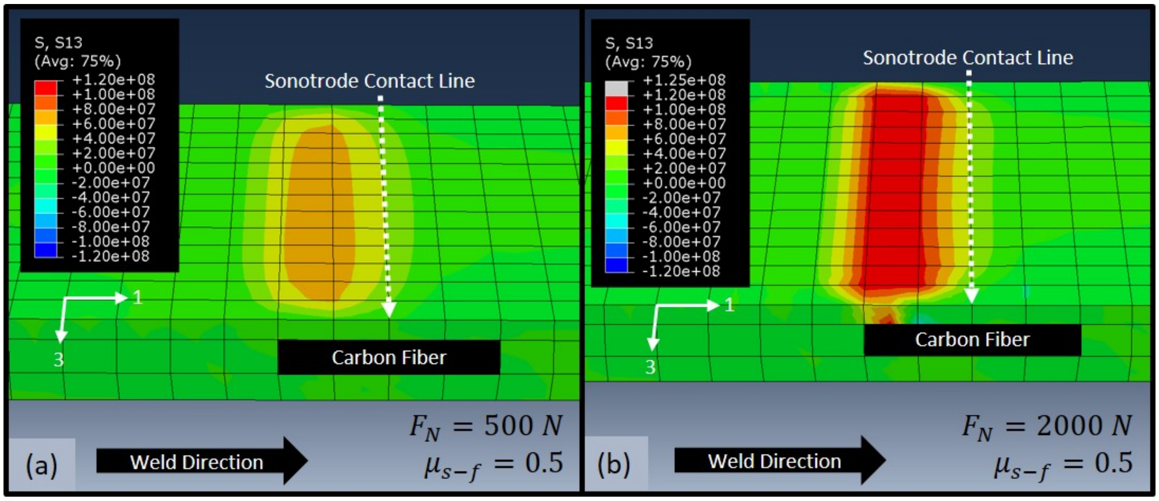

Figure 5.13: FEA S_{13} shear stress results at the center of channel position with reduced normal force (a) compared with the original simulation force case (b). Dark red indicates yielding.

Table 5.2: Summary of FEA results for cases with standard assumptions.

Position	**Normal Force**	**Friction Coefficient**	**Result**
End of Channel	2000 N	0.5	Foil Tearing Predicted
End of Channel	2000 N	0.2	No Tearing Predicted
Center of Channel	2000 N	0.5	Foil Tearing Predicted
Center of Channel	2000 N	0.2	Foil Tearing Predicted
Center of Channel	500 N	0.5	No Tearing Predicted

5.4.2 FEA Results for Three Special Cases

FEA simulations were also run for three special cases using different interactions and/or boundary conditions. Each of these cases uses the center of channel sonotrode location and a friction coefficient of 0.2. The sonotrode location was chosen because results from the previous section suggested that the center of channel location is the most critical with regard to foil tearing. The lower friction coefficient of 0.2 was chosen since the special cases discussed all deal with inducing sonotrode-foil slip to prevent yielding in the foil, so improvements in model performance are more obvious with the lower friction coefficient.

Special Case 1: Tacked Foil

The first special case assumes that during the welding process, the layer of foil welded over the channel housing CF was initially welded with very weak parameters, weak enough that foil tearing does not occur. After this initial tacking with weak parameters, a second welding pass is completed over the already tacked foil layer. The change made to the FEA model to represent this case is that the foil was assumed rigidly tied to the base layers in the region after the channel. Previously, this interaction was assumed frictionless tangential behavior and hard contact normal behavior.

The foil being tied to the base layers on both sides of the channel provided enough constraint to cause slipping between the sonotrode and foil which resulted in the much lower S_{13} shear stresses. In practice, this special case could be used to reduce foil tearing by first tack welding a foil layer with low weld parameters, followed by a more aggressive welding pass. However, using this technique will not necessarily eliminate tearing, as the effect of pre-tacking the foil was not promising when higher friction coefficients were used in the FEA. Figure 5.14 shows the S_{13} shear stress results from this FEA simulation compared with the original case from Section 5.4.1.

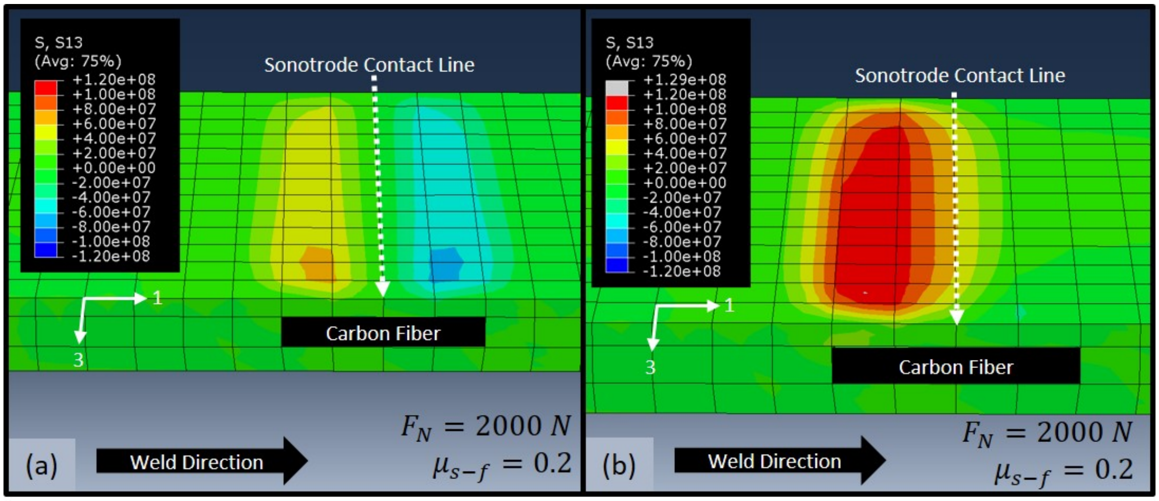

Figure 5.14: Special Case 1 FEA results and comparison. Dark red indicates yielding. (a) FEA results from securing the foil after the channel with a tie constraint. (b) The original FEA result with the foil/base layer interface given frictionless tangential properties.

Special Case 2: CF/Foil Interface Friction

The second special case assumes that the friction coefficient between the top of the CF and bottom of the aluminum foil is 0.5. The friction coefficient between the sonotrode and foil is lower at 0.2. In previous models, the interaction between the carbon fiber in the channel and the top foil layer was assumed frictionless tangential behavior. In reality, the coefficient of friction between the CF and top foil is very low since CF is made of graphite, which can act as a lubricant. However, if it would prove valuable to increase the friction at that interface, efforts to accomplish this could be explored.

Figure 5.15(a) presents the results for the FEA model with friction at the CF/foil interface. The results show very little S_{13} stresses compared to the original case without the increased friction at the CF/foil interface (Figure 5.15(b)). This suggests that a large amount of slip occurs between the sonotrode and foil. Judging from the results, it would seem that this technique could be pursued to alleviate foil tearing. However, this simulation used a friction coefficient at the CF/foil interface that was greater than the friction coefficient at the sonotrode/foil interface which would be difficult to achieve in practice. Other simulations which made the CF/foil interface friction coefficient equal to the sonotrode/foil friction coefficient predicted foil tearing.

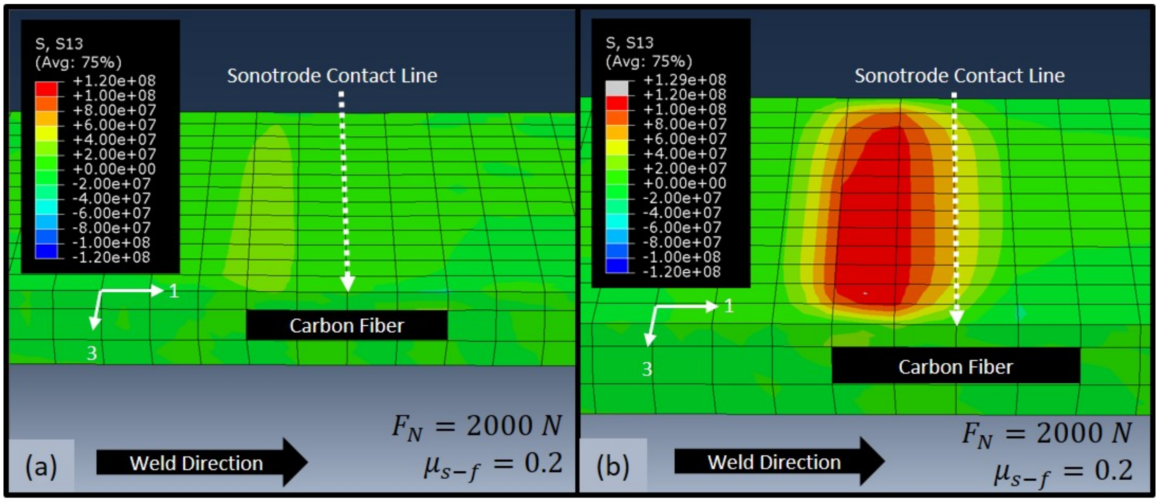

Figure 5.15: Special Case 2 FEA results and comparison. Dark red indicates yielding. (a) FEA S_{13} shear stress results for the special case where the CF/foil interface is given a friction coefficient of 0.5. (b) FEA S_{13} shear stress results for the original center of channel position case .

Special Case 3: Using Foil Constraining Guides

The third and final special case for the FEA modeling assumes that two constraining guides are used during the welding process which resist 3-direction motion in the foil and base layers. The goal in restricting this motion is to prevent the foil from displacing past a point where the it yields and tears. Modeling this scenario is not difficult, though physically this case is not realistic. First of all, constraining the foil motion in this manner would inhibit quality bonding near the edges of the foil. Second, it would be impractical to create guides that could hold the foil being welded with the level of precision needed. Nevertheless, this model was created to add insight into methods of foil tearing alleviation.

The results of this FEA case with constrained foil and base layer edges showed a large reduction in S_{13} stress over the leading edge of the channel. This shows that constraining the foil from 3-direction motion at it's edges can effectively force slip between the sonotrode and foil if the sonotrode/foil friction coefficient is low enough. However, a similar FEA case with the only difference being a higher friction coefficient of 0.5 did not predict the same result. With the 0.5 friction coefficient, slip only occurred at the edges of the foil near the constraints. This resulted in foil tearing being predicted in the central regions of the foil. The results from the 3-direction constraint case with 0.2 as the coefficient of friction is shown in Figure 5.16.

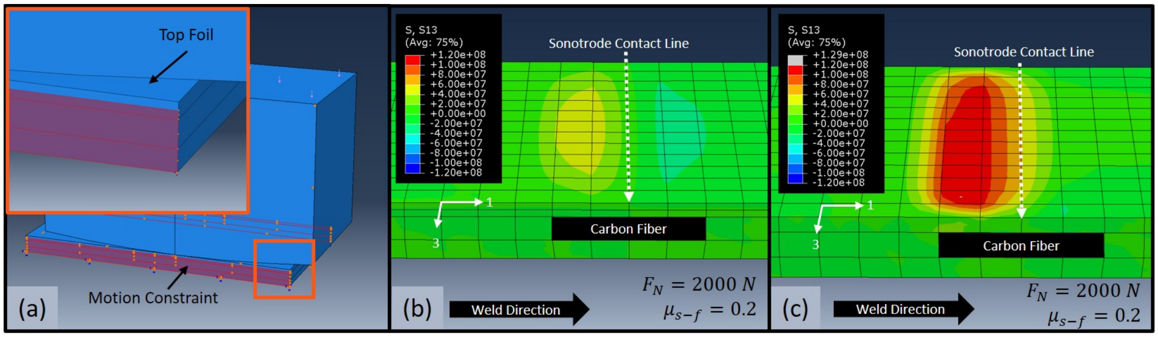
Top Foil
Motion Constraint
(a)
S, S13
(Avg: 75%)
+1.20e+08
+1.00e+08
+8.00e+07
+6.00e+07
+4.00e+07
+2.00e+07
+0.00e+00
-2.00e+07
-4.00e+07
-6.00e+07
-8.00e+07
-1.00e+08
-1.20e+08
Sonotrode Contact Line
1
3
Carbon Fiber
(b)
Weld Direction
$F_N = 2000\ N$
$\mu_{s-f} = 0.2$
S, S13
(Avg: 75%)
+1.29e+08
+1.20e+08
+1.00e+08
+8.00e+07
+6.00e+07
+4.00e+07
+2.00e+07
+0.00e+00
-2.00e+07
-4.00e+07
-6.00e+07
-8.00e+07
-1.00e+08
-1.20e+08
Sonotrode Contact Line
1
3
Carbon Fiber
(c)
Weld Direction
$F_N = 2000\ N$
$\mu_{s-f} = 0.2$

Figure 5.16: Special Case 3 FEA results with the foil and base layer edges constrained from 3-direction motion. Dark red indicates yielding. (a) 3-direction constraints on the base layer and foil edges. (b) FEA S_{13} shear stress results from using the 3-direction constraints. (c) FEA S_{13} shear stress results from original center of channel position case.

Summary of FEA Special Cases

In summary, each of the three special cases was successful in causing slip between the sonotrode and foil in order to prevent foil tearing. However, this was only true assuming a low friction coefficient of 0.2 at the sonotrode/foil interface. Results from similar simulations with a higher friction coefficient of 0.5 predicted foil tearing. A summary of the special cases and their results are listed in Table 5.3.

Table 5.3: Summary of FEA results for special cases.

Special Case	**Result**
Special Case 1: Tacked Foil	No Tearing Predicted
Special Case 2: CF/Foil Interface Friction	No Tearing Predicted
Special Case 3: Using Foil Constraining Guides	No Tearing Predicted

5.5 Discussion and Future Work

5.5.1 Summary and Conclusions

In conclusion, FEA modeling was completed using boundary conditions and surface interactions based on the predicted root cause of tearing, discussed in Section 5.2.3. Two sonotrode locations for the model were analyzed: with the sonotrode located at the center of the channel and with the sonotrode located at the end of the channel. In addition, three special cases were considered with the sonotrode located in the center of the channel with a sonotrode/foil friction coefficient of 0.2.

The results from the initial FEA models with boundary conditions and surface interactions described in Section 5.3.2 predicted foil tearing when the sonotrode/foil friction coefficient was 0.5. Reducing the friction coefficient to 0.2 reduced the amount of foil yielding. No yielding was seen with the low friction coefficient in the end of channel location. According to the FEA model results, it was found that the most critical sonotrode position concerning foil tearing is the center of channel position. However, even in this position, it was found that by reducing the normal force to 500 N, no foil tearing was predicted. This case of extremely low normal force simulates a situation where the CF in the channel is not packed tightly. This makes so the sonotrode cannot impart a large load onto the foil over the channel since there is not sufficient time for the sonotrode to compress the CF before the sonotrode has moved to another location.

FEA results from the special cases demonstrated that under certain circumstances, such as low sonotrode/foil friction, applicable boundary constraints can be placed in certain areas to induce slip between the sonotrode and foil, thereby eliminating foil tearing. While two of these special cases would be difficult to actually implement, the tacked foil special case could easily be tested and used.

5.5.2 Future Work Items

Experimental data is always important when validating a model or proving a hypothesis. Up to this point, most of the experimental work done to understand foil tearing has been qualitative. In order to provide a concrete experimental component to this analysis, three experimental measurement sets should be taken. These three measurement sets are described below in the following points.

1. Use a laser vibrometer to collect measurements while welding over a base structure with channels. The measurements necessary include: foil displacement, sonotrode displacement, and base layer displacement (directly underneath the top foil). Having these measurements would provide information on actual sonotrode/foil relative motion for this unique scenario. This information could then be used to better inform the FEA model inputs. The FEA would then predict whether failure would occur and could be compared to the experimentally observed result.

2. Use pressure sensitive paper to estimate the pressure exerted on the CF within the channel during consolidation. Unfortunately, pressure sensitive paper does not provide high accuracy results, but an approximation is still a valuable data point.

3. Investigate the UAM machine's z-position control settings. If the sonotrode z-position response time can be slowed during welding, this could prevent the

sonotrode from increasing the weld normal force when welding over carbon fiber. Since foil tearing is very sensitive to the weld normal force, this control modification could reduce foil tearing greatly.

4. Use sensing devices to determine the exact sonotrode position when the foil tearing occurs. This testing would require some variety of NDE testing sensors which use structural vibrations or eddy current techniques to determine the exact point in time when the foil tearing occurs. If this can be done, it will provide valuable insight into the foil tearing failure mode.

Chapter 6: CONCLUDING REMARKS

6.1 Summary

In this research project, it was shown that the UAM process can be used to embed fibrous materials including carbon fiber, nickel coated carbon fibers, and glass fibers within 6061-H18 aluminum. The fiber consolidation was achieved without damage to the embedded fibers. This was verified by optical and SEM imaging as well as visual inspection. Additionally, carbon fibers were successfully embedded within high strength 4130 steel, using 201 nickel as inter-layers between the steel foils. Pullout testing on embedded fiber tows was completed to determine pullout strength for different fiber/adhesive combinations. The highest pullout strength was accomplished with the nickel electroplated CF tows, the second highest pullout strength was seen with the plain CF tows, and the glass fiber tows had the lowest pullout performance.

Using the embedding technique discussed in Chapter 2, CF-aluminum joints were created by embedding multiple layers of CF tows. Each embedded layer included 8 to 18 CF tows, depending on the joint design. After the CF consolidation, the joints were laid up with epoxy to create specimens for tensile, cross tensile, and three-point-bend mechanical testing. Two joint thicknesses with three and five embedded layers of CF tows were developed for a CF-Al joint design with straight channels.

These joints were tested in tension and bending. The three layer variety were also subjected to corrosion cycling and were tested in tension after a period exposed to the harsh environment. Testing results showed that the corrosion cycling did not have a significant impact on the strength of the specimens. More extensive corrosion testing will need to be completed in the future.

A second generation of CF-Al joints were developed which featured curved channels. Through experimentation and tensile testing, it was found that the curved channel joint design paired with a CF sandwich feature produced a joint with superior strength to other previous designs. Cross tensile joints of the same thickness as the curved channel joint were also developed and tested following the JIS Z 3137 cross tensile testing standard.

Adhesive single lap versions of the CF-Al tensile and cross tensile joints were created to provide a comparison of UAM joint strength with a state-of-the-art joining method. Careful attention to surface preparation was made with regard to these adhesive specimens. A comparison of tensile and cross tensile testing for UAM and adhesive CF-Al joints showed that the UAM joints have greater strength in both categories. The average UAM joint peak load was 9241 N and 3370 N for tensile and cross tensile testing respectively. The average adhesive joint peak load was 5799 N and 1680 N for tensile and cross tensile testing respectively. This benchmarking demonstrated that UAM CF-Al joints can compete and in some cases surpass current state-of-the-art joining methods in strength.

In addition to CF-Al joint design and testing, the manufacturing process necessary to create the joins was developed. Experimental observations were made to predict a foil tearing root cause. Methods for accomplishing repeatable manufacturing without foil tearing were investigated and found by trial and error experimentation. In addition, an FEA model was created which provides support to the predicted foil tearing root cause and insight into potential foil tearing alleviation methods.

6.2 Future Work

One of the first items of future work includes gathering experimental measurements necessary for inputs into the foil tearing FEA model. These include foil, sonotrode, and base layer displacement measurements as well as carbon fiber tow pressure approximations. Each of these measurements must be taken during the welding process on a welding substrate with channels. Since it may be difficult to obtain several laser vibro-meters to gather all three displacement measurements at once, welding a number of identical passes may be necessary. Once obtained, these measurements will be used to better inform the FEA model inputs.

A second future work item includes continued work on CF-Al joint optimization. As discussed in Section 3.4.3, the current curved channel CF-Al joint design has a region of reduced cross sectional area which is also filled with stress concentrations due to the channels. There are many pleasing attributes about the current curved channel design, but efforts should be focused on creating a similar design that has improved aluminum tab strength. Though not discussed in this thesis, FEA modeling of CF-Al joints is currently being pursued for the curved channel design. Once this modeling is completed and validated it will be used to guide this joint optimization process.

The third future work item deals with embedding pre-preg CF tows and exploring the effect of epoxy viscosity on tow pullout strength. If embedding pre-preg CF tows proves successful, this could greatly increase CF tow resistance to pullout. Embedding pre-preg CF tows could also potentially improve the ease of CF-Al joint UAM manufacturing. The viscosity of epoxy used during the layup process is important because the epoxy must penetrate deep into the embedded CF tows for proper CF load sharing as well as adhesion to the channel walls. The use of small holes to promote epoxy flow within the CF filled channels may also be explored.

The fourth future work item deals with transferring techniques discussed in this thesis to use with high strength steel. As briefly discussed in Section 2.3.1, CF-steel joining methods are greatly needed in industry. It is preferred that the CF-steel joining not include nickel inter-layers as done in Section 2.3.1 because of strength and cost concerns. The UAM process is not quite developed enough with regard to steel to be used for creating CF-steel joints. However, separate efforts are currently under way to achieve desired UAM results with steel.

The fifth and final future work item discussed here is the issue of corrosion. Preliminary corrosion cycling followed by visual inspection and mechanical testing was completed as discussed in Section 3.1.2. However, more rigorous corrosion testing is needed. In actual applications, CF-Al joints will be exposed to harsh environments and be expected long use lifetimes. The length of corrosion cycle testing will need to be extended to 10-20 year equivalent time periods. One potential corrosion mitigation technique is to use anodized aluminum as the metal material used in the UAM process. Anodized aluminum has a thick insulating oxide layer which helps prevent corrosion. If necessary, other corrosion prevention techniques such as fiberglass barriers may need to be explored and integrated into the joint design. Designing for strength and profile have been primary concerns of this work up to this point, but long term durability is of equal importance.

Bibliography

[1] Astm d2093: Standard practice for preparation of surfaces of plastics prior to adhesive bonding.

[2] Astm d2651: Standard guide for preparation of metal surfaces for adhesive bonding.

[3] Astm d5573: Standard practice for classifying failure modes in fiber-reinforced-plastic (frp) joints.

[4] Marcelo J. Dapino Adam Hehr. Dynamics of ultrasonic additive manufacturing - in review. *Ultrasonics*, 2016.

[5] CS Adderley. Adhesive bonding. *Materials & Design*, 9(5):287–293, 1988.

[6] ST Amancio-Filho, C Bueno, JF Dos Santos, N Huber, and E Hage Jr. On the feasibility of friction spot joining in magnesium/fiber-reinforced polymer composite hybrid structures. *Materials Science and Engineering: A*, 528(10):3841–3848, 2011.

[7] F Balle, G Wagner, and D Eifler. Ultrasonic spot welding of aluminum sheet/carbon fiber reinforced polymer–joints. *Materialwissenschaft und Werkstofftechnik*, 38(11):934–938, 2007.

[8] Frank Balle. Joining of dissimilar materials by ultrasonic metal welding. In Khoo Boo Cheong Gan Woon Stong, Lim Slak Plang, editor, *Proceeding of the 2013 International Congress on Ultrasonics*, 2013.

[9] Frank Balle, Stefan Emrich, Guntram Wagner, Dietmar Eifler, Alexander Brodyanski, and Michael Kopnarski. Improvement of ultrasonically welded aluminum/carbon fiber reinforced polymer-joints by surface technology and high resolution analysis. *Advanced Engineering Materials*, 2013.

[10] Frank Balle, Guntram Wagner, and Dietmar Eifler. Ultrasonic metal welding of aluminium sheets to carbon fibre reinforced thermoplastic composites. *Advanced Engineering Materials*, 11(1-2):35–39, 2009.

[11] TA Barnes and IR Pashby. Joining techniques for aluminium spaceframes used in automobiles: Part iiadhesive bonding and mechanical fasteners. *Journal of Materials Processing Technology*, 99(1):72–79, 2000.

[12] Ferdinand P. Beer, Jr E. Russell Johnston, and John T. DeWolf. *Mechanics of Materials (In SI Units) (Mechanical Engineering Series).* McGraw Hill, 2005.

[13] DR Foster, GA Taber, SS Babu, and GS Daehn. In situ velocity measurements of very high power ultrasonic additive manufacturing using a photonic doppler velocimeter. *Science and Technology of Welding and Joining*, 19(2):157–163, 2014.

[14] R. Francis. *Bimetalic Corrosion, Guides to Good Practice in Corrosion Control.* National Physical Laboratory, 2000.

[15] Hannes Fuchs and Bryan Conrod. Super lap shear joint structural test-analysis correlation studies. In *Society of Plastics Engineers Automotive Composites Conference and Exhibition, Troy MI*, 2010.

[16] M. Bryant Gingerich. Joining carbon fiber and aluminum with ultrasonic additive manufacturing, 2014.

[17] LDR Grant, RD Adams, and Lucas FM da Silva. Experimental and numerical analysis of single-lap joints for the automotive industry. *International Journal of Adhesion and Adhesives*, 29(4):405–413, 2009.

[18] Justin Hale. Boeing 787 from the ground up. *Aero Quarterly, Boeing. com Commercial Aeromagazine*, 4:17–23, 2006.

[19] Adam Hehr, Joshua Pritchard, and Marcelo J Dapino. Interfacial shear strength estimates of niti-aluminum matrix composites fabricated via ultrasonic additive manufacturing. In *SPIE Smart Structures and Materials+ Nondestructive Evaluation and Health Monitoring*, pages 905906–905906. International Society for Optics and Photonics, 2014.

[20] CD Hopkins, PJ Wolcott, MJ Dapino, AG Truog, SS Babu, and SA Fernandez. Optimizing ultrasonic additive manufactured al 3003 properties with statistical modeling. *Journal of Engineering Materials and Technology*, 134(1):011004, 2012.

[21] Gordon Kelly. Joining of carbon fibre reinforced plastics for automotive applications. 2004.

[22] Ronald J Kerans and Triplicane A Parthasarathy. Theoretical analysis of the fiber pullout and pushout tests. *Journal of the American Ceramic Society*, 74(7):1585–1596, 1991.

[23] CY Kong, RC Soar, and PM Dickens. Optimum process parameters for ultrasonic consolidation of 3003 aluminium. *Journal of materials processing technology*, 146(2):181–187, 2004.

[24] JO Obielodan, A Ceylan, LE Murr, and BE Stucker. Multi-material bonding in ultrasonic consolidation. *Rapid prototyping journal*, 16(3):180–188, 2010.

[25] GD Janaki Ram, C Robinson, Y Yang, and BE Stucker. Use of ultrasonic consolidation for fabrication of multi-material structures. *Rapid Prototyping Journal*, 13(4):226–235, 2007.

[26] Chris Reiter. Bmw makes lone shift to carbon fiber to gain auto edge. *Bloomberg*, 2013.

[27] Jan H. Schut. Is thermoplastic rtm close to commercial? Plastics Engineering Blog, July 2014. http://plasticsengineeringblog.com/2014/07/02/is-thermoplastic-rtm-close-to-commercial/.

[28] Eric J Siggard. *Investigative Research Into the Structural Embedding of Electrical and Mechanical Systems Using Ultrasonic Consolidation (UC)*. ProQuest, 2007.

[29] Guangling Song, Birgir Johannesson, Sarath Hapugoda, and David StJohn. Galvanic corrosion of magnesium alloy az91d in contact with an aluminium alloy, steel and zinc. *Corrosion Science*, 46(4):955–977, 2004.

[30] Raghu Srinivasan, Lloyd H Hihara, and Jeffrey Nelson. Corrosion protection of interfaces between aluminum and mechanically-coupled polymer matrix composites (pmcs). In *224th ECS Meeting (October 27–November 1, 2013)*. Ecs, 2013.

[31] Richard Stewart. Carbon fibre composites poised for dramatic growth. *Reinforced Plastics*, 53(4):16–21, 2009.

[32] Mohammadreza Tavakkolizadeh and Hamid Saadatmanesh. Galvanic corrosion of carbon and steel in aggressive environments. *Journal of Composites for construction*, 5(3):200–210, 2001.

[33] Shruti Tiwari and LH Hihara. Development of a corrosion model to correlate the atmospheric corrosion rate of a carbon-fiber reinforced aluminum mmc to weather and environmental parameters. *Journal of The Electrochemical Society*, 161(9):C382–C388, 2014.

[34] Adam G Truog. *Bond improvement of Al/Cu joints created by very high power ultrasonic additive manufacturing*. PhD thesis, The Ohio State University, 2012.

[35] S Ucsnik, M Scheerer, S Zaremba, and DH Pahr. Experimental investigation of a novel hybrid metal–composite joining technology. *Composites Part A: Applied Science and Manufacturing*, 41(3):369–374, 2010.

[36] Kunio Uehara and Mitsuru Sakurai. Bonding strength of adhesives and surface roughness of joined parts. *Journal of materials processing technology*, 127(2):178–181, 2002.

[37] Austin Weber. Composite joining: Adhesive pros and cons. *Assembly Magazine*, 2013. http://www.assemblymag.com/articles/91199-composite-joining-adhesive-pros-and-cons.

[38] Stewart Williams. Joining of dissimilar materials - problems and solutions. http://www.jwi.hw.ac.uk/documents/Willliams$_1 20626_P resn.pdf$.

[39] Paul J Wolcott, Adam Hehr, and Marcelo J Dapino. Optimal welding parameters for very high power ultrasonic additive manufacturing of smart structures with aluminum 6061 matrix. In *SPIE Smart Structures and Materials+ Nondestructive Evaluation and Health Monitoring*, pages 905908–905908. International Society for Optics and Photonics, 2014.

[40] Chunbo Sam Zhang, Andrew Deceuster, and Leijun Li. A method for bond strength evaluation for laminated structures with application to ultrasonic consolidation. *Journal of materials engineering and performance*, 18(8):1124–1132, 2009.